*Università degli Studi di Genova*
*Facoltà di Scienze Matematiche Fisiche e Naturali*
*Dipartimento di Fisica*

Ph.D. Thesis

# Chemical reactivity of supported Graphene single layers

Giovanni Carraro

Tutor: Prof. Luca Vattuone (Università di Genova, Italy)
Dott. Marco Smerieri (CNR IMEM, Italy)

Referees: Prof. G. Comelli (Università di Trieste, Italy)
Prof. H. P. Steinruck (Friedrich Alexander University, Erlangen Nurnberg, Germany)

Genova, marzo 2018

# Table of Contents

Table of Contents ..... iii
List of Acronyms ..... 1
1 Introduction ..... 3
2 State of the Art ..... 6
2.1 Production methods ..... 7
2.1.1 Growth on Silicon Carbide ..... 10
2.2 Reactivity of Graphene ..... 11
2.2.1 Controlling the bandgap by adsorption ..... 13
2.2.2 The role of the support in determining the chemical reactivity of graphene ..... 14
2.2.3 Chemical reactivity of doped graphene ..... 15
2.2.4 Reactions under a graphene cover ..... 16
3 Experimental apparatus ..... 18
3.1 Introduction ..... 18
3.2 Need for Ultra High Vacuum (UHV) conditions ..... 19
3.3 UHV Apparatuses used in the Thesis ..... 20
3.4 UHV Production ..... 20
3.5 The sample holders ..... 21
3.5.1 Sample holder for the Spectroscopy Chamber ..... 21
3.5.2 Sample holder for the Microscopy Chamber ..... 21
3.6 Gas inlet systems ..... 22
3.7 Ion gun and sample cleaning procedures ..... 23
3.8 Experimental Techniques used in the thesis ..... 24
3.8.1 LEED – Low Electron Energy Diffraction ..... 24
3.8.2 QMS – Quadrupole Mass Spectrometer ..... 25
3.8.3 HREELS – High Resolution Electron Energy Loss Spectroscopy ..... 26
3.8.4 XPS – X Ray Photoelectron Spectroscopy ..... 31
3.8.5 STM – Scanning Tunneling Microscope ..... 35
4 Adsorption of CO on Graphene on Ni(111) and Graphene on $Cu_{poly}$ ..... 38
4.1 Introduction ..... 38

4.2 Experimental ..... 39
4.3 Results and discussion ..... 40
4.4 Conclusions ..... 51
5 N Doping of G/Ni(111) an its reactivity with CO ..... 53
5.1 Introduction ..... 53
5.2 Experimental ..... 53
5.3 Results and discussion ..... 54
5.4 Conclusions ..... 59
6 Vacancies at G/Ni(111) and at G/$Cu_{poly}$ and their reactivity with CO ..... 60
6.1 Introduction ..... 60
6.2 Experimental ..... 60
6.3 Results and discussion ..... 61
6.4 Conclusions ..... 67
7 Synthesis of different boron nitrogen carbon heterostructures on Pt(111) and their reactivity with CO ..... 68
7.1 Introduction ..... 68
7.2 Experimental ..... 69
7.3 Results and Discussion ..... 71
7.3.1 Preliminary results on the chemical reactivity of the B N C layers ..... 82
7.4 Conclusions ..... 85
8 Graphene on 6H SiC(0001) and its reactivity with atomic hydrogen ..... 87
8.1 Introduction ..... 87
8.2 Experimental ..... 88
8.3 Results and discussion ..... 88
8.4 Discussion ..... 94
8.5 Kinetic model ..... 98
8.6 Conclusions ..... 99
9 Conclusions ..... 100
Appendix A) Estimate of adsorption energy from HREEL spectra ..... 102
10 Bibliography ..... 105

# List of Acronyms

| | |
|---|---|
| Al | Aluminum |
| Ar | Argon |
| ARPES | Angle Resolved Photoemission Spectroscopy |
| Au | Gold |
| B | Boron |
| Co | Cobalt |
| Cr | Cromium |
| Cu | Copper |
| CVD | Chemical Vapour Deposition |
| D | Deuterium |
| DFT | Density Functional Theory |
| DMAB | Dimethyl Amino Borane |
| Fe | Iron |
| G | Graphene |
| H | Hydrogen |
| HT | High Temperature |
| Ir | Iridium |
| HREELS | High Resolution Electron Energy Loss Spectrometer/Spectroscopy |
| L | Langmuir |
| LT | Low Temperature |
| LEED | Low Energy Electron Diffraction/Diffractometry |
| LT STM | Low Temperature Scanning Tunneling Microscopy |
| ML | Monolayer |
| Mn | Manganese |
| N | Nitrogen |
| NEXAFS | Near Edge X ray Absorption Fine Structure |
| Ni | Nickel |
| NP | Nano Particle |
| Pd | Palladium |
| Pt | Platinum |
| QMS | Quadrupole Mass Spectrometer/Spectroscopy |
| Rh | Rhodium |
| RT | Room Temperature |
| Ru | Rutenium |
| SiC | Silicon Carbide |
| STM | Scanning Tunneling Microscopy |
| UHV | Ultra High Vacuum |
| XPS | X ray Photoemission Spectrometer/Spectroscopy |

# 1 Introduction

Although graphene (G) is generally considered a chemically inert material, pioneering work has demonstrated recently that it can be used effectively in gas sensing applications [1,2], and applications in chemistry have been envisaged, too [3–5].

Adsorption of molecules at graphene can be relevant for several applications such as, at least:

a) Sensoristic;
b) Active support for catalysis;
c) Engineering of the band gap for electronic applications;
d) Environmental applications (i.e. removal of toxic substances from water, etc).

The effectiveness of such approaches ultimately depends on the nature and strength of the adsorption. For sensoristic applications, the main issues are represented by sensitivity, selectivity and reversibility of adsorption at room temperature. The heat of adsorption must be high enough to obtain a detectable equilibrium coverage at room temperature and low enough to avoid the need to regenerate the sensor or to operate it at higher temperature. The sensor developed by Geim and Novoselov, for example, satisfies the requirements for high sensitivity but needs to be regenerated by annealing. This hardly reconciles with the low heat of adsorption expected for interaction with pristine G sites, so that the mechanism of operation of the sensor is not really understood yet at the atomistic level.

Graphene, thanks to its low chemical reactivity, can also be used as an active support for catalytic nanoparticles: it would physically host the nanoparticles (NPs) and can enhance their reactivity and durability owing to its high surface area, high conductivity, high stability and strong interaction with NPs [6].
Indeed, the best catalitic material should have an adsorption energy high enough to guarantee a sufficient local coverage of reactants (at the temperatures at which the catalyst is operated) and at the same time low enough to allow diffusion of the molecules to the metal nanoparticles where the reaction can effectively occur. Finally, yet importantly, the ideal support should prevent sintering of the nanoparticles under reaction conditions, a goal which requires a strong nanoparticle support interaction.

On the other hand, adsorption of molecules or atoms can be used to tune the band gap of graphene for electronic applications: this application requires the adsorbate to be stable and the presence of a nonmetallic substrate. Graphene on SiC, is often used in these cases since large and high quality graphene films can be easily grown, their electron mobility being only limited by scattering processes with the substrate. Decoupling of the graphene layer by hydrogen intercalation can further improve the transport properties approaching the fantastic mobility of free standing graphene (120.000 $cm^2/Vs$) [7].

It has been recently shown that the chemical reactivity of weakly interacting G on SiC with aryl radicals can be modified by the introduction of mechanical strain in the layer [8] and that the reactivity with respect to covalent functionalization is enhanced in presence of large substrate induced electron hole charge fluctuations for G on $SiO_2$ and $Al_2O_3$ [9,10].

Theoretical calculations also show that Al doped graphene might support stable CO adsorption [11]. The interaction of G with halogenated compounds [12] and with atomic hydrogen was also reported [13]. For less reactive environments/adsorbates only weak molecular adsorption was detected [14] at regular graphene sites [14].

The scientific literature reporting studies of adsorption of simple molecules at graphene is growing daily: in most cases, they are theoretical papers estimating the heat of adsorption of several simple molecules at pristine graphene sites, at vacancies and in presence of doping with N, B or heteroatoms. Experimental studies under controlled UHV conditions are, on the contrary, still rare.

In order to shed light on this important, but not yet deeply understood, phenomenology, I have investigated the chemical reactivity of supported graphene using experimental surface science methods. In particular, I focused my studies on the role of the substrate, the effect of N doping and the role of vacancies. To address properly the role of the substrate I have compared the reactivity towards CO of graphene grown on a strongly interacting substrate such as Ni(111) and on a less interacting substrate such as polycrystalline copper.

The choice of G/Ni(111) is motivated by the lower graphene substrate distance which maxim izes the potential role of the support, and by the fact that its growth mechanisms is well es tablished [15], while G on polycrystalline Cu is representative of a weakly interacting system and is widely used in applications. As I will show, similar results have been found for graphene on Pt(111), another weakly interacting support.

On the other hand, the choice of CO as a probe molecule is motivated both by the need for more sensitive CO detectors and by its wide use as a prototype molecule.

Controlled doping with N atoms have been obtained by $N_2$ low energy ion bombardment [16] while a controlled amount of vacancies (mostly single and di vacancies) has been obtained by low energy Ne ion bombardment.

In order to address the role of co doping a protocol for the growth of a mixed carbon boron and nitrogen layer on Pt(111) has been also developed (in collaboration with F. Bondino and collaborators in Trieste) and preliminary results for the reactivity of such layers with CO will be presented.

Finally, I considered also a prototype system with formation of a strong chemical bond investigating adsorption of atomic hydrogen on graphene on SiC.

The Thesis is organised as follows:

Chapter 2 briefly resumes the state of the art about graphene properties and its chemical reactivity.

Chapter 3 describes the experimental setup used for the growth of graphene and for the study of its chemical reactivity.

Chapter 4 reports about the reactivity of pristine graphene on Ni(111) and on polycrystalline Cu foil with CO, as published in [17,18].

Chapter 5 shows the effect of controlled N doping on the reactivity with CO, as reported in [19].

Chapter 6 deals with the reactivity of vacancies and discloses the relevant role of intercalation through the vacancies and the pivotal role of the support, reporting results published in [20].

Chapter 7 reports about the protocol for the growth of mixed C, B and N layers (see my paper [21]) and shows preliminary results about the reactivity with CO.

Chapter 8 addresses recent and still unpublished results about the interaction of graphene/SiC with atomic hydrogen around room temperature and below.

Finally, in chapter 9, I summarise the main results of the Thesis.

# 2 State of the Art

Graphene (G) is a carbon allotrope consisting of a single atom thick sheet of carbon atoms arranged on a honeycomb lattice and bound together by strong $sp^2$ bonds. It was discovered in 2004 by A. K. Geim and A. Novoselov, which were the first to really understand that they were dealing with a completely "new" material, characterized by 2 dimensional properties. Thanks to its structure, graphene shows unique properties that make it very interesting for fundamental research and quite promising for technological applications.

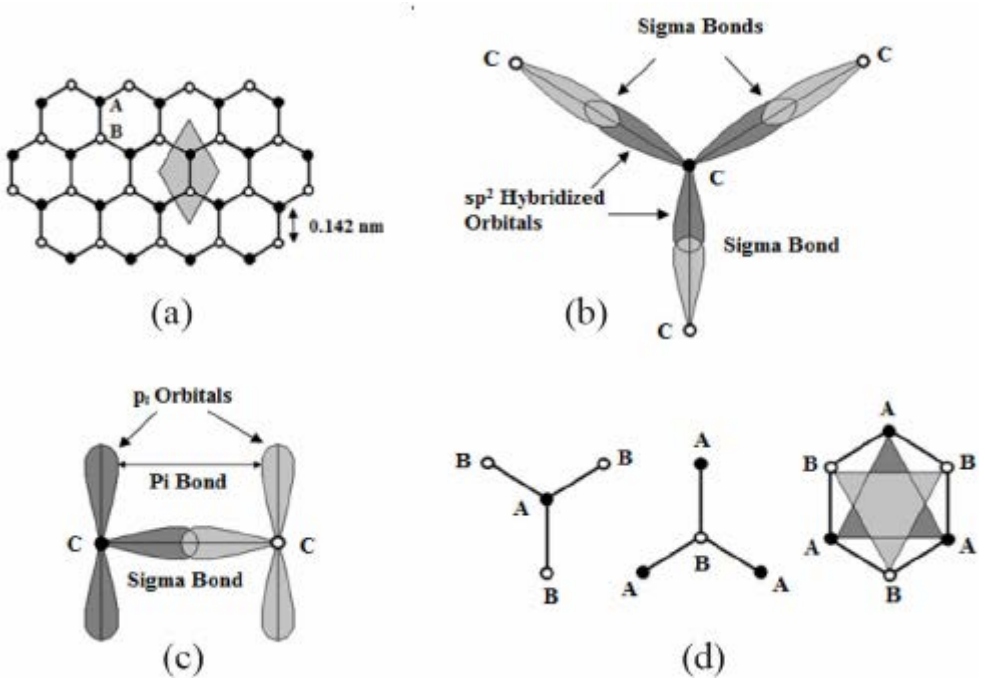


Figure 2.1 – (a) Graphene lattice structure with the honeycomb arrangement of carbon atoms. The unit cell (grey) contains two different carbon atoms A (black) and B (white) 0.142 nm apart. (b) sp2 hybridised orbitals forming three σ-bonds with the three nearest neighbours. (c) the electrons not involved in the sp2 bond are distributed perpendicular to the molecular plane. (d) the two different arrangements of the C atoms at A and B sites: the honeycomb lattice can be viewed as superposition of two triangular lattices of A and B carbon atoms. Picture taken from [22].

Graphene structure is show in Figure 2.1: the lattice exhibits hexagonal symmetry and belongs to the P6/mmm space group with two inequivalent C atoms in the unit cell sitting on A and B sites respectively, which are 0.142 nm, apart (at least in the pristine graphene configuration). The carbon atoms are bonded together by σ bonds arising from the interaction of the $sp^2$ hy bridized orbitals. The remaining electrons reside in the $p_z$ orbitals interacting with each other via π bonding, and these electrons are responsible for the valence and conduction band of graphene.

G band structure is characterized by linearly dispersing states near the Fermi Edge, forming cones in the band structure near the K and K' points (Dirac Cones). Because of this G is a zero bandgap semiconductor (also addressed as semi metal in older books) and can be easily trans formed into a semiconductor by doping or substrate interaction. At the same time, the linear

dispersion gives rise to an exceptional electron mobility (with zero effective mass, even if the cyclotron mass of the carriers is non zero but as low as 0.02 $m_e$ [23]).

More recently, researchers started to investigate new applications for Graphene, in particular the possibility to use G in sensor devices and in catalytical processes, where it could reduce the need for rare or expensive materials or eventually replace them altogether. The high surface/volume ratio of G means that a huge surface area can be obtained from a very low quantity of carbon, which is very cheap and common. Nonetheless, the price of G is presently mainly determined by the production cost, which is rapidly decreasing thanks to the large efforts devoted to the optimizations of the production techniques. A sfurther ubstantial decrease in the cost is expected when the production methods will scale up to mass production.

## 2.1 Production methods

Since the discovery of Graphene in 2004, more and more production methods have been discovered and engineered, but all of them can be roughly classified into two main groups: mechanical exfoliation and epitaxial growth.

To the first category belongs the scotch tape method originally used by Geim and Novoselov, which still is the preferred method for the production of relatively large area of freestanding samples with the best electronic properties to be used in transport experiments.

Production through sonication of high purity graphite crystals can also be used: this method, contrary to the scotch tape one, can produce graphene in large quantities but the flakes are usually smaller (up to a few 100 nm), less pure and mostly oxidized. A reduction process is then needed to really obtain pure graphene, but efficient production without degrading the quality of the graphene layer remains a challenge.

The second group of production processes consists in epitaxial growth methods, including for example Chemical Vapour Deposition (CVD), Molecular Beam Epitaxy (MBE) and growth by surface segregation. All these processes are usually applied to grow large area and high quality graphene layers on transition metals surfaces but also on other materials like Silicon Carbide (SiC).

Depending on the choice of the substrate, the quality of the grown film varies widely and with it also the electronic and mechanical properties.

A wide range of transition metals can be used to grow graphene by Chemical Vapour Deposition (CVD) either pure (Ru, Pt, Ir, Rh, Co, Ni or Cu) or in alloys (Au Ni, Cu Ni, Ni Mo) but most of the research is focused on Ni and Cu.

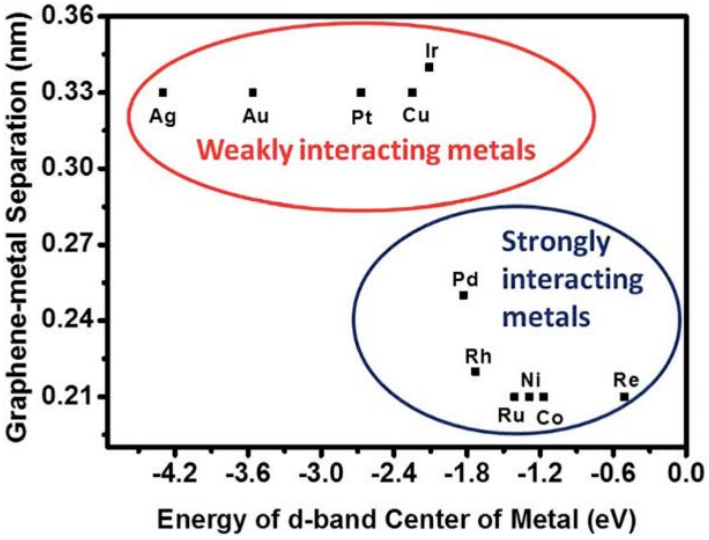


Figure 2.2 – Illustration of the correlation of graphene/metal separation with the energy of the d-band centre position (approx. 2eV below Fermi level). Picture taken from [24]

The different strength of the substrate film interaction will manifest itself in a larger or weaker deformation of the graphene bands, as reported in Figure 2.2 the lower the distance, the higher the interaction and the higher the band deformation.

Ni and Cu for example have quite different degrees of interaction with the G layer: while Cu is a prototypical weakly interacting metal substrate with a metal G separation of about 3.3 A, conversely Ni is strongly interacting, and the distance shortens to 2.1 Å. As a comparison, the inter layer separation in graphite is 3.35 Å. In general, growth on strongly interacting substrates, such as Ni, requires lower substrate temperature and lower pressure of the precursor hydrocarbon used in CVD than weakly interacting substrates, such as Cu.

An alternative growth method takes advantage of carbon dissolved into the bulk of the substrate:

the carbon dissolved into most bulk metals can be driven to the surface by thermal annealing, a phenomenon known as segregation. This carbon can be used as a source for graphene production, as demonstrated for Ni, Co, Fe and Cu Ni polycrystalline films [25].

The mechanism of graphene growth by carbon segregation proceeds in three steps:

1) thermally induced diffusion of dissolved carbon to the surface;
2) creation of growth nuclei by trapping of carbon atoms at grain boundaries and at step edges;
3) graphene growth around those centers by lowering the temperature.

Graphene production via segregation easily yields multilayer graphene, in contrast to the sin gle layer limitation of the CVD method. It is particularly efficient on Ni, Co and Pd due to their high carbon solubility (2.03%, 3.41% and 8.98% respectively), while it is strongly suppressed on metals having very low maximum carbon solubility, like Cu (0.04%) [24].

In experiments the carbon content of the sample is firstly increased by ethylene exposure at very high temperatures, then the hydrocarbon source is closed, and the substrate is slowly cooled down to promote graphene nucleation by segregation.

Chemical Vapor Deposition (CVD) relies on the catalytic decomposition of hydrocarbons on hot metal surfaces. The mechanism of graphene growth by CVD involves:

1) decomposition at the substrate surface;
2) graphene nucleation;
3) expansion.

CVD growth is direct, while the growth by segregation is an indirect process; however, for metals having high carbon solubility (such as Ni and Fe), the carbon will also diffuse into the hot substrate. As the substrate cools down, the dissolved carbon will segregate to the surface leading to the growth of graphene.

Many transition metals (Ni, Co, Ru, Ir, Pt, Cu) have successfully been used to catalyze the formation of graphene, and their catalytic properties come from the partially filled d orbitals and are enhanced by the formation of intermediate carbon compounds. The growth mechanism is substrate specific and depends on many characteristics such as carbon solubility, crystal face and surface cleanliness. This complicates the analysis of the processes involved and in fact very little is established up to now about the influence of all these factors, as for example about the role of transition metal carbides in graphene formation. It has indeed been observed that on Ni(111) the growth of an ordered single layer thick $Ni_2C$ phase competes with graphene growth [26–28]. On the other hand it has been argued that graphene growth by CVD on group IVB VIB metals is facilitated via carbide formation [29].

Being dependent on many factors, the graphene growth can be optimized by tuning several variables: the hydrocarbon used in the reaction ($CH_4$, $C_2H_4$, $C_6H_6$, …), the gas flux/pressure, the ratio of hydrocarbon and additional gases (Ar, $H_2$, $O_2$), the substrate temperature, after growth annealing processes, the cooling rate etc. A direct industrial interest is driving research to obtain high quality and large area graphene films on nickel, copper and other substrates.

Copper foils have been largely employed in CVD synthesis thanks to their large availability, low cost and to the relatively mild growth pressure and temperature required in the growth: tem peratures ranging from 800 to 1050°C and ethylene or methane are usually employed for this purpose.

Ni(111) is the metal single crystal surface having the smallest lattice mismatch with graphene (about 1.3%), and the interaction with the matching substrate is particularly strong. The growth on metallic single crystals requires previous surface cleaning, by standard cycles of ion sputtering (argon or neon ions) and annealing at high temperature (details in the experimental section). Graphene can then be prepared by thermal dehydrogenation of hydrocarbons on the surface. In a typical preparation recipe, the substrate is heated to 550°C and exposed to a

pressure of $10^{-7}$ to $10^{-6}$mbar of ethylene ($C_2H_4$) in UHV chamber for approximately 10 minutes. The preparation temperature is lower than the one needed for copper due to the higher chemical reactivity of nickel, and it influences the properties of the resulting film. At lower temperature undesired nickel carbide is formed, while higher temperature can be used only for carbon enriched samples. In the latter condition a significant increase of rotated graphene domains can be observed [28]. Further increasing the preparation temperature leads to the production of multilayer graphene.

Due to the small mismatch between the graphene and the Ni(111) lattice constants graphene grows in a (1x1) structure having different possible configurations, depending on the relative position of the carbon atoms respect to the underlying nickel lattice (see Figure 2.3).

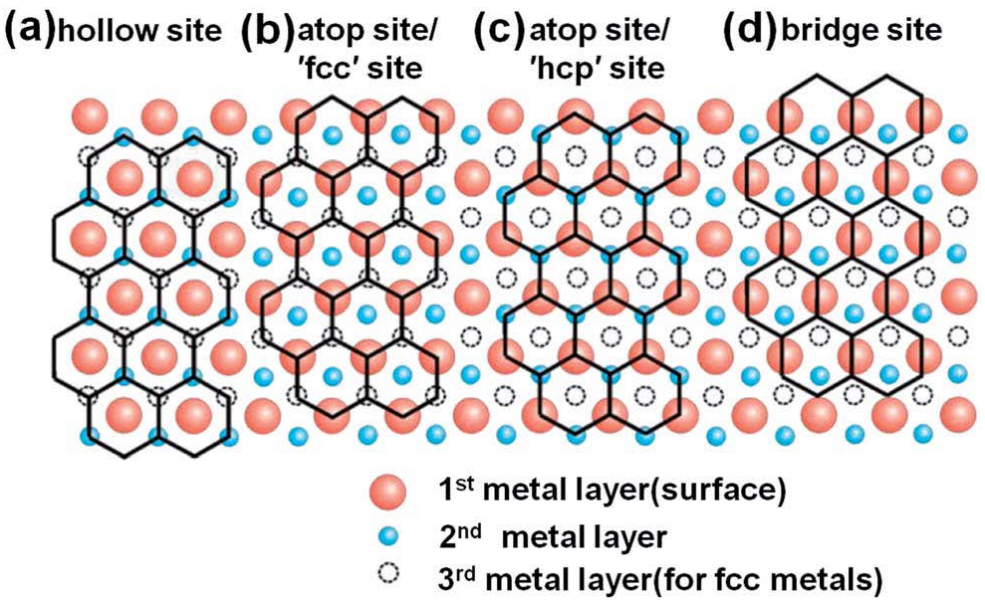


Figure 2.3 – The four different basic adsorption configurations of a honeycomb lattice on a matching hexagonal densely packed metal surface. Taken from [30]

The main structural features are the interlayer distance between graphene and the topmost Ni layer of 2.11 Å and the very small corrugation (0.05Å) between the two carbon atoms of the graphene sublattices. This small interlayer distance, compared to graphite interlayer distances, is a consequence of the strong interaction between C and Ni atoms at the interface. In particular, there is a strong *n* doping of graphene due to electron transfer from the Ni 4s to the Gr π states and angle resolved photoemission electron spectroscopy (ARPES) experiments performed on this interface clearly show a gap opening in the Gr π band [31].

### 2.1.1 Growth on Silicon Carbide

Silicon Carbide (SiC) has become the most common substrate of choice to grow graphene for electronics applications because high quality graphene easily grows on large area SiC wafers simply by heating and cooling the sample. Furthermore, the SiC substrate is a wide bandgap

semiconductor, and depending on the surface termination (Si or C), the electronic coupling is moderate or very low. The interaction between graphene and SiC can be reduced even more by intercalating Au or H below the graphene film. Nevertheless, the system is mechanically strongly bonded, and the graphene layer cannot be detached from the substrate.

When the SiC substrate is annealed to high temperature, typically at 1200°C under UHV con ditions [32], silicon atoms start desorbing from the surface sooner than carbon atoms, and, under appropriate conditions, graphene is formed.

Depending on the growth parameters, like temperature, heating rate, and pressure, single or multi layer graphene can be grown, and the number of layers can be tuned to some extent. Even though the thermal decomposition of SiC in UHV appears promising for large scale production, this method usually produces small grains (30–200 nm) with variable thicknesses.

The homogeneity of the graphene layers can be increased by annealing the SiC samples above 1600°C in argon [33] (but the purity of the argon gas and the composition of the residual gases can play a role in the quality of the resulting film [34]) or by providing an additional carbon supply at lower temperature [35].

The interaction between the graphene layer and the SiC(0001) substrate is mediated by a strongly bounded carbon buffer layer. Graphene is thus epitaxial, but the mobility of its carriers is significantly affected by the presence of the buffer layer. Epitaxial graphene on SiC is in fact intrinsically n doped (with a carrier density n of the order of $10^{13}$ cm $^{2}$) so that the Fermi level is shifted above the Dirac point. For electronic applications it is thus of utmost importance to recover the intrinsic carrier concentration density and to reverse the shift of the Fermi: such goals can be partially obtained by doping with electron acceptors atoms as antimony or bismuth[36], by hydrogen intercalation at high temperature [37] or by deposition of electronegative tetrafluoro tetracyanoqunodimethane (F4 TCNQ)[32,38].

Bilayer G/SiC is characterized by a small band gap which can be tuned by electronic influence of the buffer layer[37] or by strain forces[39] and the Fermi level of graphene can be shifted into this bandgap (again by transfer doping) in order to produce a true semiconducting graphene.

## 2.2 Reactivity of Graphene

Graphene is usually considered to be chemically inert: theoretical studies have calculated the adsorption energy for simple molecules (such as CO, $H_2O$, NO; $NH_3$) on freestanding graphene layer. The adsorption energy depends on the site and the molecular orientation, but it always falls in the energy range usually assigned to physisorption (for example it is lower than 47 meV for $H_2O$, than 31 meV for $NH_3$, 14 meV for CO, 67meV for $NO_2$ and 29 meV for NO [40]).

Some of the molecules that have been tested in simulations behave like electrons acceptor ($H_2O$ and $NO_2$) creating trap states for graphene electrons and producing a net p doping of the system, while others act like donors ($NH_3$, CO, NO), symmetrically causing an n doping. This

effect, called *molecular doping* [2], is strong enough that graphene manifests macroscopic chemical sensing properties, as demonstrated by pioneering experiments [1] showing a change in the resistivity of the graphene upon adsorption of different molecules, as reported in Figure 2.4.

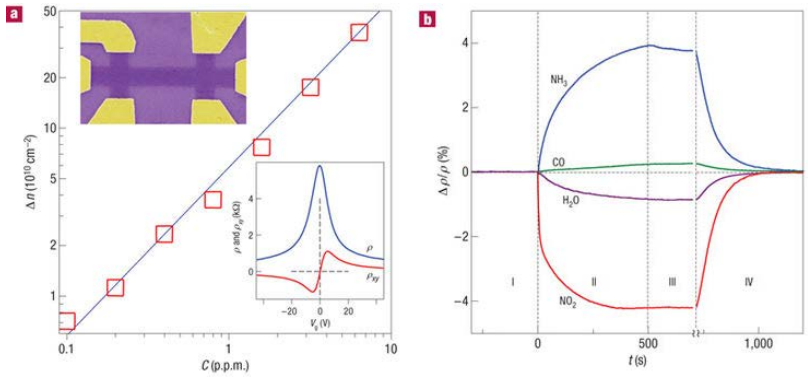


Figure 2.4 - Sensitivity of graphene to chemical doping. A) Concentration, Δn, of chemically induced charge carriers in single-layer graphene exposed to different concentrations, C, of $NO_2$. Upper inset: Scanning electron micrograph of this device (in false colours matching those seen in visible optics). The scale of the micrograph is given by the width of the Hall bar, which is 1 μm. Lower inset: Characterization of the graphene device by using the electric-field effect. B) Changes in resistivity caused by graphene's exposure to various gases diluted in concentration to 1 p.p.m. The positive (negative) sign of changes is chosen here to indicate electron (hole) doping. Region I: the device is in vacuum before its exposure; II: exposure to a 5 l volume of a diluted chemical; III: evacuation of the experimental set-up; and IV: annealing at 150 °C. Adapted from *[1]*.

The extremely low values of the adsorption energy predicted by the theoretical calculations however can hardly be reconciled with the need to anneal the graphene layer to 150 ° C in order to restore the initial resistivity ([1], see Figure 2.4). Because of this the nature of the adsorption site is still unclear and it is possible that the sensing activity has to be ascribed to adsorption at some defect or doped site and not directly to pristine graphene sites. The fact that the sensing activity is suppressed after removing the contaminants introduced using nanolithography [41] supports this hypothesis.

Other theoretical studies [42–44] suggest that adsorption on freestanding graphene in presence of doping or defects should be significantly increased. Indeed the adsorption energy of NO and $NO_2$ is predicted to increase up to 341 and 325 meV respectively at N doped sites [42], while doping with heteroatoms such as Al is required to increase significantly the adsorption energy of molecules like CO, $CO_2$, $O_2$ and others[45]. In general doping with Al, Cr, Mn increases the adsorption energy of molecules like $O_2$ more than N or B doping [46].

In presences of small defects, single and di vacancies, the theoretically predicted adsorption energies are as high as −8.44 eV, −4.53 eV, −13.83 eV, and −3.86 eV for $O_2$, $N_2$, $B_2$, and CO molecules, respectively [47]. Even an healing process of vacancies has been proposed: in this process a CO molecule would adsorb at a vacancy site and a NO molecule would subsequently remove the oxygen atom in adsorbed CO to form $NO_2$ which desorbs leaving the C atom to repair the vacancy. Similarly, controllable N doping should be achievable by sequential vacancy

creation (e.g., by an electron beam) and subsequent exposure to NO molecules at room temperature [44,48].

### 2.2.1 Controlling the bandgap by adsorption

An interesting consequence which arises from the characteristic *molecular doping*[2,49] in duced by adsorption, is the possibility to open a band gap. The presence of a band gap is in deed highly desiderable to use graphene in nanoelectronics and optoelectronics devices.

It has been suggested that a band gap can be created by doping with adatoms[50], or with interaction with gases [51,52] or ambient humidity [53]. Figure 2.5, shows the experimentally measured change in resistance with time for different absolute humidity (measured in weight of water content with respect to weight of air).

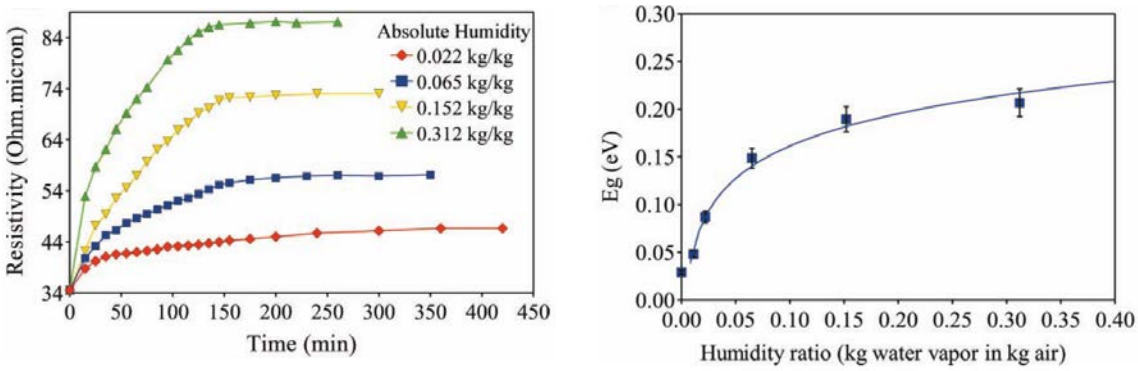


Figure 2.5 – (left) Change of resistivity for a graphene films as a function of time for different absolute humidity. (right) Bandgap (Eg) as a function of the absolute humidity. The bandgap increases sharply with humidity and then saturates at a level of ≈ 0.206 eV. Taken from [53] . Copyright from Wiley – VCH.

It is apparent that the resistance increases with time and that the higher the humidity the higher is the resistance. Interestingly, adsorption occurs reversibly. To prove the opening of a band gap the authors performed similar experiment keeping fixed the humidity and changing the temperature and demonstrated the presence of an activation barrier associated with elec tron transport in the graphene layer.

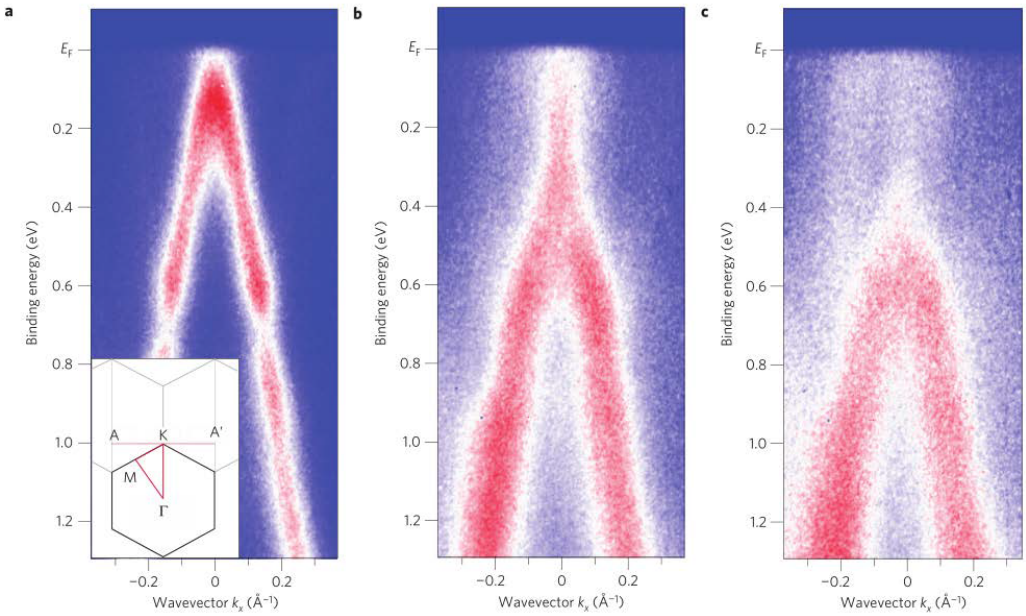


Figure 2.6 – *Photoemission intensity along the A–K–A' direction of the Brillouin zone for clean graphene on Ir(111) (a), graphene exposed to a 30s dose of atomic hydrogen (b) and graphene exposed to a 50s dose of atomic hydrogen (c). The inset shows the Brillouin zone. Taken from* [52]

Theoretical calculations also predict that exposure to atomic hydrogen allows for a tuneable band gap opening [54]. This approach was indeed experimentally verified [52] by exposing G/Ir(111) to atomic hydrogen: ARPES measurements showing the opening of a band gap upon H adsorption are reported in Figure 2.6.

### 2.2.2 The role of the support in determining the chemical reactivity of graphene

In most of real systems, graphene is not freestanding but is often supported on a substrate, thus rising the important question about the influence of the substrate on the reactivity of the graphene layer.

Figure 2.7 shows Temperature Programmed Reaction rates recorded for graphene on silica (green) and graphene on copper foil (red) after different exposures to water in UHV conditions.

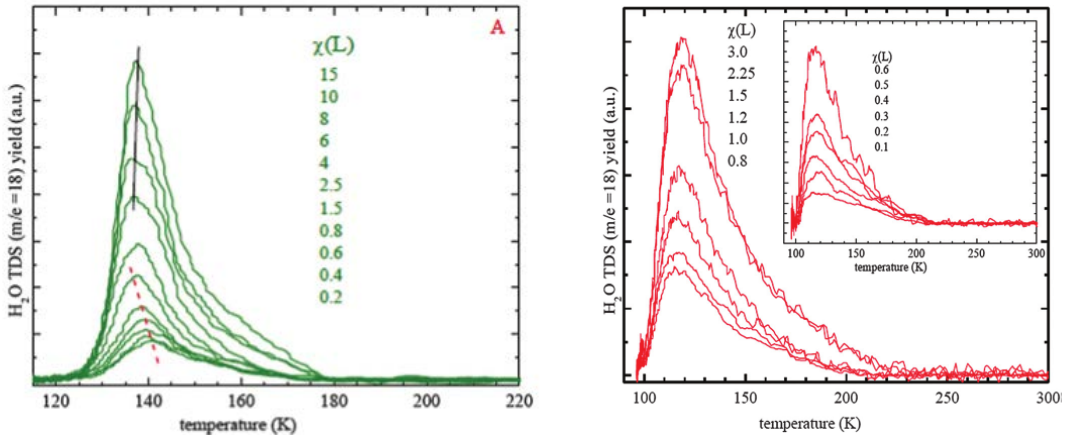


Figure 2.7 - *TDS of water as a function of water exposure (A) on hydrophilic graphene/SiO2 (left) and on graphene/Cu as a function of water exposure (right). The inset shows data for lower exposures. Taken from* [55].

While for graphene on copper foil the TDS peaks are almost aligned, for graphene on silica they initially do not align: this is an indication of a deviation from a zero order kinetic at lower exposures, suggesting a hydrophilic interaction and wetting of the surface. On the contrary, water adsorption on graphene/Cu is consistent with hydrophobic interactions, similar to graphene/Ru [56]. The authors concluded that the graphene wettability is anti correlated with the wettability of the support, i.e., if the support is hydrophobic, graphene shows wetting behavior (becomes hydrophilic) and if the support is hydrophilic, graphene shows non wetting behavior (is hydrophobic).

Note that desorption is completed at 180 K for G/$SiO_2$ while it continues up to temperatures higher than 200 K for G/Cu (and for G/Ru [56]), i.e. when the graphene substrate interaction is stronger.

The influence of the substrate does not affect only the (relatively weak) reactivity with simple molecules: as reminded already in the introduction, the presence of large surface charge fluctuations induced by the substrate enhances e.g. the reactivity of strong reactants such as aryl diazonium molecules with graphene supported on $SiO_2$ and $Al_2O_3$ [9], while adsorption is negligible on alkyl terminated and hexagonal boron nitride (h BN) surfaces.

### 2.2.3 Chemical reactivity of doped graphene

Despite the presence of a large amount of theoretical works suggesting the promoting role of doping on the chemical reactivity, only some experimental results have appeared.

Figure 2.8 shows experimental results about the electrochemical performance of ORR for doped graphene (grap HOPG and pyri HOPG) compared to undoped graphene (clean HOPG and edge HOPG). The Cyclic Voltammetry (CV) in standard acidic electrolyte (0.1 M $H_2SO_4$) under oxygen saturated conditions shows that the sample with pyridinic N (pyri HOPG) provides the highest current density.

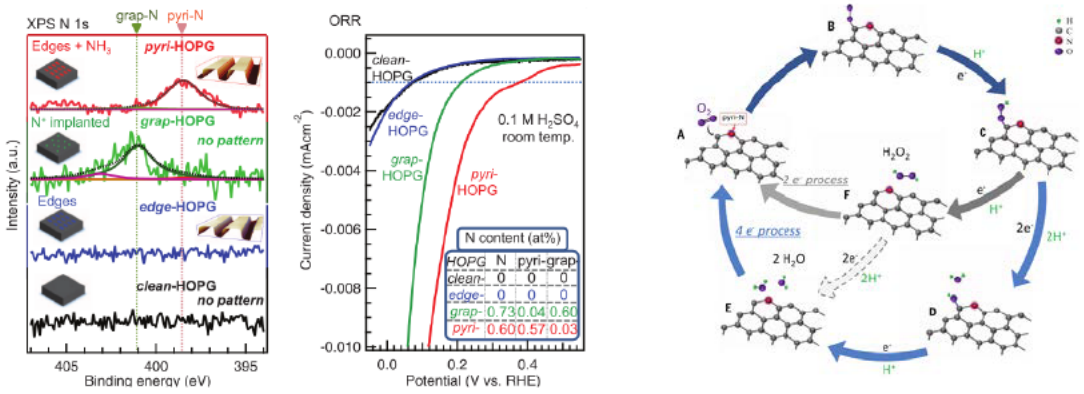


Figure 2.8 – (left) *N 1s XPS spectra of model Catalysts and (center) corresponding ORR results. (right) Schematic pathway for oxygen reduction reaction on nitrogen-doped carbon materials. Taken from* [57]

The left scheme depicts two alternative mechanism for the reaction involving two or four elec trons

The $O_2$ molecule initially adsorbs at C site next to pyridinic N. Then there are two possible reaction mechanisms. In the four electron mechanism, the other two protons attach to the two oxygen atoms, leading to the cleavage of the O OH chemical bond and to the formation of OH groups. The additional proton then reacts with the adsorbed OH to form $H_2O$.

In the other reaction mechanism (2+2 electrons) $H_2O_2$ is formed due to the reaction of OOH with a proton and then by re  adsorption of $H_2O_2$ which is then reduced by two protons to yield $H_2O$.

### 2.2.4 Reactions under a graphene cover

In recent years the idea of using graphene in chemical reaction occurring "under cover" has collected a lot of interest: reactions taking place in between the catalytically active substrate while desorption is partially hindered from the graphene and the activation barrier can thus be reduced [58–61].

Figure 2.9 shows the results for the CO oxidation reaction comparing the results obtained on bare Pt(111) and under graphene cover on Pt(111).

It is apparent that the slope of the Arrhenius plot for the CO oxidation reaction Pt(111) is higher than for 1.0 ML Gr/Pt(111) (panel a) indicating a higher activation barrier in the former case, in agreement with theoretical predictions (panel b). The comparison between the oxidation rate for bare Pt nanoparticles and for graphene covered Pt nanoparticles confirms (panels c and d) the result of surface science experiments (panel a and b): the activation barrier is reduced from 85 to 50 kJ/mol when the nanoparticles are covered with C.

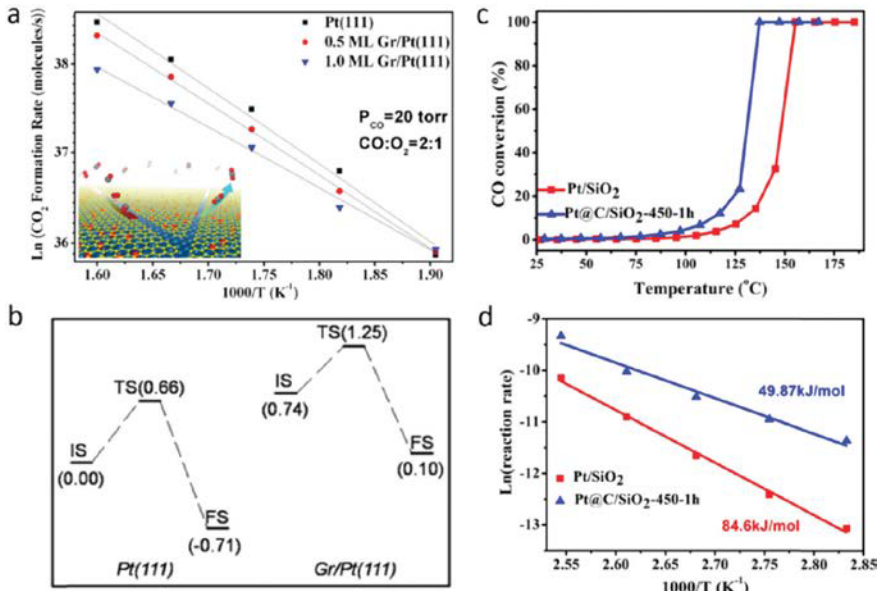


Figure 2.9 - Arrhenius plots of the CO2 formation rate on the Pt(111) surface and graphene/Pt(111) from 525 K to 625 K. The reaction gas consists of 20 Torr CO and 10 Torr $O_2$. (b) Calculated reaction barriers for oxidation between CO and O on Pt(111) and Gr/Pt(111), respectively. Values in the brackets are in units of electron volt. c) CO conversion as a function of reaction temperature over the Pt/SiO2 and Pt@C/SiO2 catalysts; (d) Arrhenius plots of the CO oxidation reaction rate (between 80 and 120 1C) over the Pt/SiO2 and Pt@C/SiO2 catalysts. Taken from [61].

# 3 Experimental apparatus

## 3.1 Introduction

In order to study the chemical and physical properties of graphene based systems it is necessary to work in Ultra High Vacuum (UHV) condition. This is required to limit the sample contamination and to study all the different processes under controllable conditions as well as to use electronic spectroscopies.

During this Ph.D. thesis, I have used two different UHV apparatuses, which will be labelled in the following as Spectroscopy Chamber and Microscopy Chamber, provided with all the tools needed to grow and characterize *in situ* most of the graphene layers.

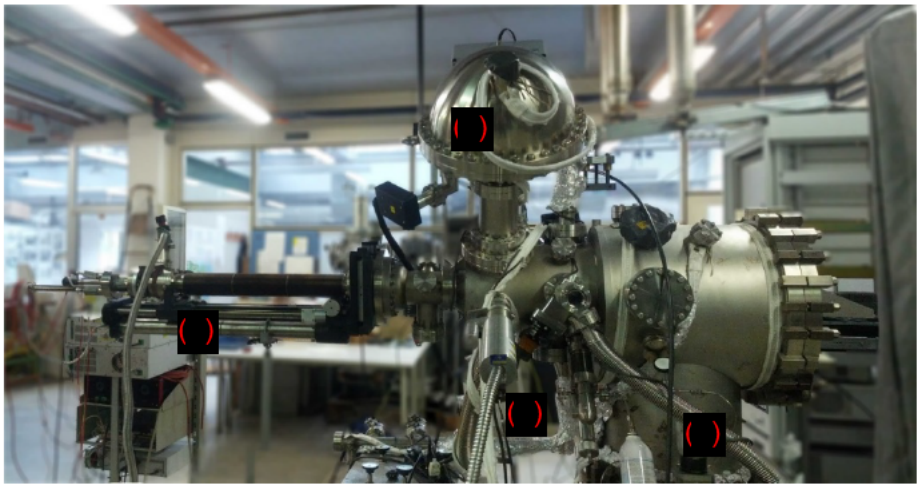

Figure 3.1 – A picture of the Spectroscopy Chamber – (a) sample manipulator – (b) X-ray source and (c) hemispherical analyser for the XPS – (d) the gas inlet system used to grow graphene

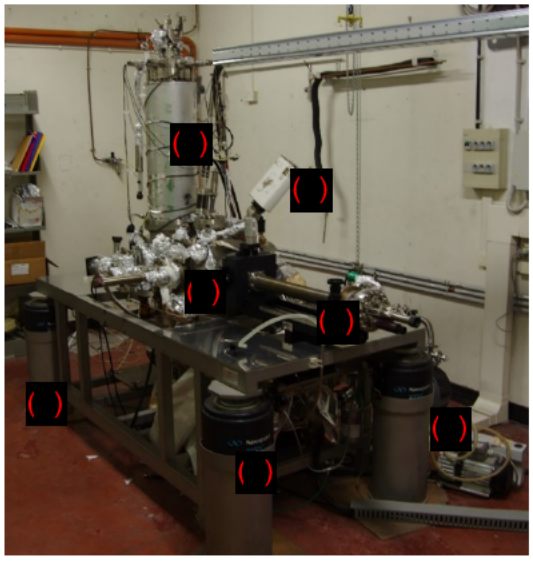

Figure 3.2 – Picture of the Microscopy Chamber – (a) sample manipulator – (b) external cryostat for liquid nitrogen housing a second cryostat for either liquid nitrogen or liquid helium and the LT-STM – (c) preparation chamber – (d) quadrupole mass spectrometer –(e) the whole chamber is held onto four damping feet.

The two chambers are characterised by the presence of different experimental facilities for the characterization of the sample. The Spectroscopy Chamber is provided with an X ray source and a hemispherical analyser for X ray Photoemission Spectroscopy (XPS) and houses a High Resolution Electron Energy Loss Spectrometer (HREELS). The Microscopy Chamber hosts a Low Temperature Scanning Tunneling Microscope (LT STM) which can be operated either at liquid nitrogen or liquid helium temperature.

## 3.2 Need for Ultra High Vacuum (UHV) conditions

UHV is required to study the interaction of gases with a surface in controlled conditions since the different gases present in air could interact with the surface, polluting it and eventually making it impossible to analyse the chemical processes.

UHV is the vacuum regime characterized by pressures lower than $10^{-9}$ mbar; at these low pressures, the number of molecules impinging on the surface per unit time is low enough that the surface remains clean for hours, allowing to perform the experiments.

The incident gas flow on the surface can be calculated directly from the ideal gas law:

$$n = \frac{N}{V} = \frac{P}{k_B T}$$

and using the mean molecular speed from the Maxwell Boltzmann distribution:

$$\bar{c} = \sqrt{\frac{8k_B T}{m\pi}}$$

The result is the Hertz Knudsen equation, which describes the sticking of gas molecules on a surface:

$$\Phi = \frac{1}{4} n\bar{c} = \frac{P}{\sqrt{2\pi m k_B T}} \left[\frac{molecule}{m^2 s}\right]$$

The quantity of gas molecules coming to the surface is given by exposure X=ϕ·t, which is usually expressed in Langmuir (L) in Surface Science:

$$1L = \frac{3}{4} \cdot P[10^{-6} mbar] \cdot t[s]$$

Or in monolayers (ML) where 1 ML corresponds to the number of atoms at the surface for unity of area (which depends on the particular surface studied). For example, for Ni(111) 1 ML $=1.41 \cdot 10^{15}$ atoms/cm$^2$ and 1 L corresponds to about 1/3 of a monolayer.

From the equation for the flux we can calculate for example that if the chamber is filled with carbon monoxide (CO, having mass m=28 a.m.u.) at pressure P=$10^{-9}$ mbar and at temperature T=300K the flux impinging onto the surface of the sample is ϕ=2.87 $10^{15}$ mol/(m$^2$s), and given the surface atoms density for Ni(111) which is $1.41 \cdot 10^{19}$ atoms/m$^2$, the flux becomes 1.46 ML/h. This provides an estimate of the maximum coverage attainable in a certain amount of time due to the background gas: 1.46 ML in these conditions, supposing a constant sticking coefficient equal to one, i.e. if all the molecules impinging onto the surface stick at its surface. Working under UHV conditions allows employing the experimental techniques based on low energy

electron beam and ion beams. Only when the pressure is low enough those particles can travel macroscopic distances without interacting with the stray molecules of air.

## 3.3 UHV Apparatuses used in the Thesis

The experimental chambers are mainly built of stainless steel 316L. They are constituted by big cylinders provided with several flanges housing all experimental instruments and all facilities needed for the experiments. All these tools must be themselves manufactured in UHV com patible materials.

As previously said, the Spectroscopy Chamber houses the XPS and the HREELS spectrometers, while the Morphology Chamber houses the LT STM. These instruments are the main tools for the experimental activity and are described in detail further on.

Except for these instruments, both chambers are provided with a common set of facilities, which can be found in many UHV apparatuses:

- sample manipulator with 4 degrees of freedom which can be heated to 1200°C or cooled to liquid nitrogen temperature;
- pumping system;
- low (thermocouple, Bayard Alpert) and high (ion gauge) pressure sensors;
- inlet gas lines for controlled input of reagents (Ne, Ar, $C_2H_4$, …);
- Ion gun for sample cleaning;
- Quadrupole Mass Spectrometer (QMS) for residual gas analysis;
- Low Energy Electron Diffractometer (LEED) for the crystallographic analysis of the surface.

## 3.4 UHV Production

A pressure low enough to reach UHV condition cannot be obtained by a single pumping system, but different pumping stages are used in cascade based on different pumping techniques:

1) The first, low vacuum stage ($10^3 – 10^2$ mbar) takes advantage of a mechanical pumping stage, using either a Scroll pump (in the Microscopy Chamber) or a double stage rotary pump (in the Spectroscopy Chamber).
2) The second, high vacuum stage ($10^2 – 10^9$ mbar) is still obtained by mechanical pumping with molecular and turbomolecular pumps for both chambers.
3) To reach the UHV regime (<$10^9$ mbar) in a relatively short time it is necessary to “bake” the chambers above 100°C for 24 h in order to accelerate the removal of water molecules and other gases from the inner walls of the chamber and of all the parts present inside it.
4) The third pumping stage, or chemical pumping system, consists of ion pumps and titanium sublimation pumps, which help to reach and to maintain UHV conditions and to further improve the base pressure.

5) Finally, both chambers are provided with cryogenic pumps, which can be used to improve the vacuum when required.

All pumping systems combined allow for a working base pressure as low as few $10^{-10}$ mbar, which can be reached in both experimental chambers. The microscopy apparatus can reach even lower pressures when the cryostats are filled with cryogenic liquid: no actual measurement is available but a pressure in the order of $10^{-12}$ mbar can be considered a good extimate.

## 3.5 The sample holders

### 3.5.1 Sample holder for the Spectroscopy Chamber

The sample can be moved within the chamber by means of a manipulator with 4 degrees of freedom (x, y, z, θ). The sample is mounted onto a sample holder (see Figure 3.3) which is a molybdenum bar, 2 mm thick, in electric and thermal contact with the sample.

The sample can be heated up to 1500 K via electron bombardment: the electrons emitted from a hot tungsten wire located behind the sample, are accelerated towards the back of the sample by a bias of some hundreds eV. The sample holder has a hole having a diameter of a few mm to allow the electrons to reach the backside of the sample.

The sample can be also cooled down to 90 K thanks to the thermal contact with a small cryostat at the end of the sample manipulator with a flow of liquid nitrogen. The temperature of the sample is monitored by a K type thermocouple (the two wires labelled (c)).

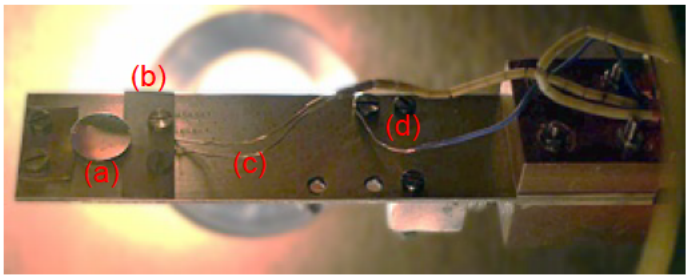


Figure 3.3 – The spectroscopy chamber sample holder – (a) the Ni(111) sample – (b) small molybdenum flags holding the sample against the sample holder – (c) K type thermocouple – (d) the grounding connection – The heating filament and the cold finger cannot be seen as they are located on the back of the sample holder.

### 3.5.2 Sample holder for the Microscopy Chamber

The Microscopy chamber is provided with a four degrees of freedom manipulator which is quite similar to the one mounted in the Spectroscopy chamber. The two sample holders are, on the contrary, quite different. The Microscopy Chamber sample holder must be detachable from the manipulator to allow its insertion inside the STM within the double cryostat. The free sample holder is shown in Figure 3.4 (a) while in panel (b) it is shown when connected to the manipulator, inside the preparation chamber in front of the LEED diffractometer and the ion gun. As it is visible in the small inset in Figure 3.4 (c), on the back of the sample holder electrical contacts are present.

When the sample holder is attached to the manipulator, it is possible to cool down the sample near liquid nitrogen temperature by a cold finger present at the end of the manipulator. This cooling system can be used as a pre cooling stage in order to reduce the thermal shock when inserting the sample holder in the STM inside the double cryostat when the inner cryostat is filled with liquid helium.

The temperature is monitored by a K type thermocouple which is mounted on a side of the sample itself and can be read both when the sample holder is attached to the manipulator or when it is placed inside the STM.

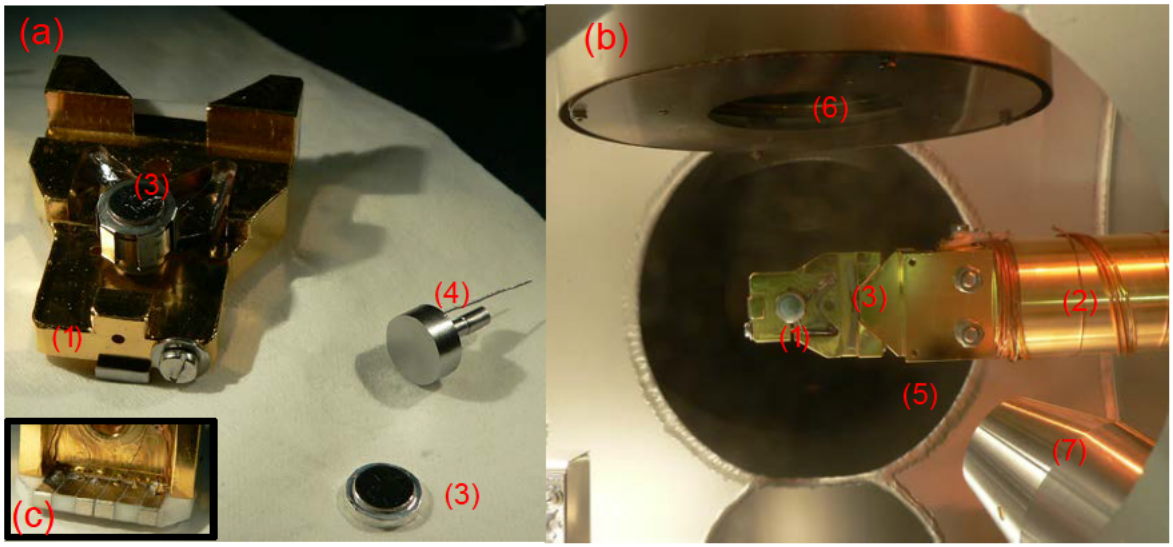


Figure 3.4 – Pictures of the Microscopy sample holder – (a) the sample holder outside of the chamber – (b) the sample holder attached to the manipulator – (c) detail of the electric contacts on the back of the sample holder – (1) sample holder – (2) manipulator – (3) sample – (4) sample heater – (5) grafting mechanism – (6) LEED diffractometer – (7) ion gun

To heat up the sample two possibilities are available: the simplest way is to use the resistive heating element visible in Figure 3.4 (a)(4) which consists of a tantalum wire dipped in a ceramic resin encapsulated in a molybdenum cage. This heater can heat the sample up to almost 1300 K with a very low degassing profile during heating. Alternatively, a home built electron bombardment heating system has been developed in order to heat the sample to higher temperatures.

## 3.6 Gas inlet systems

The UHV chambers are provided with different reagent input systems to expose the sample in a controlled way.

In the simplest option, a gas bottle is connected to a sapphire leak valve to expose the sample by *back filling* i.e. by filling the whole chamber with a desired pressure of the molecules. To reach higher exposure rates without polluting too much the chamber or in case of reactive or dangerous reagents a *doser* can be used. It simply consists in a small pipe which extends from the leak valve inside the UHV chamber and which can be positioned near the sample in order to increase the local partial pressure near the sample only by a factor of ~5 [62].

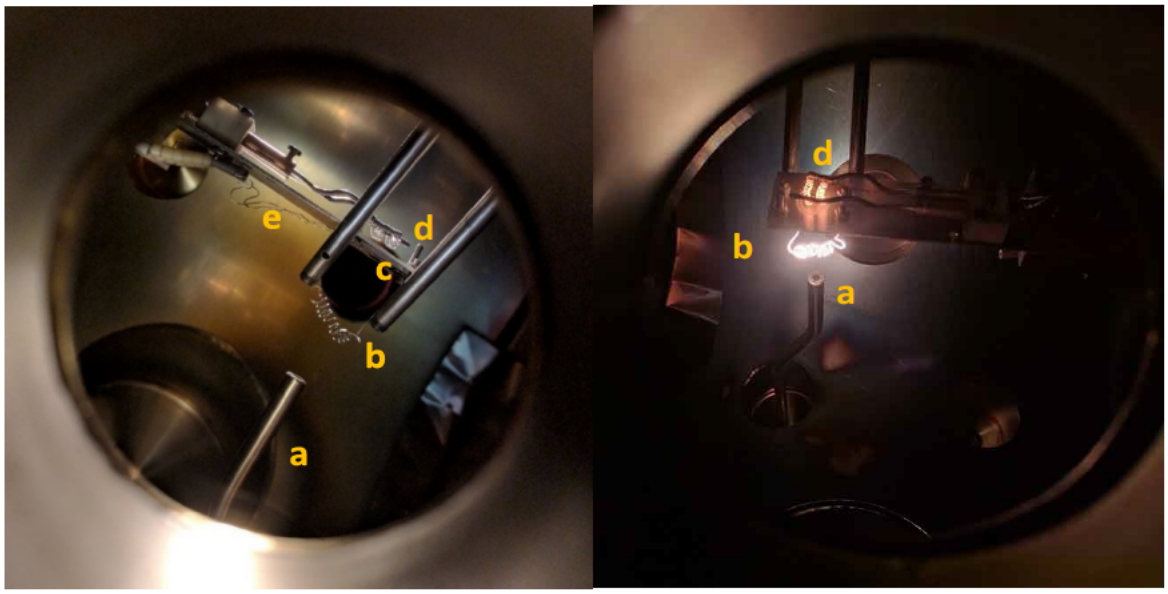


Figure 3.5 – Picture of the atomic H/D dosing system – (a) doser – (b) cracker filament not powered/powered – (c) sample – (d) sample heating filament – (e) thermocouple filaments

To produce a beam of atoms of H or D a filament cracker can be used. It consists of a hot tungsten wire, which is placed in between the gas doser and the sample, visible in Figure 3.5 (b). This hot filament is used to crack the molecules of hydrogen and deuterium to obtain a flux of H and D atoms.

During exposure of the sample to gas, Quadrupole Mass Spectrometer (QMS) is used to check for gas cleanliness.

## 3.7 Ion gun and sample cleaning procedures

A prerequisite of most of Surface Physics experiments is to have a clean and ordered surface ready to do experiments; to obtain this it is necessary to remove the topmost layers of the sample in order to clean the surface from contaminants and adsorbates coming from previous experiments or from the residual gases prolonged exposure.

In case of metallic substrates, the cleaning protocol consists in cycles of ion bombardment (sputtering) followed by thermal heating (annealing).

The sample is sputtered using an ion gun fed with a noble gas like argon or neon; the gun ionizes the atoms and accelerates them with an electric field of 1 3kV. The ions release the kinetic energy on the surface of the sample removing some material in the impact. This process lasts typically tens of minutes with an ion current of the order of a few microamperes, and after this treatment, the surface is clean but disordered.

To reorder the surface, it is necessary to heat the sample to a temperature high enough to increase the mobility of the atoms of the substrate without melting it. For nickel sample, the annealing temperature is 1200°C and the annealing lasts for few seconds to few minutes.

Both this processes of sputtering and annealing must be optimized depending on the characteristics of the instruments employed, on the geometry of each apparatus and even more depending on the materials used in each experiment. During these experiments I have been using $Ne^+$ ions accelerated with an energy $E_{ion}$ = 1.5 3.0 keV and impinging on the surface 45° off respect to the surface normal. The sputtering and annealing cycles last from 20 to 60 minutes each depending on the sample condition and are repeated a number of times sufficient to obtain a clean surface.

In case of strong carbon contamination, which is a common problem on transition metal substrates like nickel or even platinum samples, an additional cleaning process using oxygen can be required. The sample is heated to a temperature between 400 and 600°C and exposed to oxygen ($1 \cdot 10^{-6}$mbar for few minutes): the oxygen molecules dissociate on the surface and then desorb as CO molecules removing the carbon atoms.

At the end of the sputtering and annealing cycles, the surface order can be tested with the LEED diffractometer or with the STM microscope, while the cleanliness of the surface can be tested with XPS and HREELS spectroscopy.

## 3.8 Experimental Techniques used in the thesis

### 3.8.1 LEED – Low Electron Energy Diffraction

The Low Energy Electron Diffraction (LEED) is a surface science technique that uses the diffraction pattern obtained using low energy electrons to study the orientation and the periodicity of crystalline lattices and of the layers of adsorbates that can be deposited on the samples.

The electrons used have an energy ranging from 20 to 500 eV and at these energies, the De Broglie wavelengths associated with the particles are of the order of crystalline lattices: thus, they can interact with each other and an interference pattern can be obtained on the phosphor screen which corresponds to the reciprocal lattice of the surface structure.

The LEED is a surface specific technique since the mean free path for electrons having energies in this range is limited to a few atomic layers.

The electrons are extracted from a hot filament, accelerated, and focussed onto the sample with electrostatic lenses, then they are diffracted from the surface. A set of electrodes at the appropriate voltage guarantees that only elastically reflected/diffracted electrons are acceler ated towards a fluorescent screen. This screen is visible from the outside of the vacuum chamber through a window and the light emitted can be directly observed thus inspecting the diffraction pattern.

In Figure 3.6 is reported an example of LEED pattern obtained from a graphene film grown on a silicon carbide substrate.

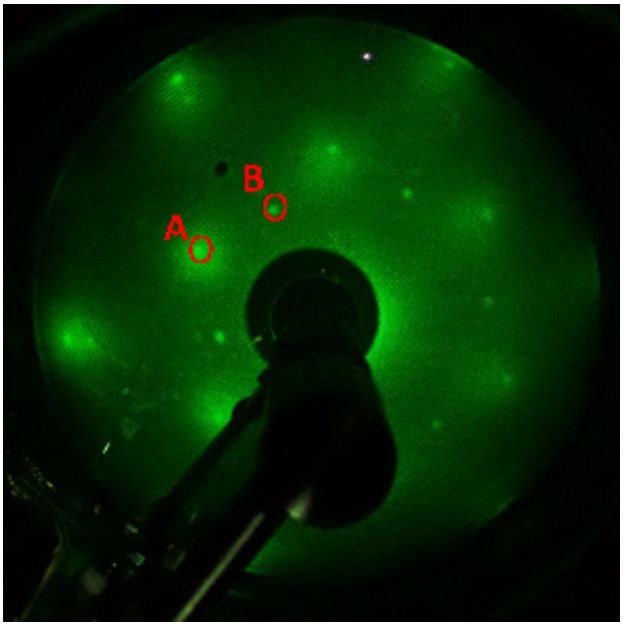


Figure 3.6 - Diffraction pattern obtained by LEED for Graphene on SiC. A indicate a spot due to the graphene lattice while B is a spot due to the underlying SiC substrate.

Two different series of spots A and B can be identified, each arranged with an hexagonal symmetry.

The A spots in particular are associated with the Graphene film grown on the SiC sub strate while the B spots are associated with another hexagonal geometry with very similar lattice spacings but is rotated 30° respect to the graphene layer. This structure is due to the carbon atoms of the buffer layer (more details can be found in the SiC experiments chapter).

Analysing the details of the LEED image, we can observe another weak series of hexagonally disposed spots emerging from the bright halo around the A spots. The size of these hexagons is smaller than the other two previously discussed and this means that the periodicity in direct space is actually larger respect to the brighter spots. These points correspond to the Moiré pattern, which is the superlattice originating from the low mismatch between the graphene lattice and the surface SiC lattice.

### 3.8.2 QMS – Quadrupole Mass Spectrometer

The Quadrupole Mass Spectrometer (QMS) is a tool used to determine the composition of all the gases that can be present in the chamber, as residual gas or as gas provided by the gas inlet system. Both experimental chambers are provided with a Balzers QMS similar to the one reported in Figure 3.7.

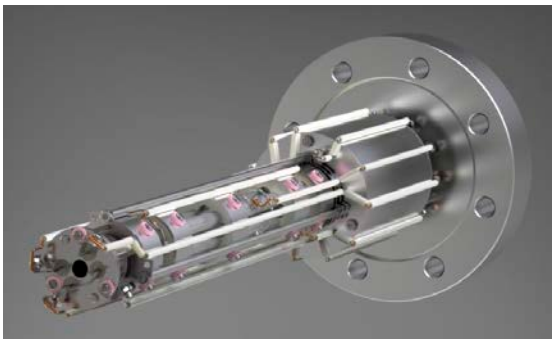

Figure 3.7 – Picture of the Quadrupole Mass Spectrometer

The QMS uses an hot filament and electric potentials to ionize and accelerate the gas molecules which pass through a quadrupole, i.e. four parallel metal rods alternatively contacted and polarized by the sum of a DC voltage and a radiofrequency AC voltage. The ions moving along the quadrupole will be influenced by this electric potential and only those having a defined mass/charge ratio can have a stable trajectory and pass through the skimmer at the end of the quadrupole.

The ions that reach the end of the quadrupole are eventually counted by an electron analyser (either a Faraday cup if the gas pressure is not low enough, or a channeltron to reach the maximum sensitivity).

### 3.8.3 HREELS – High Resolution Electron Energy Loss Spectroscopy

HREELS (High Resolution Electron Energy Loss Spectroscopy) is a spectroscopic technique that measures the energy losses of a monochromatized electron beam after scattering on the sample. This technique is able to detect collective electronic excitations and phononic vibrations of the surface itself or also of molecules or atoms adsorbed on it.

In both cases, during the scattering process, both the energy and momentum are conserved, thus:

$$E_i = E_f + E_{loss} \quad (1)$$

$$\boldsymbol{k}_{i,\parallel} = \boldsymbol{k}_{f,\parallel} + \boldsymbol{q}_{\parallel} + \boldsymbol{G}_{\parallel} \quad (2)$$

In the equations (1) and (2), $\boldsymbol{k}_{i,\parallel}$ and $\boldsymbol{k}_{f,\parallel}$ are the components of the wave vectors of the electrons parallel to the surface before and after hitting the surface, $\mathbf{q}_{\parallel}$ is the wave vector of the excitation activated during the scattering process, $\mathbf{G}_{\parallel}$ is one vector of the reciprocal lattice and, $E_{loss}$ represent the energy lost from the electrons in the scattering process.

The HREEL spectroscopy is a surface technique because uses electrons having an energy between a few eV and about 100 eV, the free mean path being usually or of the order of a nano metre.

Two different scattering processes can happen due to the interaction of the electron beam with the surface:

a) Dipolar scattering
b) Impact scattering

The dipolar scattering is a long range interaction through which the electron activates vibrational modes of the surface atoms or adsorbates.

The dipole mechanism is characterized by the following properties:

a) only modes causing a change of the dipole moment will be detected. In other words, the dynamical dipole moment associated with the vibrational transition must be non zero;
b) since the Coulomb interaction is quite long range and lasts for a relatively long time (some $10^{-14}$ s) the microscopic details of the interaction potential are not needed to describe it.

In the semi classical theory, the probability that an electron loses an energy hω to create a surface excitation at a crystal temperature T=0 K is given by:

$$P(\omega) = \frac{4e^2}{\pi^2\hbar}\int_D d^2q_{\parallel}\frac{(q_{\parallel}v_{\perp}^2)}{\left[(\omega - q_{\parallel}v_{\parallel})^2 + q_{\parallel}^2v_{\perp}^2\right]^2} \times \frac{Im(-1)}{\xi_0(\boldsymbol{q}_{\parallel},\omega)+1}$$

The last factor contains the effective dielectric function of the target ξ 0 , i.e. the surface properties. The domain of integration D is determined by the angles of acceptance of monochromator and analyser. In the semi classical limit, the surface is considered as a perfect reflector and the excitation probability equals the ratio $I_{loss}/I_{el}$, where $I_{loss}$ and $I_{el}$ are the intensity of the loss and of the elastic peak, respectively. From integration of eq. 1.1 the following relations are derived, where the different dependencies are caused by the different spatial confinement of the excited modes:

$$\frac{I_{loss}}{I_{el}} \propto \frac{1}{cos\theta\sqrt{E_0}\omega^2}$$

for surface phonons and plasmons (excitations decaying exponentially into the substrate) and

$$\frac{I_{loss}}{I_{el}} \propto \frac{1}{cos\theta E_0\omega}$$

for adsorbate modes (confined in the adlayer).

For non metallic substrates there are no restrictions on the orientation of the observable dipoles with respect to the surface and the only requirement is the existence of a non vanishing dynamical dipole moment. For metals, on the contrary, the image dipole will enhance the in tensity of perpendicular vibrations and screen out those parallel to the surface, leading to the well known metal surface selection rule: only molecular vibrations that give dipole changes perpendicular to a metal surface can be observed in HREELS when the scattered electrons are collected close to the specular direction. The ultimate physical reason for this is that for metals electronic oscillations (plasma frequency) have a much higher frequency (energies of several eV) than molecular vibrations (¯ hω ≤0.6 eV), so that the surface electrons can effectively screen parallel vibrations by giving rise to an image dipole in the opposite direction. This argument does not apply to semiconductors, characterized by 2 3 order of magnitude lower values of the plasma frequency and, *a fortiori*, to insulating samples.

Impact scattering is a short range process which can also activate vibrational modes which are not perpendicular to the surface. The energy dependence of the cross section is in general non monotonic and its intensity can be maximal under non specular scattering conditions [63].

Impact scattering is due to the losses arising during the collision of the electrons against the ionic cores of substrate or of adsorbate atoms. Contrary to dipolar scattering, it arises therefore from a short range interaction and is therefore not limited to small momentum transfer.

In a seminal paper Ho, Willis and Plummer[64] investigated the non dipole electron impact excitation of the vibrational modes of H adsorbed on W(100) and showed that for some of them the angle and energy dependence of the intensity deviates significantly from the one expected for dipole scattering. Impact scattering was not, however, systematically investigated until 1982 when the study of surface phonon spectra became a hot topic.

The theory to compute the impact scattering cross section is more demanding than for dipole scattering, since both crystal potential and multiple scattering have to be included explicitly. The scattering probability, firstly derived by Tong, Li and Mills [22], has the form:

$$\frac{dP}{d\Omega} = \frac{mE_0}{2\pi^2\hbar^2}\frac{\cos^2\theta_s}{cos\theta_0} S\left|M(\boldsymbol{k_0}, \boldsymbol{k_s}, \boldsymbol{q}_{\parallel}, \boldsymbol{u})\right|^2$$

Where: $\theta_0$ and $\theta s$ are the impinging and scattering angles measured from the surface normal, respectively; $E_0$ is the primary kinetic energy; $m$ is the electron mass; $S$ is the surface area hit by the beam; $M$ is the multiple scattering matrix element for an electron with initial wave vector $k_0$ into a state with final wave vector $k_s$ exciting or annihilating a phonon of wave vector $q_{||}$ (parallel to the surface) and polarization vector $u$.

It is important to remark that, for impact scattering, there is no relation between elastic reflectivity and inelastic cross section, since both are determined independently by multiple scattering. Consequently, normalization of the experimental data with respect to the specular elastic intensity makes no sense.

The $E_0 cos^2\theta_s$ factor in the equation above implies that the impact cross section increases with kinetic energy and decreases with $\theta_i$ and $\theta_s$. The actual dependence of the cross section on scattering energy and geometry is, however, so strongly modulated that no forecast for the most favourable experimental conditions is possible without calculating $M$. In general, since the growing cross section is more than counterbalanced by the worsening of the HREEL spectrometer performance with $E_0$ , the best conditions for observing phonons have usually to be searched between 20 eV and 50 eV.

The intensity of the energy losses are proportional to the adsorbate coverage, at least in the low coverage limit, when the interaction between adsorbates are negligible.

Nevertheless, an absolute determination of the coverage is in general quite difficult: the cross section for electron diffusion (both dipolar and impact) depends on many variables, such as the energy of the electrons, the impact and scattering angles and, for impact scattering, a microscopic scattering theory is required to describe the scattering process.

Even in the dipolar scattering regime, which can be described by a macroscopic theory, the intensity are still difficult to calibrate, since the dynamic dipole moment is not known *a priori*.

Additionally, the trajectories of the low energy electrons used, can be easily influenced from any stray electric or magnetic field, which are only partially screened by the magnetic shielding

of the chamber: the result is a relatively modest reproducibility of the absolute scattered intensities.

In the dipolar scattering regime, the intensities of the energy losses are typically at least two orders of magnitude lower than the elastic peak, which consists of the secularly and elastically reflected electrons. Nevertheless some vibrational modes which are particularly strong exist, like the Fuchs Kliewer [65][66] phonons typical of oxides and present also for SiC. These mixed phononic electromagnetic excitations originate from the counter phase motion of the two sublattices of silicon and carbon and generate strong oscillations yielding losses of intensity comparable with the one of the elastic peak.

They can be explained by using macroscopic dielectric theory without the need for a microscopic description of the scattering process of the electrons, which is, on the contrary required, to describe scattering in the impact regime.

In most of the experiments reported in this Thesis, spectra have been recorded under specular conditions (for which the angle if incidence and the angle of scattering are equal), at grazing angles and using relatively low electron energies to maximise the dipolar cross section for the detection of adsorbed CO.

When investigating hydrogen adsorption on graphene/SiC since the dynamical dipole moment of adsorbed H is very low, a systematic search for the scattering conditions enabling to maximise the intensity of the CH stretch has been performed. Such conditions correspond to $\theta_i$=62° and $\theta_s$=47° and E=5eV. The spectra have been normalised on the background level in the inelastic region of the spectra in order to allow a comparison of the intensities recorded in different experiments.

A schematic of the Delta0.5 HREELS spectrometer, manufactured by Specs, is reported in Figure 3.8: the electrons are emitted by thermionic effect from a $LaB_6$ cathode, and are focussed by the first set of electrostatic lenses (A lenses) into the input slit of the monochromatizing stage. This stage is actually composed of two actual sections, the pre monochromator and the monochromator, which are dispersing electrostatic lenses. The trajectories of the electrons depend on their energy and direction at the entrance and only those having a desired energy value can reach the exit slit.

The best resolution attainable with the instrument is strongly affected by the energy distribution of the electrons emerging from the monochromatizing stages: typically, a few meV.

The electrons are focussed on the sample and accelerated to the desired kinetic energy (1 100 eV) by the $B_1$ and $B_2$ lenses. After interacting with the sample, the scattered beam is focussed again towards the analysing stage by pair of lenses $B_3$ and $B_4$ symmetric to the previous ones.

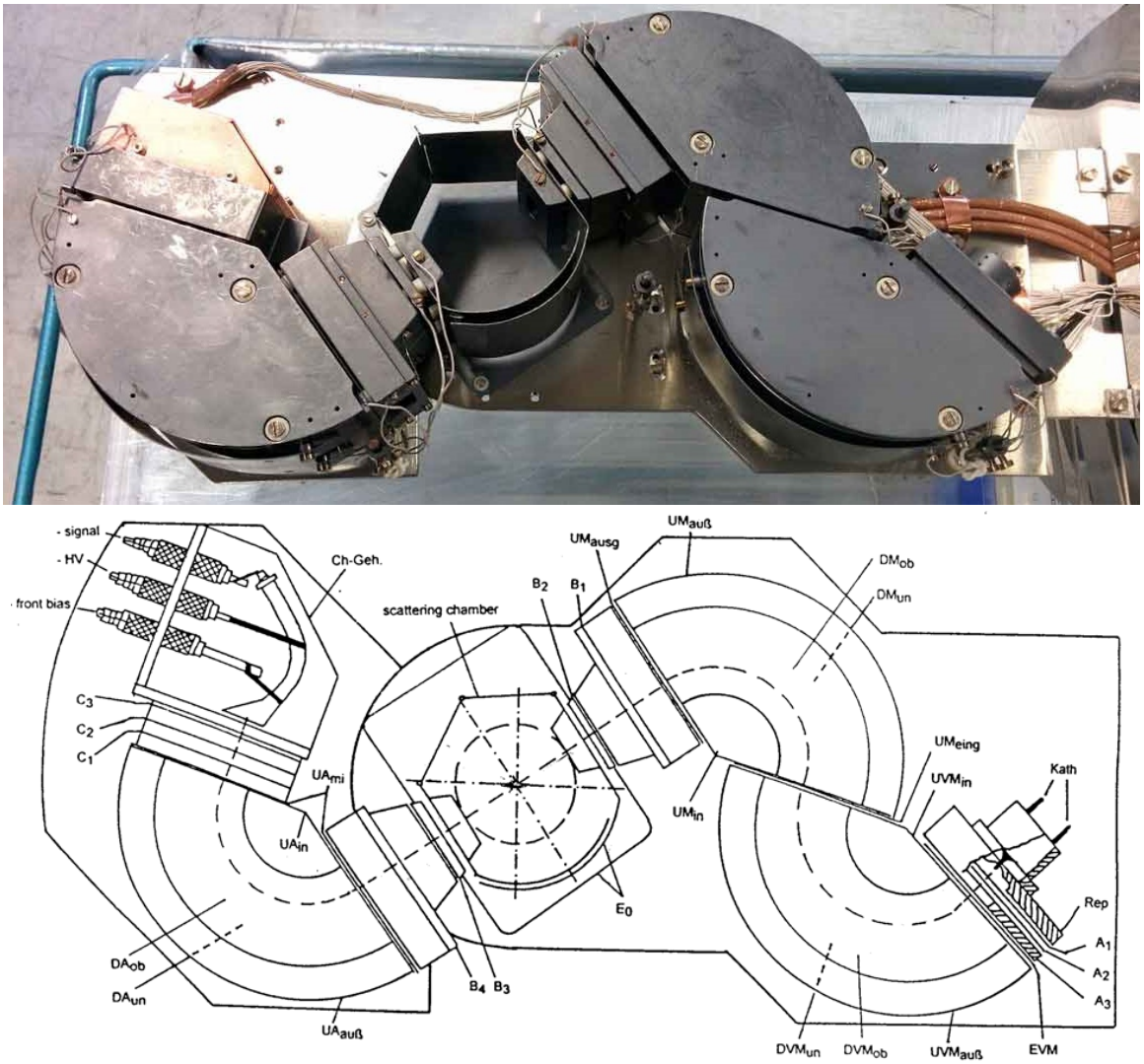


Figure 3.8 – Picture and schematics of the HREELS Delta0.5 produced by Specs.

The analysing stage is another dispersing stage and the passing energy is linearly varied during the acquisition in order to span all the possible energies of the electrons scattered from the sample. These electrons are eventually counted using a channeltron, a high efficiency electron multiplier, which converts them into detectable current pulses.

The signal coming from the detector is filtered, preamplified and it is delivered to the signal processing unit and finally it is recorded on the computer.

The resulting HREELS spectra are a graph plot of the number of detected electrons per energy loss.

An in specular spectra usually consists in the main peak, the elastic peak, centred at 0 meV energy loss, which is due to the elastically reflected electrons, and other peaks, which can be wide or narrow but are typically weaker than the elastic peak and are due to the anelastically scattered electrons. These electrons have lost some energy in the interaction with the sample

and the energy difference respect to the incident electrons corresponds to the energy of the excitation which has been activated.

Figure 3.9 shows an example of a HREELS spectrum for a G/SiC(0001) sample taken in in specular conditions ($\vartheta_{in}$= $\vartheta_{out}$=55°) with a primary electrons energy of 12 eV.

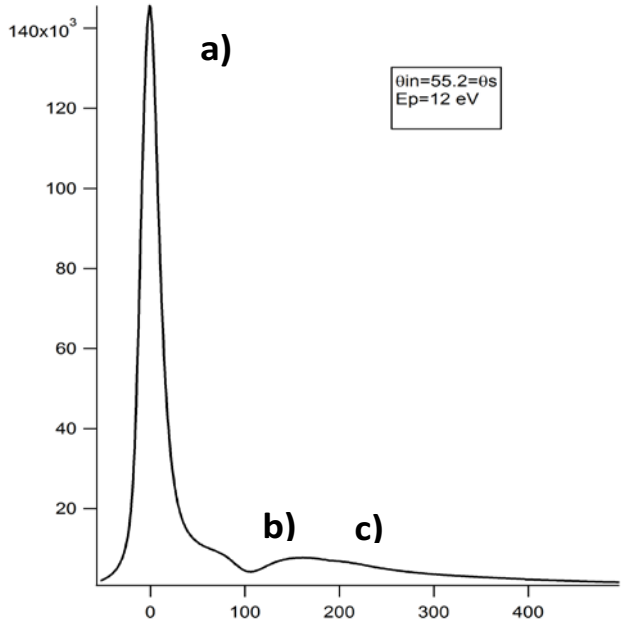


Figure 3.9 – Example of HREELS spectrum for a clean G/SiC(0001). The measure is taken in-specular with an incidence angle of 55° and beam energy of 12eV. (a) elastic peak, (b) and (c) are two components of an hybridised electronic-phononic oscillation: the plasmaron

Three main features are visible in this HREELS spectra: a) the elastic peak, which is the most intense feature and centred at 0 meV energy loss; b and c) are the two components of a plasmaron, which originates from the hybridization of the Fuchs Kliewer of SiC and the acoustic plasmon of graphene.

The asymmetric shape of the elastic peak is due to the presence of losses at relatively low energy (some tens of meV), the so called Drude tail.

### 3.8.4 XPS – X-Ray Photoelectron Spectroscopy

X ray Photoelectron Spectroscopy is an analysis technique based on the photoemission of core electrons induced by X rays.

The sample is exposed to a beam of soft x rays. The photons can be absorbed from an atom of the sample, which is then excited. From the excited state different processes can occur: photoemission, Auger processes, electron hole pair creation and anelastic processes.

In a photoemission process, depicted in Figure 3.10, the excitation energy given by the photon is directly used to promote an electron from a core level to the conduction band, above the Fermi level. If the electron has enough kinetic energy to overcome the work function of the material, it can escape and can then be captured and analysed.

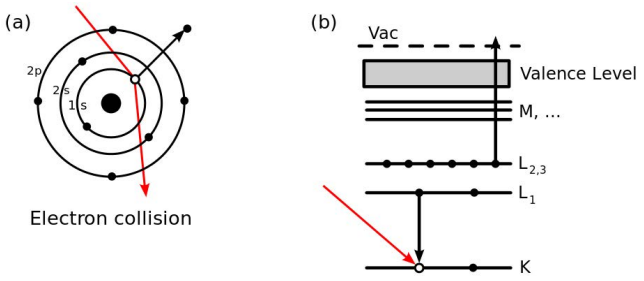


Figure 3.10 – Photoemission process: the photon (red) is adsorbed and a core electron from the K band is emitted

At the simplest single particle level, from energy conservation it follows that the kinetic energy $E_k$ for the electron is

$$E_K = h\nu - E_B - \phi$$

Where $E_B$ is the binding energy of the electron, $\varphi$ is the work function of the material and $h\nu$ is the energy of the electron. Since $h\nu$ (ad to some extent also $\varphi$) are known parameters, from the measure of $E_K$ we can obtain direct information on the binding energy of the atoms. This provides information on the atomic species present at the surface of the sample as each atomic species is identified by precise value of the binding energies of its electrons.

The electrons in the valence band are weakly bounded to the nucleus and thus are strongly influenced from the chemical environment near them. On the contrary, core electrons do not feel a so strong effect and show only a small variation (of the order of at most a few eV) of their binding energy, labelled as chemical shift or core level shift. Accurate measurement of this chemical shift provides information on the chemical environment around the different atoms and can be used, for example, to distinguish graphitic carbon bonded to form the gra phene layer ($E_B$ del C1s 285 eV [67]) from the carbidic carbon forming nickel carbide ($E_B$=283 eV [67]).

XPS is a surface science technique not because of the X rays, which can penetrate the sample for hundreds of atomic layers, but because the mean free path of the photoemitted electrons (having energy of 100 1000eV) is limited to few atomic layers: only the electrons photoemitted in proximity of the surface can leave the sample and then be detected.

The surface sensitivity can be enhanced by changing the geometry of the sample with respect to the electron analyzer and selecting grazing scattering angles.

XPS is a quantitative technique: the intensity of the photoemission peaks is proportional to the number of atoms of a certain specie excited by the beam and taking into accounts the sensi tivity factors for each element it is possible to estimate the concentration of the different species, although photoelectron diffraction and calibration problems can limit the attainable sensitivity.

Figure 3.11 – Detailed view of the DAR400 anode

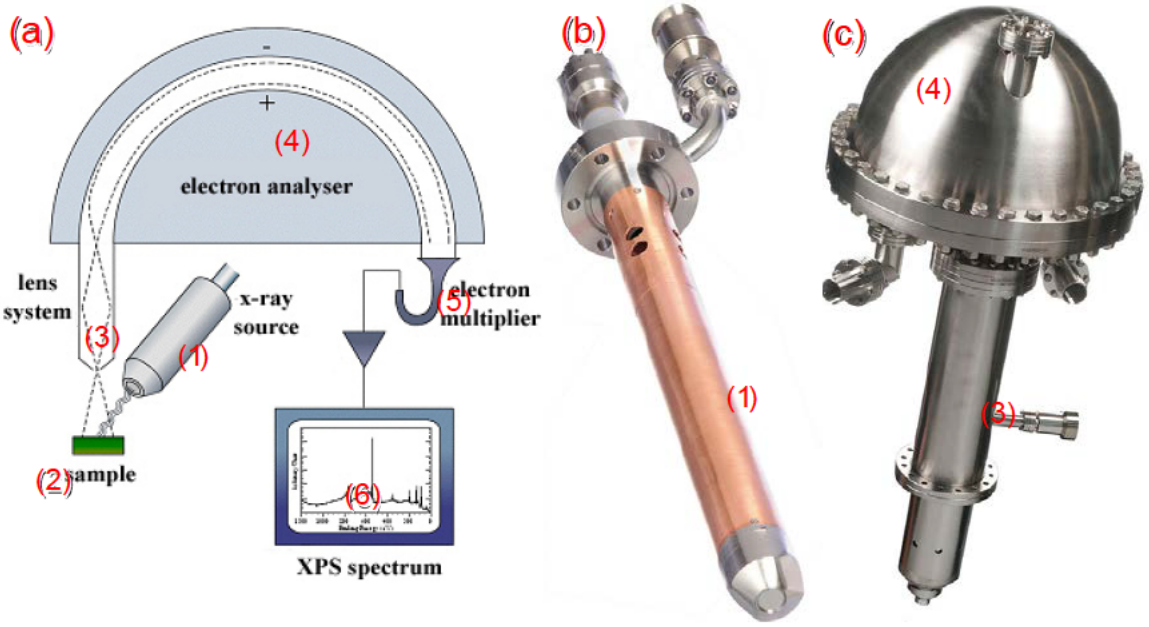


Figure 3.12 – (a) schematic drawing of an XPS spectrometer. Different parts can be identified: (1) the X-ray source, (2) the sample, (3) the electrostatic lens system focussing the photoemitted electrons into the (4) hemispherical electron analyser and only those having a desired energy value can reach the (5) electron multipliers being converted into detectable current pulses which are counted and recorded by the (6) data acquisition system. – (b) a picture of the Omicron DAR400 X-ray source and of the (c) Omicron EA125 hemispherical analyser installed on the Spectroscopy Chamber.

A schematic drawing of an XPS spectrometer is reported in Figure 3.12(a): the most important parts are the X ray source (Omicron DAR400) and the hemispherical analyser (Omicron EA125).

The DAR400 source produces the X rays by accelerating electrons emitted by an hot filament against an anode placed at the tip of the gun. The anode is divided into two sections which are coated with aluminium and magnesium respectively, in order to emit photons having two possible energy values: $h\nu$=1486,6 eV corresponding to the $Al_{K\alpha}$ band and $h\nu$=1253,6 eV corresponding to the $Mg_{K\alpha}$ band. Since the source is non monochromatized, the X ray radiation has a natural line width of 0.85 and 0.70 eV respectively for the two energies, and this is the main limiting factor for the energy resolution of the XPS spectra.

The availability of two different photon energies is a common characteristic of XPS X ray sources because it is useful to have to distinguish between photoemission and Auger peaks: indeed, in photoemission processes $E_B$ is constant while in Auger processes $E_K$ is constant. Thus, when doubt arises in the assignment of a peak, switching the photon energy can be of great help.

A set of electrostatic lenses collects, focusses and accelerates the photoemitted electrons towards the hemispherical analyser. A set of slits is available at the entrance of the analyser, which can be used to filter out part of the electrons reducing the collection spot size if more spatial resolution is required.

Only electrons having the desired $E_0$ energy value can pass through the analyser to reach the detection system, consisting of five channeltrons. The energy resolution of the analyser can be set by changing the *pass energy* $\Delta E$, that is the energy range (around $E_0$) of the electrons which are allowed through the analyser: the lower $\Delta E$, the higher is the resolution ($E_0/\Delta E$), but the lower is the attainable count rate. The value of $\Delta E$ = 22 eV has proved as the best compromise in our conditions.

An example of an XPS spectrum is reported in Figure 3.13 (red curve): a wide energy range scan for a graphene film grown on Ni(111). Such a large energy range (0 1000 eV) is used to investigate the presence of all the chemical species.

The main features are quickly identified: an intense doublet is due to the nickel substrate (853 eV) and also the three Auger peaks between 650 and 800 eV. No peak is detected around 530 eV which means that no oxygen is present on the sample while the small peak at 285 eV is the fingerprint of the graphene layer.

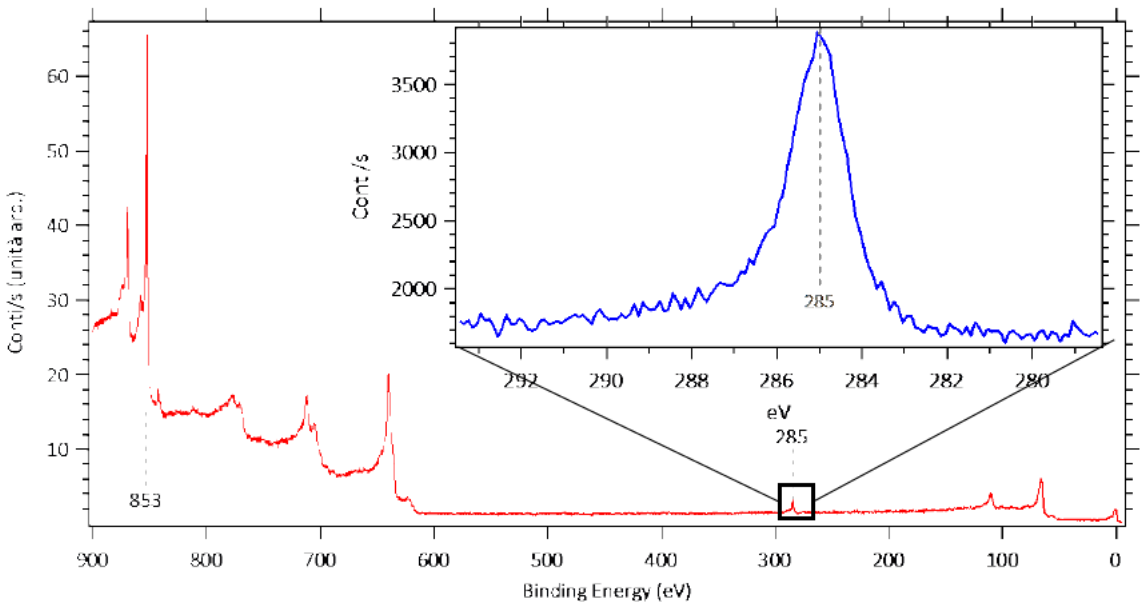


Figure 3.13 – Example XPS spectra: a wide energy scan (red) and an high-resolution section centred on the C1s peak (blue)

Having identified the chemical species of interest, high resolution scans can be collected for shorter energy ranges, obtaining spectra like the inset in Figure 3.13, centred around the C1s region which can be analysed in detail. The peak position, centred at 285 eV allows the unambiguous identification of graphitic carbon, which testifies the presence of the graphene film.

The XPS spectra must be calibrated using known reference values which must not show any significant core level shift during the experiments. In this particular case the reference value is the main peak of nickel ($Ni2p_{3/2}$ = 853 eV) since most of the signal comes from the bulk of the sample and is thus not influenced by the presence of the graphene layer or other species.

### 3.8.5 STM – Scanning Tunneling Microscope

The Scanning Tunneling Microscope was firstly developed in 1981 by G. Binning and H. Rohrer who received the Nobel Prize in Physics in 1986 for this discovery. In a short time, it has become one of the most used techniques in surface science. The STM is based on the tunnel effect: a metallic tip is brought a few angstroms away from the surface of the sample (which must be a metal or a semiconductor). A bias ranging from few meV to few volts is applied between them and even if there is a potential barrier between the sample and the tip, an electric current can be measured. This current is forbidden in a classical picture since the electrons do not have enough energy to overcome the energy barrier. But from quantum mechanical principles we know that the wavefunction of the sample and of the tip do extend inside the barrier though decaying exponentially: if the distance between them is short enough the evanescent functions overlap enough that there is a significant probability for an electron to pass through via tunnel effect.

An approximated expression for the tunnelling current in the low bias limit, i.e. for the tunnel ling conditions used in the present Thesis, is:

$$I(z) \propto eV_B \exp\left(-2\frac{\sqrt{2m\Phi}}{\hbar}z\right)$$

Where $V_B$ is the bias voltage, e and m are charge and mass of the electron, z is the distance between sample and tip, and $\Phi$ is the work function of the sample. The tunnelling current is typically of the order of pA or nA and depends exponentially on the distance between sample and tip, changing of about an order of magnitude for a change of only 1 Å in the distance z.

This means, for example, that when measuring a typical atomic diameter of 0,3 nm the tun nelling current changes about three orders of magnitude, and this high sensitivity is fundamental for the STM.

Two operating modes are possible for the STM: constant current or constant height.

In the first mode the tunnelling current is measured and kept constant by a feedback system which changes the distance z between tip and sample. The surface is thus mapped by mapping the distance value (z) for each coordinates pair (x,y).

The other option is to keep the distance constant and monitor the tunnelling current: this operating mode is however less common. The presence of defects, steps etc on the surface would indeed lead to frequent crashes of the tip with the surface.

The map created with the STM is a direct map of the *integrated* local density of states (LDOS) near the Fermi Energy. Conversion from LDOS to the topological map is nontrivial and depends on the electronic properties of the surface. The correspondence is high for good conductors like metals, while it is more complex for semiconductors due to the presence of dangling bonds. It follows that molecules adsorbed on the sample can exhibit either a decreased or an increased LDOS appearing like holes or protrusions with respect to the clean surface.

To obtain the extreme lateral resolution necessary to reconstruct a map with atomic precision, very high accuracy and stability are required while moving the tip, and the motion system is based on piezoelectric crystals with different possible realizations evolved during the years.

The LS STM I used was manufactured by Createc and based on a project by K. Schaeffer, S. Zophel e G. Meyer. A picture of the scanner (modified Besocke type) is shown in Figure 3.14: four different piezos are used for moving the tip. The tip itself is magnetically attached to a central piezo fixed on a rotating structure supported onto the three other piezos. The rotating structure is divided into three 120° sectors which are machined to form three ramps linearly thicker with the angle. Moving the lateral piezos with a sawtooth signal it is possible to obtain a rotation of the structure with a stick and slip motion. This movement is the “coarse” movement ranging up to 1 mm. The fine movement is fully managed by the central piezo, which can extend or contract along the z direction and even flex in order to control the x y movement of the tip.

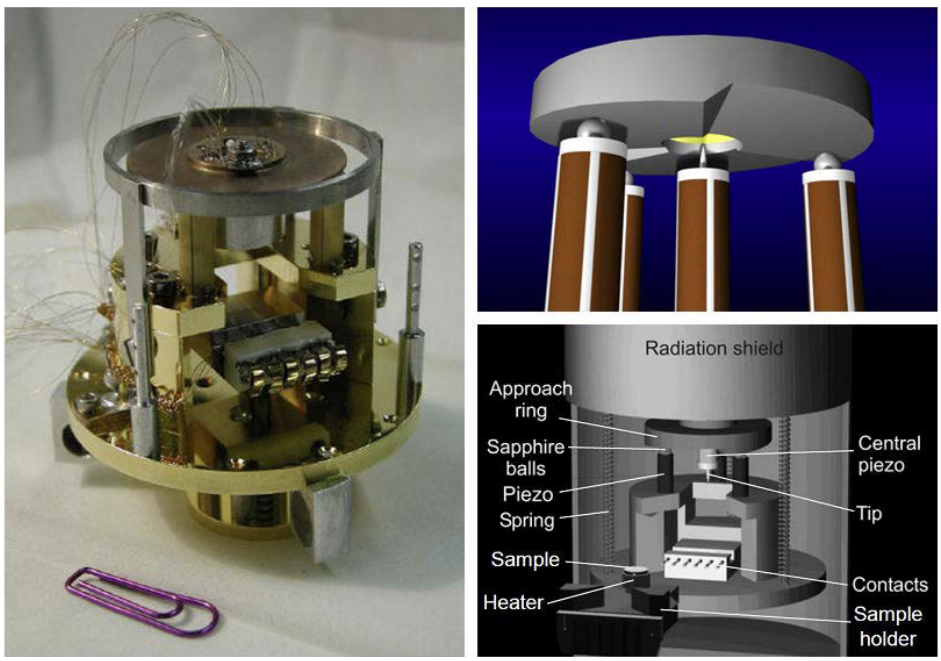


Figure 3.14 – A picture (left) and a scheme (right) of the STM with a detail of the motion system (right top)

The motion of the tip, the feedback system and the data acquisition are controlled by a software provided by the manufacturer together with a digital control unit, which is also provided with a dedicated lock in system for spectroscopy measurements (Scanning Tunneling Spectroscopy – STS).

The whole STM is decoupled from the UHV chamber in order to reduce the vibrations by hanging inside the chamber suspended on calibrated springs inside a magnetic dampener. The whole chamber is also suspended on pneumatic damping feet.

All these measures are needed to achieve the lateral resolution of approximately 1 Å while the vertical resolution can be pushed to 0.03 Å.

The STM can be cooled to liquid nitrogen or liquid helium temperature. To maintain the low temperature the STM is placed inside a double cryostat. A Zener diode is installed in order to measure the temperature in the required range. The usual working temperature is 80 K if only liquid nitrogen is used and about 6 K if also liquid helium is used.

The main advantages of working at low temperature are:

1. The cold walls of the cryostats work as cryogenic pumps thus the vacuum inside the cryostats is enhanced by more than two orders of magnitude respect to the base vacuum level of $10^{-10}$ mbar. Consequently, once the sample is placed inside the STM, the surface is kept clean for many days enabling long measurement sessions.
2. Thanks to the reduced thermal drift the stability of the STM improves with lower temperature, allowing to study the dependence on the bias voltage of the same area of the sample without needing any tracking system.
3. A temperature of 6 K is necessary in case of STS measurements in order to reduce the thermal noise contribution.
4. Additionally, adsorbates with low diffusion barriers can be investigated only at low temperature when their diffusion is suppressed.

# 4 Adsorption of CO on Graphene on Ni(111) and Graphene on $Cu_{poly}$

## 4.1 Introduction

We have investigated the role of substrate in determining the chemical reactivity of graphene. To this purpose we have compared adsorption of CO, a prototype molecule characterized by a large dipole moment and thus detectable also at low concentrations, on graphene grown on Ni(111) and for a graphene on a copper foil.

We also investigated the dependence of the reactivity of the G/Ni(111) system on the particular phase formed: it is indeed well known that the G/Ni(111) layer is not uniform, but C atoms occupy different sites, forming domains with either top fcc, top–bridge or the less stable top hcp geometry. Such configurations are characterised by different distances from the substrate and different bond strengths and their relative abundance depends on the growth parameters [67,68]. In addition, at high temperature, rotated G domains may form. Finally, on Ni(111) the alternative mechanisms of nickel carbide formation and carbon dissolution into the bulk may compete with G growth in a way which depends on both pre growth treatments and growth temperature [15].

As already mentioned, different adsorption configurations exist for graphene on Ni(111). Combined high resolution XPS experiments and DFT [67] calculations indicate that, in the most stable geometry, the two C atoms of the G unit cell occupy top and fcc sites of the underlying Ni(111) lattice; this configuration is referred to as top fcc. A nearly iso energetic assembly corresponds to C atoms in top and bridge sites (top bridge) [67], while the condition in which C atoms sit in top and hcp sites (top hcp) is slightly less stable. A schematic representation of these three configurations is reported in Figure 4.1.

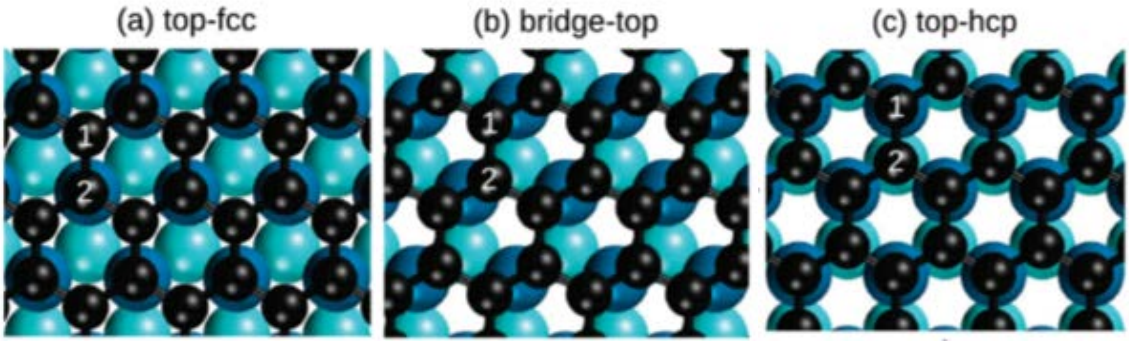


Figure 4.1 – Schematic representation of the different graphene configurations on Ni(111): (a) top-fcc, (b) top-bridge and (c) top-hcp. Adapted from [67]

The different graphene configurations are characterized by small differences in the C 1s line shapes, which can be distinguished easily in high resolution XPS experiments performed with Synchrotron Radiation. Indeed, graphene in top fcc geometry is characterized by a doublet in

the C 1s region at 285.1 eV and 284.2 eV; the top bridge and top hcp domains, on the contrary, present XPS spectra with a single component centered at 284.8 eV and 285.3 eV, respectively [67]. Though it is not possible to resolve such contributions with a conventional laboratory X ray source, their relative weight modifies the shape of the photoemission peak and the position of its maximum, so that useful information can be extracted by fitting the C 1s peak. A careful calibration of the energy scale is necessary for this scope and was obtained by using the Ni(2p) peak of metallic Ni (free from dissolved C) as a reference [69].

The core level shifts of the two non equivalent C atoms (C1 and C2) with respect to free standing graphene have been estimated theoretically [67] and are reported in Table 4.1.

| Configuration | Core level shift of C1 (eV) | Core level shift of C2 (eV) |
|---|---|---|
| **Bridge-top** | 0.40 | 0.36 |
| **Top-fcc** | 0.63 | 0.19 |
| **Top-hcp** | +0.30 | +0.31 |

Table 4.1 - Theoretically estimated core level shifts for the two inequivalent carbon atoms for the different configurations of G on Ni(111). Data taken from ref [67].

## 4.2 Experimental

The Ni(111) crystal is cleaned by repeated sputtering (with 3 keV Ne ions) and annealing (T=1283 K) cycles. In addition, for a more efficient removal of C dissolved in the near surface region, several cycles in which the sample was exposed to ~2.5 L of $O_2$ at T= 673 K and then annealed to 783 K under UHV conditions were performed before the first preparation and whenever required (in particular before growth with protocol 823 K DD2 (see below).

G is grown in situ, by thermal dehydrogenation of ethene catalysed by the Ni surface exposing the substrate at $T_g$ for the preparation time.

The substrate growth temperature ($T_g$) was varied between $T_g$=753 K and $T_g$=873 K, for the different growth protocols. Ethene was introduced into the UHV chamber through a doser placed ~1 cm away from the Ni(111) surface. Under these conditions, we estimate an increase in the local pressure of approximately a factor of 5 with respect to the value measured in the UHV chamber [70]. The substrate was exposed to ethene for 660 sec either at P= 5 $10^{-6}$ mbar (~2500 L, referred to as single dose – SD – in the following) or at P=1.0 $10^{-5}$ mbar (~5000 L, double dose DD). The sample was kept eventually at $T_g$ for 10 minutes after pumping ethene off. Alternatively, G was obtained by segregation of C atoms dissolved in the bulk by annealing the clean Ni(111) crystal to 788 K for 30 minutes in UHV.

The main protocols tested are reported in Table 4.2. Such growth processes result in single layer graphene domains up to a few tens of nm in size as verified by Low Temperature Scanning Tunnelling Microscopy (LT STM). The cleanliness of the surface and the chemical nature of the carbon layer obtained are checked by X ray Photoelectron Spectroscopy (XPS). The binding energy, Eb, was calibrated on the metallic Ni $2p_{3/2}$ line which, in absence of dissolved carbon,

is located at 852.6 eV [71,72]. Detailed analysis of the C 1s region was performed by fitting the photoemission signal with different contributions.

| Growth protocol | Temperature Tg (K) | Dosing Pressure (mbar) | Growth time (s) | Ethene dose (L) | Post annealing (s) |
|---|---|---|---|---|---|
| **753 K SD** | 753 | $5\,10^{-6}$ | 660 | 2500 | 600 |
| **823 K DD1** | 823 | $1\,10^{-5}$ | 660 | 5000 | 600 |
| **823 K DD2** | 823 | $1\,10^{-5}$ | 660 | 5000 | 600 |
| **873 K DD** | 873 | $1\,10^{-5}$ | 660 | 5000 | 600 |
| **Segregation** | 688 | | 1800 | | |

Table 4.2 - Growth parameters for the different G/Ni(111) layer preparation protocols.

CO is dosed by backfilling the chamber. High Resolution Electron Energy Loss Spectroscopy (HREELS) is used to monitor CO adsorption while LT STM allows the morphological characterisation of clean and adsorbate covered G layers. HREEL spectra were recorded in specular, with incidence angle $\theta_i=\theta_f = 62°$ with respect to the surface normal and with primary electron energy E= 4 eV. In order to allow for a reliable comparison of the different spectra, the measured intensity (Imeas) is normalized with respect to the average intensity of the inelastic tail in the flat region between 400 meV and 500 meV ($\langle I[400; 500]\ \mathrm{meV}\rangle$). STM images were acquired in constant current mode, with typical tunnelling currents of $85 \leq I \leq 600$ pA and bias voltages (of the sample with respect to the tip) of $-0.2\ V \leq V \leq 0.2\ V$.

## 4.3 Results and discussion

After growing graphene layers under the different conditions summarized in Table 4.2, we have tested their chemical reactivity towards CO. The samples were exposed to 400 L of CO at room temperature and no trace of CO adsorption was ever detected. We thus conclude that the graphene layers we obtained are inert towards CO at room temperature, regardless of the growth protocol used, and also that the reactive nickel substrate is completely covered by graphene. In fact, the presence of bare Ni patches would result in CO adsorption at RT since for coverage lower than 0.4 ML CO desorption off Ni(111) occurs between 430 and 450 K [73] or around 412 K, according to a more recent paper [74].

We then cooled down the samples to 87 K and exposed them to 40 L of CO. Figure 4.2 shows the outcome for the different samples.

Stable CO adsorption occurs on all the samples, as witnessed by the presence of a CO stretch vibration around 256 meV. The attained coverage depends on the preparation protocol; in particular it is largest for the films produced at $T_g$=823 K and significantly lower for the films pro-

duced at higher or lower temperature. However, two nominally identical preparations (addressed as 823 DD1 and 823 DD2) exhibit remarkably different reactivity towards CO. This important point will be discussed further in the following.

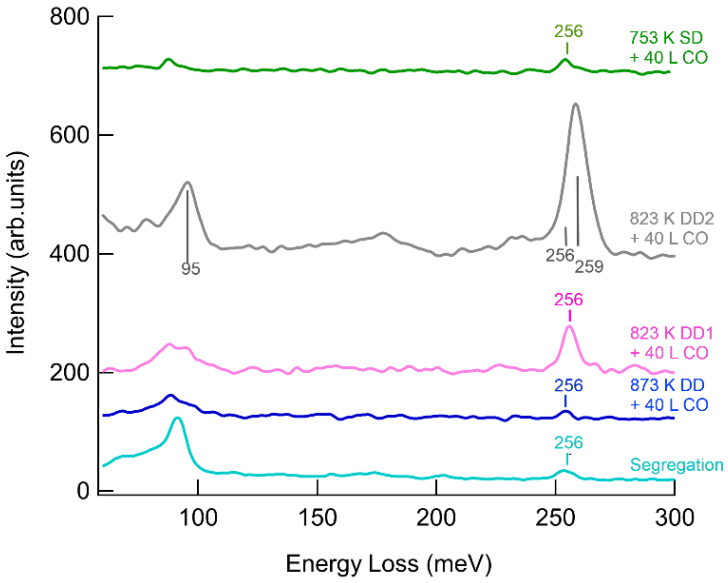


Figure 4.2 – *HREEL spectra recorded after exposing G/Ni(111) layers prepared following the different protocols and cooled at 87 K to 40 L of CO.*

The peak around 90 meV, present in all the spectra, corresponds to the $H_2O$ libration mode and is indicative of little water contamination; most likely, due to unwanted adsorption from the residual gas. Since the intensity of such energy loss is not correlated with the amount of adsorbed CO we conclude that water acts as a spectator, and we shall not discuss it further.

HREEL spectra for CO on Ni(111) exhibit one feature at 236 meV for exposure at 150 K and a doublet at 233 and 250 meV for exposure at RT, the feature at 233 meV being the most intense [75], contrary to the outcome of the present experiment in which no loss around 230 meV is observed, thus further supporting our conclusion that no bare Ni patches are present.

In order to understand the reasons of the differences in reactivity observed for our films, we analyze the X ray photoemission spectra for each of them recorded before CO exposure. XPS spectra were recorded at RT to prevent uncontrolled CO adsorption from the background pressure. The raw data are reported in Figure 4.3A. The spectra of the C 1s region corresponding to the different preparations are present a single peak centered at 284.6 eV. They present small differences in shape and intensity, which are associated to the different relative amount of G in top bridge, top fcc and top hcp configuration, as well as to the amount of nickel carbide ($Ni_2C$) present at the surface.

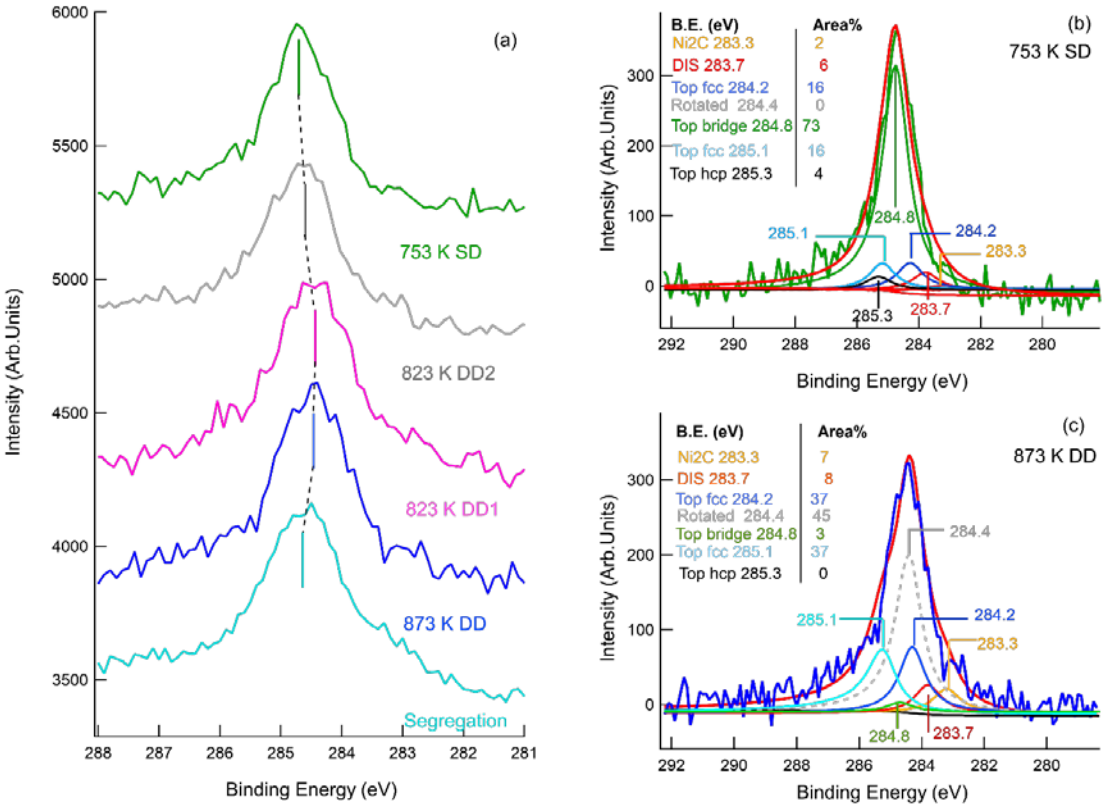


Figure 4.3 – *XPS spectra of C1s region of all preparations (panel a). Example of the result of the XPS fitting procedure shown for SD and DD preparations at 753 K and 873 K (panel b and c, respectively): Top hcp component (black), top fcc (blu and light blu), top bridge (green), rotated graphene (gray),dissolved (red) and $Ni_2C$ (orange).*

By cross comparison of the XPS spectra with the theoretically estimated core level shifts reported in Table 4.1 it is apparent that:

a) A significant fraction of domains with top fcc configuration determines a shift toward lower BE (with respect to free standing graphene) of the centroid of the C 1s feature, since the top fcc configuration has a contribution with a core level shift (CLS) of 0.63 eV and the average CLS of the two components is 0.41 eV;
b) A significant fraction of domains with top bridge con figuration causes a (smaller) shift toward lower BE of the centroid because the average CLS is 0.38 eV;
c) Domains with top hcp configuration cause the presence of extra intensity (i.e., a shoul der) at higher BE since the average CLS of this component is +0.31 eV;
d) A significant amount of $Ni_2C$ and of dissolved carbon determines extra intensity at lower BE;
e) A larger width of the C 1s suggests the presence of significant fraction top fcc domains which are characterized by the largest difference in the CLS of the two inequivalent carbon atoms.

From such qualitative arguments we can expect a relatively larger fraction of top fcc domains to be present for the 823 K D1 ad 873 K DD protocols which exhibit the most negative shift of the centroid and a relatively lower amount for the 753 K and segregation protocols, which are

characterized by a centroid shifted towards higher $E_B$. The comparison of the extra intensity present on the lower binding energy side also provides evidence for the presence of a larger amount of dissolved C (and/or of $Ni_2C$ domains) for the segregation protocol.

A more quantitative assessment can be obtained by properly fitting the XPS spectra [76]. As we shall see the conclusions obtained from the fit agree with the qualitative considerations presented above.

The experimental curves are fitted as the superposition of several components (see Figure 4.3B and Figure 4.3C reportd as example):

a) a Shirley background [77] is removed
b) a doublet at 285.1 eV and 284.2 eV corresponds to graphene in top fcc configuration (light blue and blue traces)
c) a single component at 284.8 eV due to the top bridge configuration (green curve)
d) another single component at 285.3 eV due to the top hcp G (black trace)

Other additional components present in small amounts are:

e) rotated graphene at 284.4 eV (grey curve) [28]
f) $Ni_2C$ at 283.3 eV (orange curve) [69]
g) dissolved C at 283.7 eV (red curve) [69]

Slightly different vaues of the components with respect to the values given in literature are required to ensure the convergence of the fit.

We remind that two different processes contribute to the growth of G on Ni(111), their relative importance being determined by the temperature of the sample and by the amount of dissolved carbon present in the bulk [15]. The former growth mode is operative at the highest temperature and directly yields graphene from ethene decomposition. The latter process proceeds via the formation of nickel carbide ($Ni_2C$). Segregation of C may also play a role if a significant amount of C is dissolved in the bulk of the sample [68,78]. For these reasons, we introduced in the fitting procedure two additional components at 283.3 eV (orange curve) and at 283.7 eV (red curve), corresponding to $Ni_2C$ and dissolved C, respectively. [15,69]

The outcome of the fitting procedure over all the investigated samples is summarised in the histograms of Figure 4.4. Panel A shows the total amount of carbon, obtained by taking in account the total area of the C1s peak. The total XPS intensity is strongly variable, with a maximum difference of ~30% between the smallest and the largest values. Panel B reports the different graphenic (top hcp, top bridge, top fcc) and non graphenic ($Ni_2C$ and dissolved C) components for each film. For the preparation at 873 K DD, an additional contribution of rotated graphene ($E_b$=284.4 eV [15], a species which forms especially above $Ni_2C$) is also considered. Finally, in panel C we plot the CO stretch peak intensity detected by HREEL and normalized to the inelastic background measured after 40 L exposure at 87 K.

The following considerations arise:

a) First of all, it should be noted that the information retrieved by XPS spectra recorded at RT is representative of the conditions present at 87 K, the temperature used for CO adsorption. Indeed the amount of $Ni_2C$ and of dissolved C is not expected to change below RT since diffusion and conversion of carbide into G are quenched. On the other hand, the relative population of the different G configurations can change with crystal temperature. The top fcc component is found to increase by less than 15 % when decreasing the surface temperature from 300 K to 150 K [67]. Whether the trend persists until 87 K, i.e. at the temperature of our experiments, is not known and cannot be determined with a non monochromatized X ray source. Therefore, the relative concentration of the different G moieties estimated at RT represents a lower limit for the top fcc species and an upper limit for the top bridge one (which must show the opposite behavior in order to conserve the total G coverage).
b) The spectra with the highest carbon content correspond to those with a significant amount of nickel carbide and/or of dissolved carbon, as estimated considering an escape length of the photoemitted electrons of ~5 nm. This indicates that the surface is covered almost entirely with single layer graphene with a maximum contribution of the bilayer amounting to 15%. The extra estimated 15% of C is due either to $Ni_2C$ or to dissolved C in the bulk. The amount of adsorbed CO present after 40 L dose at 87 K decreases when the amount of non graphenic carbon increases.
c) The amount of graphene in top hcp configuration is very small and decreases with increasing temperature in agreement with DFT calculations, which predict it to be less stable than top fcc and top bridge graphene.
d) The two preparations at 823 K DD1 and DD2 are not equivalent. They correspond to G layers grown either on a Ni substrate obtained following a “standard” cleaning procedure (823 K DD1, pink trace in Figure 4.2A) or prepared by repeated sputtering and annealing cycles to deplete the near sub surface Ni layers from dissolved C (823 K DD2, grey trace). As evident in the chart of Figure 4.4B, these two layers are characterized by a quite different amount of $Ni_2C$, of dissolved C and of top fcc graphene; in both cases top hcp G is missing and top bridge G is present in similar amounts. The remarkable difference in reactivity indicates, on the one hand, that the presence of $Ni_2C$ and/or dissolved C inhibits CO adsorption, on the other hand that top bridge G is not the reactive species. This comparison proves, therefore, that top fcc G is the most reactive phase. Analysis of the composition of the C1s line for the 753 K SD and 823 K DD1 and DD2 samples confirms this statement: despite the fact that the 753 K SD preparation has twice as much G in the top bridge configuration than both the 823 K DD1 and 823 K DD2 protocols, the former layer is significantly less reactive than the latters
e) The reactivity of G obtained by the 753 K SD protocol, despite the lower amount of top fcc G, is slightly higher than for G obtained by segregation and for the 873 K DD. Since the preparation at 753 K SD presents a lower amount of $Ni_2C$ and of dissolved C, this

indicates that the reactivity is not only a function of the amount of top fcc G or non graphenic carbon alone, but it depends on a combination of the two parameters.

Rotated graphene is inert, since the reactivity of the 873 K DD sample, the only one in which rotated G domains are present in detectable amount, is low.

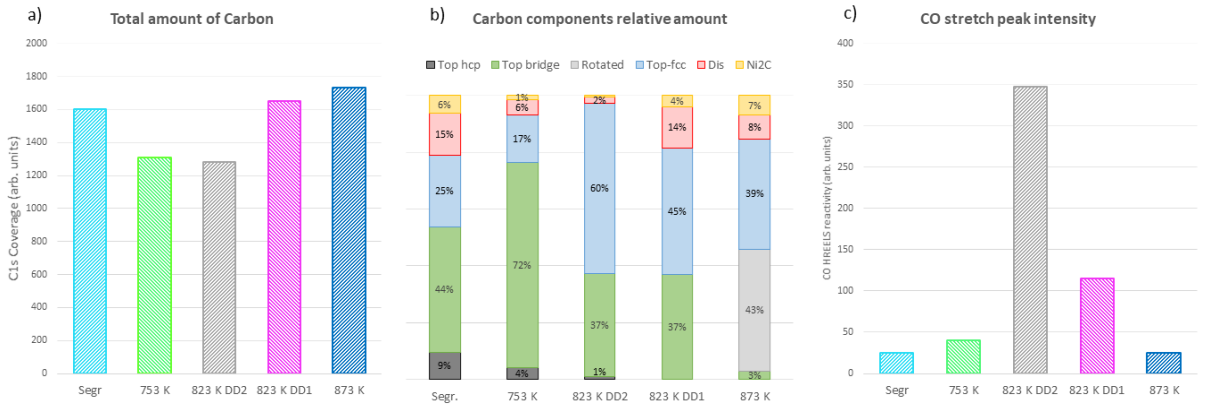


Figure 4.4 – *Histograms summarizing the results of the fitting procedure on the XPS spectra of* Figure 4.3. *a) total amount of C, b) partitioning of the C 1s intensity into the different graphenic (top-hcp, top bridge, top fcc) and non graphenic ($Ni_2C$ and dissolved C) components; c) intensity of the CO stretch peak detected in the HREEL spectra of* Figure 4.2, *normalized to the inelastic background, after 40 L exposure at 87 K.*

The qualitative considerations summarised above are supported by inspection of the graphs reported in Figure 4.5. It is evident that the reactivity is not directly correlated with the amount of top bridge G (panel A) and top fcc G (panel B). On the contrary, it reasonably correlates with the amount of top fcc/$Ni_2C$ ratio (panel C).

Though discriminating between the effect of $Ni_2C$ and of dissolved C is not straightforward, a poisoning effect of the former species seems more reasonable for two reasons. First, $Ni_2C$ is located either on the surface or immediately below the rotated graphene domain, while dissolved carbon may be diluted over several Ni layers and thus it might not affect the reactivity of the adlayer. Secondly, due to stoichiometry, a 6% coverage of $Ni_2C$ corresponds to 24% of the substrate area; therefore, it is not unreasonable that the presence of a limited carbide signal influences significantly the overall reactivity.

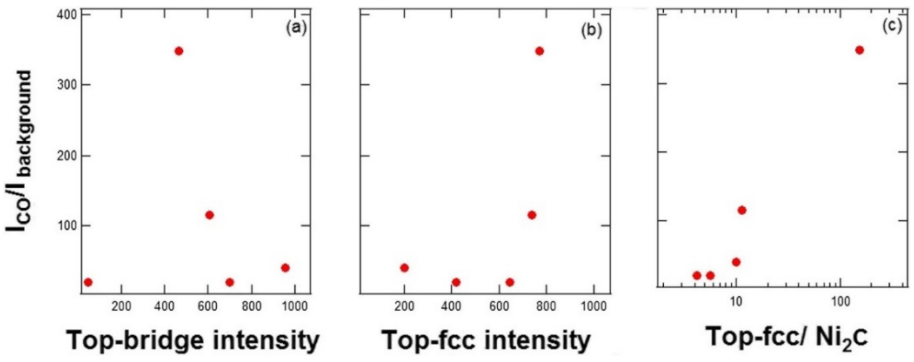


Figure 4.5 – Intensity of the CO stretch feature (normalised to the inelastic background) vs. intensity, normalited to the backround, of the top-bridge component (a), of the top-fcc component (b), and of the top-fcc/$Ni_2C$ ratio (c).

A closer inspection of the HREEL spectra recorded for the 823 K DD1 and 823 K DD2 samples shows a different CO stretch frequency in the two cases. To better understand the phenomenon,in Figure 4.6 we compare the spectra recorded after subsequent exposure of these layers to 1 L and 40 L of CO at 87 K. In both cases the CO stretch vibration at 256 meV is already evident after 1 L of exposure, its intensity being only slightly larger for the C depleted sample (823 K DD2). Increasing the exposure to 40 L CO causes an increase in the intensity of the loss by more than a factor of three for the 823 DD2 sample, leaving the spectrum for the 823 DD1 nearly unaffected. The increase in the intensity of the CO stretch for the C depleted sample is accompanied by a 4 meV blueshift of the CO stretching frequency. These observations indicate that a higher local CO coverage is obtained for $T_g$=823 K on the C depleted sample and that such molecules vibrate at a higher frequency due to the stronger dipolar interaction. Possibly the increase in the CO stretch frequency which approaches the gas phase value, correlates also with a signficant decrease in the adsorption energy with increasing coverage.

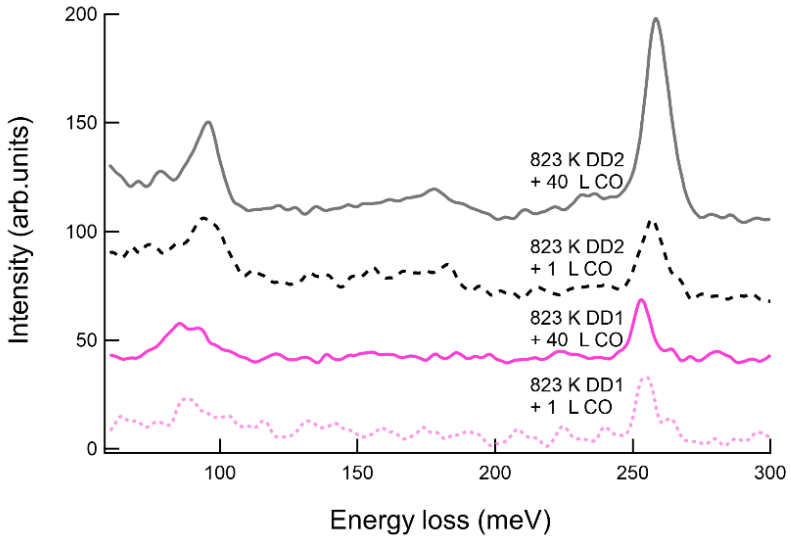


Figure 4.6 - *Comparison of the HREELS spectra recorded after different CO exposures for films grown at 823 K DD on the C-rich (pink spectra) and C-depleted (black spectra) Ni(111) substrate. Dotted traces refer to 1 L of CO exposure, continuous ones to 40 L of CO.*

From the analysis of our data we can thus conclude that the reactivity of single layer graphene on Ni(111) is mostly due to its top fcc component and this should not come as completely unexpected. Since the reactivity of G is determined by the nature of the substrate, we can easily imagine that the most reactive carbon atoms are the ones closest to Ni atoms. In top fcc graphene, 50% of the C atoms are in on top positions, thus pulled towards the substrate. In agreement with this explanation, the vibrational frequency of adsorbed CO is in the range expected for mono coordinated CO, i.e. for CO adsorbed at on top sites. The inertness of the top bridge and of the rotated graphene configurations (when present) agrees with this interpretation: despite the name, in the top bridge configuration both C atoms sit in bridge sites (see Figure 4.1) and the effect of the substrate is reduced.

We eventually concentrated our investigation on the most reactive preparation and we proceeded with a more detailed analysis in order to gain some additional information on the nature of the CO adsorption on G/Ni(111).

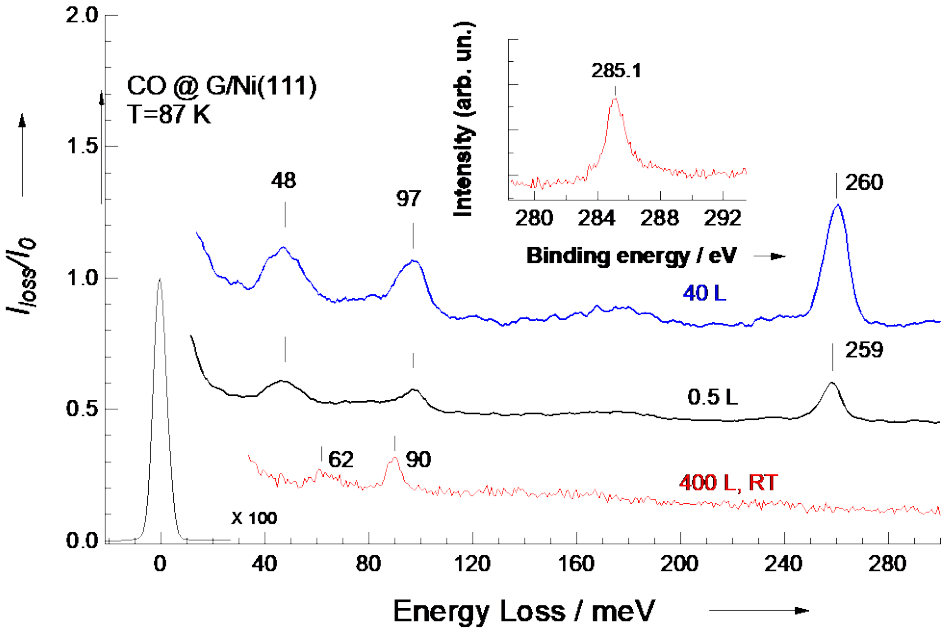


Figure 4.7 – HREEL spectra normalised to the elastic peak intensity after CO exposure. The spectra are recorded at the dosing temperature. Note the absence of CO related intensity when the sample is exposed at RT (bottom spectrum) and the CO related losses at 48 and 259 meV when the exposure is performed at 87 K (2nd and 3rd spectrum). The spectra are vertically displaced with respect to the bottom one for sake of clarity. The feature at 90 meV already present before dosing is assigned to the ZO phonon mode of graphene.[79] Such loss is excited by impact scattering being dipole-inactive. The loss at 62 meV is due to isolated carbon atoms adsorbed on Ni(111).[80] The feature around 97 meV is associated to a slight water contamination [81] .The inset shows the XPS spectrum of the C1s region of the clean G film.

The graphene layer was exposed to 400 L of CO at room temperature (red) and after 0.5 L and 40 L of CO at T=87 K (black and blue, respectively) and the results are reported in Figure 4.7. As already discussed no adsorption is detected at RT, while already a 0.5 L CO dose at T=87 K produces evident losses at 259 meV (internal CO stretch frequency, ν(CO)) and at 48 meV (CO surface stretch) [63]. Upon further exposure, the CO related losses increase, and the CO stretch mode frequency upshifts by 1 meV due to dipole dipole interaction [63].

We firstly note that the CO stretch frequency is lower than the value of ~265 meV appropriate for gas phase [82] and for physisorbed CO (e.g. on graphite [82] or Ag(111) [83]). Such lower value is indicative of weak CO chemisorption at on top sites [63]. The presence of a loss at 48 meV, which is suitable for the adsorbate substrate stretch of chemisorbed CO on a light substrate [63] definitely proves our assignment. The possibility that adsorption occurs on residual bare Ni patches is ruled out by the absence of reactivity at room temperature (Figure 4.7, bot tom spectrum). Adsorption on Ni is indeed observed in the case of incomplete G/Ni(111) layers and occurs then also at RT (not shown), giving rise to two CO stretch losses at 229 (bridge) and 250 (on top) meV and to a metal molecule stretch at 50 meV [84].

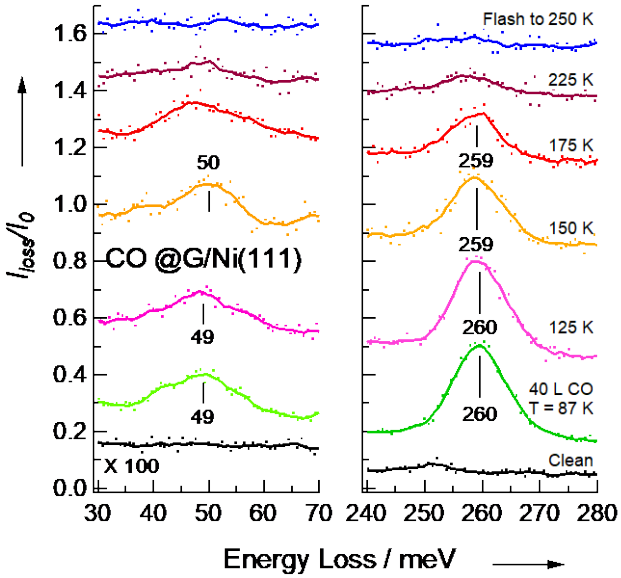


Figure 4.8 – HREEL spectra showing the CO-substrate (left) and the ν(CO) stretch (right) regions recorded after flashing the CO covered layer to the indicated temperatures and cooling back to 87 K. The attainable signal to noise ratio is limited by the need to keep the integration time short in order to avoid CO re-adsorption from the background.

After annealing the layer to increasingly higher T, the HREEL spectra evolve as shown in Figure 4.8. It is apparent that the CO stretch mode intensity is stable up to 125 K, it is halved after flashing to 175 K and disappears definitively above 200 K. The observed thermal stability is also in accord with weak chemisorption since physisorbed CO does desorb at significantly lower T (e.g. 55 K on Ag(111) [83]).

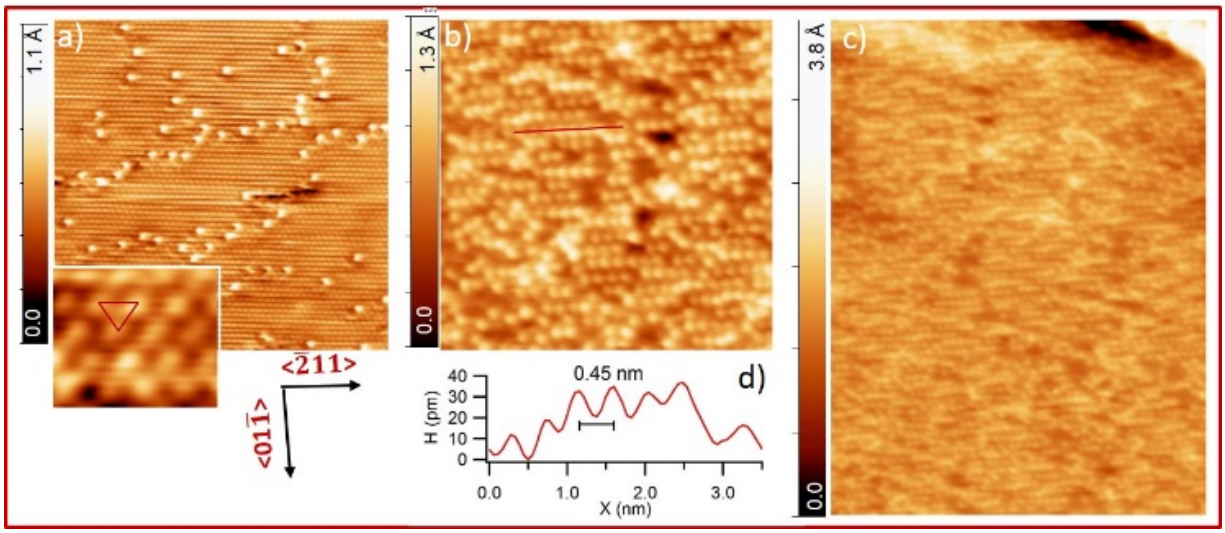


Figure 4.9 – Panel a) STM image of the clean G/Ni(111) surface. Image size: 11.3 x 11.3 nm$^2$, V=0.19 V, I=85 pA. The atomically resolved hexagonal lattice of the G layer is visible (see inset for an enlarged image; size: 10 Å x 8.5 Å, triangular unit cell marked). The brighter spots correspond to defects, as discussed in the text. The high symmetry directions of the Ni(111) substrate are reported below the image. b) G/Ni(111) after exposure to 1 L of CO dosed at 90 K. Image size: 11.3 x 11.3 nm$^2$, V=0.02V, I=0.55 nA. CO rows are mainly aligned along the <-211> direction. c) Larger overview of the same area reported in b), showing that the CO admolecules uniformly cover the whole graphene layer. Image size 21.2 x 28.3 nm$^2$. d) Line profile of one CO row cut along the red line marked in b), i.e. along the <-211> direction.

Figure 4.9 reports the outcome of the corresponding CO adsorption experiment monitored by Low Temperature Scanning Tunnelling Microscopy (LT STM). Panel a) shows a typical area of Ni(111) covered with a monolayer of pristine G. The high symmetry directions are marked below the image and the inset shows an enlargement in which the triangular symmetry typical of top fcc or top hcp graphene [15,67,76,85] is evident. The Ni surface is not covered only by one type of G, since areas with top bridge structure were also observed, as well as small regions in which $Ni_2C$ has formed. The pristine surface shows a series of brighter spots forming sorts of irregular chains on the surface, which correspond most probably to Stone Wales defects [86].

Being the defect site more reactive, their contamination by adsorption from the rest vacuum cannot be ruled out.

After 1 L CO exposure at T= 90 K, the aspect of the surface changes dramatically (see Figure 4.9b). Now it is fully covered by white dot features forming short chains mainly aligned along the

< 211> direction, see panel b. We identify them with CO molecules adsorbed at G domains. As evident from the large overview of panel c, CO is uniformly adsorbed on all the graphene film. The patches of $Ni_2C$ are, on the contrary, still bare being unreactive even at low T (image not shown).

The average distance between CO molecules in the same row is ~4.5 Å (see line scan in panel d). Although we are not able to determine the precise adsorption site of the molecule with respect to the graphene lattice underneath, this distance is well compatible with the adsorption of one CO molecule every second G unit cell. The packing in the perpendicular <01 1> direction is less regular. We observe, however, that the closest distance between adjacent CO rows is ~3.8 Å, which corresponds again to one CO unit every second G unit cell. We can therefore estimate a maximum local CO coverage of $1/6^{th}$ of monolayer (ML) in ML of G (1/3 in ML of Ni(111)). The global coverage is of course smaller, due to the irregular packing of the rows and to the presence of clean $Ni_2C$ areas.

Since in our experimental setup it is impossible to record STM images during exposure to CO, the areas imaged before and after CO uptake correspond to different regions of the surface. On the other hand, we cannot estimate the relative coverage of top fcc and top bridge G directly by STM since the number of images we recorded is not sufficient for a reliable statistical analysis. Unfortunately, it is also not possible to discriminate between top fcc and top bridge configuration by inspection of STM after exposure, so that our present conclusions rely on XPS data analysis only. However, since the majority of the areas, as imaged before dosing, correspond to top fcc graphene, i.e. to the configuration exhibiting the highest reactivity with CO, it is not surprising that we did not find bare graphene areas after exposure. Moreover, as already pointed out, the amount of top fcc G estimated by measuring XPS at RT is a lower limit to the concentration of top fcc present at 87 K, thus further justifying the non observation of clean G areas after CO exposure in the STM images.

In order to understand the role of the substrate/graphene interaction in the chemical reactivity of the supported graphene layer, we have repeated similar experiments on a graphene film grown on polycrystalline copper. The sample was grown ex situ by S. Agnoli (University of Padova, Department of Chemistry) by CVD using methane. Indeed, it was not possible to grow graphene on copper in our experimental apparatuses due to the high pressure needed.

Comparison between the sets of experiments is summarised in Figure 4.10. The spectra recorded for the pristine G/Ni(111) (black line in panel b) is quite flat and only vibrational mode detected is the ZO phonon, as previously observed. On the contrary, the graphene film grown on polycrystalline copper is populated of different peaks: a large CH stretch vibration centered around 360 meV and different $CH_3$ vibrational modes between 100 meV and 200 meV. These peaks come from non complete dehydrogenation of some methane molecules remaining after the film production.

While CO adsorption was detected after exposing the pristine G/Ni(111) at low temperature and after dosing CO at room temperature on the G/Ni(111) in presence of vacancies, no trace of adsorption was detected for $G/Cu_{poly}$ under any condition, not even in presence of vacancies at low temperatures.

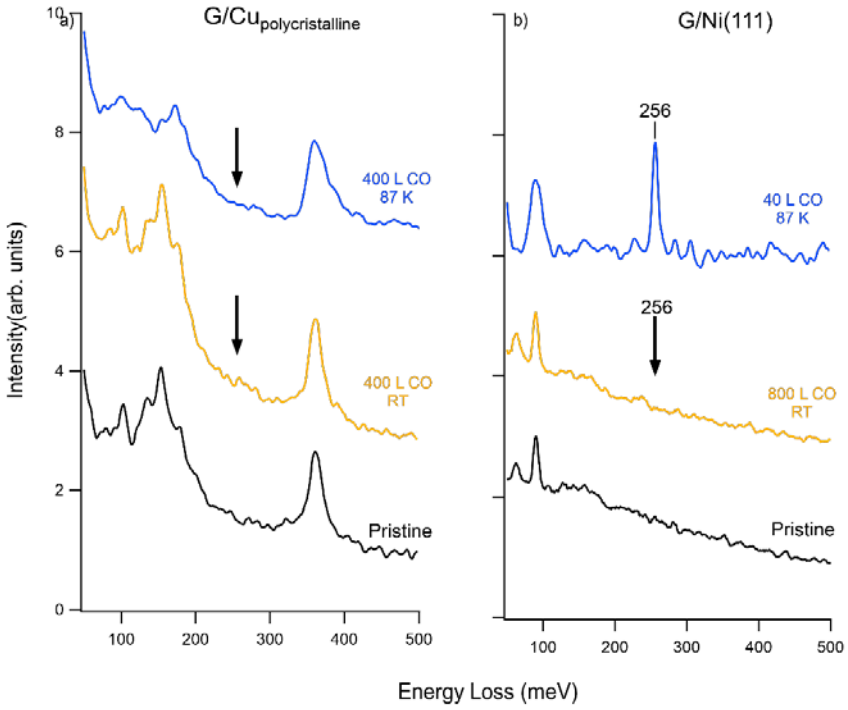


Figure 4.10 – Comparison of HREELS spectra recorded for a graphene layer grown on polycrystalline Cu (panel a) or single crystal Ni(111) (panel b). The spectra are taken at the following conditions: (black) pristine samples, (yellow) dose of CO at room temperature, (blue) CO dosed at 87 K. The arrow indicates the position where the CO stretch mode is expected.

The different chemical reactivity of the supported graphene layer is directly caused by the different level of interaction with the substrate: only the highly interacting nickel affects enough

the density of states of the graphene layer and makes it reactive towards CO. The less interacting copper substrate shows no reactivity at all, even at liquid nitrogen temperature. Moreover, since on a polycrystalline sample the different grains can expose different surface terminations we can conclude that neither grain edges nor surface terminations different from the (111) modify the reactivity of the graphene layer enough to support stable CO adsorption even at 87 K.

## 4.4 Conclusions

The outcome of our combined vibrational spectroscopy and STM experiments allows thus to conclude that:

a) CO chemisorbs molecularly on G/Ni(111) at 87 K with a nearly unitary sticking probability.
b) The adlayer is stable up to 125 K and desorbs gradually above this T.
c) CO adsorption takes place at pristine graphene areas, not just at defects.
d) The chemical reactivity of G/Ni(111) depends on the relative position of the G layer respect to the undelying substrate and the top fcc configuration is the most reactive one
e) The amount of non graphenic carbon and of rotated or partially detached graphene patches negatively impacts the chemical reactivity

Assuming a pre factor for desorption of $10^{13}$ Hz [87–89] and using an Arrhenius like dependence for the desorption rate (see appendix A), we estimate a desorption energy of ~0.35 eV/molecule at 1/3 ML coverage (in ML of Ni(111)) and of ~0.58 eV/molecule in the low coverage limit. Since no adsorption barrier is present, this estimate equals the adsorption energy. The higher value in the low coverage limit (evidenced by the residual coverage after flashing at and above 150 K) can be due either to adsorption at defect sites [90] or to repulsive interactions between admolecules at regular sites [91]. Whatever the reason, the value of 0.35 eV/molecule is much higher than the one predicted for free standing graphene [5]. This allows to obtain a significant equilibrium coverage under realistic, catalytic conditions. Using a Langmuir isotherm, an equilibrium coverage of ~0.1 ML is attained at RT under a CO partial pressure of only 10 mbar[1].

Occurrence of CO chemisorption, albeit weak, is an unexpected results which can only be accounted for by the presence of a reactive substrate such as Ni(111) below the G layer. Photoe mission measurements [92,93] show indeed that at the K point a substantial flattening of the $\pi$ band occurs. Such strong perturbation of the ideal electronic structure of G is responsible for the opening of a gap [92] and for the partial disruption of the Dirac cone. Band bending implies clearly a high DOS below the Fermi energy. This feature mimics the d band intensity of transition metals closes to the Fermi level and is suggested therefore to account for the enhanced reactivity of Ni supported graphene with respect to a free standing G film, although it

[1] As a result of the compensation effect in the Arrhenius analysis, the assumption of a 100 times lower (higher) value of the prefactor affects the estimated adsorption energy by 0.05 eV but does not affect the order of magnitude of the attainable equilibrium coverage at a given pressure and temperature.

is not yet clear whether the observed increase in the adsorption energy can be accounted for by intrinsic *n* doping alone [9].

In conclusion, we have demonstrated that Ni supported graphene (and possibly graphene grown on other highly interacting substrates) enables CO chemisorption with relatively high adsorption energies, paving the way to its use in catalytic applications. The adsorption energy is thereby high enough to permit reaching an equilibrium coverage significantly higher than for un supported graphene, but low enough to ensure that the removal of CO from graphene will not be the rate limiting step [94].

# 5 N Doping of G/Ni(111) an its reactivity with CO

## 5.1 Introduction

After some understanding of the properties of pristine G has been reached, [95,96] attention has focused on the possibility to tailor its properties, for example by introducing dopants such as N and B atoms [97–99], which either donate or withdraw free electrons. The presence of heteroatoms in the perfect hexagonal structure of G causes structural and electronic distortions, leading to changes in the electronic state, charge transport, bandgap, spin density, optical characteristics, thermal stability or magnetic properties of pristine G. The knowledge of the changes induced by the introduction of heteroatoms in G layer is an important prerequisite to design new G based materials for novel applications.

An enhanced chemical activity was predicted by first principle theoretical calculations, e.g., for B doped graphene interacting with $NO_2$ and $NH_3$ [43]. Theorists proposed moreover that, while graphene vacancies cannot selectively sense CO in air, N doped graphene could be an excellent candidate for this purpose [100] since pyridinic like N doped sites can adsorb this molecule but are inert towards $N_2$ and $O_2$. Adsorption should be accompanied by a large charge transfer, which would in turn provide a detectable signal for CO sensing. The calculated heat of adsorption for CO on N doped graphene is 3.43 eV, to be compared to the value of 0.17 eV for the pristine layer. Even higher adsorption energies have been predicted for Al doped graphene [11].

The increased reactivity induced by doping of the G film has been proved experimentally, e.g., for $NH_3$ in concentrations of 100 ppm at RT on P doped graphene [101]. More recently the key role of pyridinic N in the Oxygen Reduction Reaction has been demonstrated, too [57].

Depending on the doping site, different shifts of the graphene bands are expected: while pyridinic N would cause an upshift of the bottom of the $\pi$ band, incorporation of N into the graphene lattice in substitutional sites (otherwise called graphitic N) would cause a shift in the opposite direction [16].

Here, we present an experimental study performed under controlled ultra high vacuum (UHV) conditions aimed at clarifying the effect of doping with N atoms on the reactivity towards CO adsorption of a G/Ni(111) layer. In addition to the chemisorption channel open also for pristine G/Ni(111) [17], the presence of N atom dopants causes the appearance of a novel chemisorbed CO species. The latter is characterized by a CO stretch frequency in the range expected for bidentate CO and by an adsorption energy close to ~0.85 eV/molecule at low coverage, i.e. significantly higher than for CO at pristine G/Ni(111) sites.

## 5.2 Experimental

The Ni(111) crystal was cleaned by repeated sputtering (with 3 keV $Ne^+$ ions) and annealing (1283 K) cycles. Graphene was grown in situ by the thermal dehydrogenation of ethene catalysed by the Ni surface at $T_g$=823 K, (P=5 10 $^6$ mbar 660 seconds), as described in more detail

[17,18,20]. This procedure resulted in single layer graphene domains up to a few tens of nm in size, as verified by LT STM [17]. According to a recent XPS study, this protocol enables to obtain a high fraction of top fcc graphene, which is the most reactive configuration for CO adsorption [18]. N doping was introduced by bombarding the pristine G/Ni(111) single layer [102] with $N_2^+$ ions with 110 eV energy (the lowest energy attainable with our ion gun) at normal incidence and RT. The ion dose was varied to control the doping level and it is set to ~$10^{15}$ ions/$cm^2$ in the present experiment. The layer was eventually annealed to 550 K to reduce the amount of implanted nitrogen. Higher temperature annealing was not performed to avoid the possible depletion of pyridinic N, as reported for G/Ir(111) [103]. CO was dosed by backfilling the chamber with a doser close to the sample [17,18,20].

The cleanliness of the Ni(111) substrate, the chemical nature of the graphene layer as well as the doping level were checked by XPS. Spectra were recorded using the Al $K_\alpha$ photon and the binding energy ($E_B$) was calibrated on the metallic Ni $2p_{3/2}$ photoemission peak, which is located at $E_B$=852.6 eV in absence of dissolved carbon [72]. In order to obtain quantitative information on the chemical composition, the spectra were fitted with an asymmetric Doniach Sunjic line shape after subtracting a Shirley background. An asymmetry parameter α=0.08, intermediate between the one (0.1) typical of G/Ni(111) and the one found for G/Ni(111) after Au intercalation (0.061), was used [104]. Up to four components were necessary to reproduce the C1s line shape, while three components were employed to fit the N 1s region.

CO adsorption was monitored by HREELS. Spectra were recorded *in specular,* at 62° incidence with respect to the surface normal and at primary electron energy E=5 eV to enhance the sensitivity to adsorbed species. Thanks to the high dynamical dipole moment, CO can be detected already at very low surface coverage. The spectra are normalized to the inelastic background around 300 meV.

## 5.3 Results and discussion

Figure 5.1 shows the X ray photoemission spectra of the C1s and N 1s regions recorded after growth of the G/Ni(111) layer (bottom spectra) and after doping it by $N_2^+$ ion sputtering (top spectra). $N_2^+$ ion bombardment and annealing to 550 K causes a significant modification of the C 1s line with respect to the pristine graphene case: it broadens significantly, and a shoulder develops at lower $E_B$. While the pristine G/Ni(111) can be described by a single C1s component centred at 284.7 eV, the N doped layer clearly consists of different C species. Its line shape can be properly described only including additional components due to detached G (284.1 eV, ~28 %), to $Ni_2C$ (283.4 eV, ~13 %) and to C bonded to N (285.5 eV, ~16 %). The ratio between the number of C atoms bonded to N and the number of C atoms *in graphene* is 18 %. The N1s spectrum demonstrates that N atoms are present in different configurations, in agreement with literature [102,105].

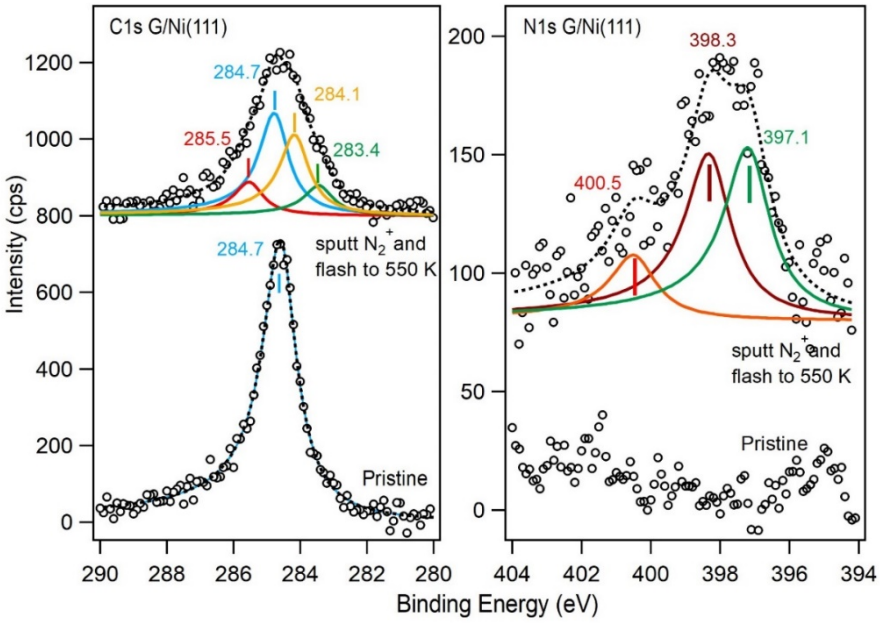


Figure 5.1 C 1s (left) and N 1s (right) photoemission spectra recorded: (bottom spectra) after growth of the graphene film; (top spectra) after N-doping by $N_2^+$ ion bombardment (ion dose of ~$10^{15}$ ions/cm$^2$) and subsequent annealing to 550 K

Indeed, as summarized in table I, components with $E_B$=397.1 eV, 398.3 eV, 400.5 eV are identified and assigned by comparison with literature to Ni nitride, to pyridinic N and to pyrrolic N. No intensity is found at $E_B \geq 400.6$ eV, i.e. in the energy range suitable for graphitic N. We deduce therefore that this nitrogen species is absent or present in negligible concentration in our sample. While the assignment of the two features at lower $E_B$ is straightforward, the presence of pyrrolic N in higher concentration than graphitic N is at variance with the results of ref. [102], which reports a component at 400.7 eV ascribing it to graphitic N only.

| | **NG/Ni(111)** [105] | **NG/Ni(111)** [102] | **NG/Ni(111)** [16] | **HOPG** [57] | **NG (from GO)** [106] | **NG/Ni film** [5] | **Present study** |
|---|---|---|---|---|---|---|---|
| **Pyridinic** | 398.2-399.3 | 398.7 | 399 | 398.5 | 398.5 | 398.3 | 398.3 |
| **Pyrrolic** | 400.1-400.5 | ---- | ---- | 400.1 | 400.1 | 400.5 | 400.5 |
| **Graphitic** | ---- | 400.7 | 400.6 | 401.0 | 401.5 | ---- | ---- |
| **$Ni_2C$** | ---- | 397.3 | ---- | ---- | ---- | ---- | 397.1 |

Table 5.1 - N1s binding energy (in eV) of the different N species according to recent literature: for N doped (NG) G grown on Ni(111), for different kinds of HOPG, for NG obtained from graphene oxide (GO) and for NG on a Ni film and for the present results.

| **Protocol** | **Doping** | **$N_{nitr}/N_{tot}$** | **$N_{pyr}/N_{tot}$** | **$N_{pyrr}/N_{tot}$** | **$N_g/N_{tot}$** |
|---|---|---|---|---|---|
| $N_2^+$ ion bombardment & flash to 550 K | 11 % | 43 % | 41 % | 16 % | ~ 0 % |

Table 5.2 – Doping level (defined as: $(N_{pyr}+N_g+N_{pyrr})/(C_g+N_{pyr}+N_g+N_{pyrr})$) and fraction of the different kinds (substitutional: $N_g$, pyridinic: $N_{pyr}$; pyrrolic: $N_{pyrr}$ and nitride: $N_{nitr}$) of N atoms as determined by XPS. It is apparent that 43 % of the total amount of N is in nitride form and is thus not part of the G layer. We can estimate an uncertainty of ~ 2% on the concentration values reported in the table.

Eventually, the so obtained N doped graphene layers were exposed to 40 L CO at RT and at 87 K. The corresponding HREEL spectra are shown in Figure 5.2, together with the spectrum recorded after exposing pristine G/Ni(111) to the same CO dose. No traces of adsorbed CO are observed after exposing the N doped G/Ni(111) layer at RT, indicating that ion bombardment with 110 eV nitrogen ions does not open an adsorption channel at RT. This result is at variance with what we observed for CO adsorption at a $Ne^+$ ions sputtered G/Ni(111) [20]. As I shall show in the next chapter, in that case, CO intercalation and chemisorption on the Ni(111) substrate occurs, yielding an intense loss at 237 meV and a weaker one at 253 meV, both stable at least up to 350 K [20]. The occurrence of intercalation close to the N site can thus be excluded and the absence of CO adsorption at RT also rules out the presence of bare Ni patches in the present experiment [84,108,109].

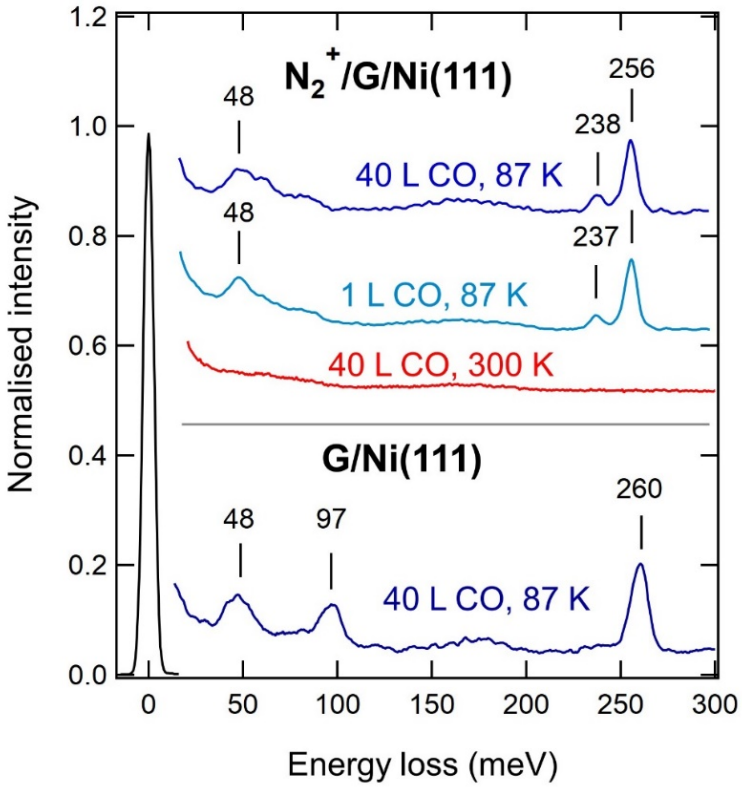


Figure 5.2 HREEL spectra showing CO adsorption at pristine G/Ni(111) (from ref. [17], bottom spectrum) and at N-doped G/Ni(111) for different T and CO dose, as discussed in the text. The data are normalized to the inelastic background around 300 meV.

Upon exposure of the N doped G/Ni(111) system at 87 K to 1 L of CO, a doublet at 237 and 256 meV appears in the HREEL spectrum. Both losses can be ascribed to the internal stretch mode of CO molecules and thus indicate CO adsorption at two non equivalent sites. Increasing the CO exposure to 40 L causes a negligible increase of the losses, indicating that a coverage close to saturation is reached already at the lowest dose. CO adsorption is thus a non activated process with a high sticking probability. The intensity of the CO stretch vibration at 256 meV is only 15 % lower than the corresponding one measured upon 40 L of CO exposure onto pristine

G/Ni(111) (bottom spectrum in Figure 5.2), but it is red shifted in energy by ~4 meV. It is therefore compatible with CO molecules in a mono dentate configuration, i.e. in on top position [110]. On the other hand, the weaker loss at ~238 meV, present only for the doped sample, is compatible with the internal stretch mode of doubly coordinated (i.e. bridge bonded) [110] CO. The additional broader losses around 48 meV and 97 meV are assigned to the CO substrate stretch vibration and to water contamination, respectively.

In order to estimate the adsorption energy of the observed CO moieties, the thermal evolution of the HREEL spectra was recorded while the sample warms up (Figure 5.3A). The heating rate is not constant because, since the use of a heater is not compatible with the simultaneous recording of sequential HREEL spectra, the sample was annealed by switching off the cooling system. The 256 meV species starts to decrease immediately upon annealing, while the one at lower energy is stable up to 160 K and disappears below RT. Since both CO intercalated under G/Ni [20,108] and CO adsorbed on bare Ni(111) [84,108] desorb well above RT, we conclude that the observed losses correspond to CO admolecules at graphene sites.

| | **E($\Theta$=0) (eV/molecule)** | **E($\Theta = \Theta_i$) (eV/molecule)** | **$\Theta_i$ (ML)** |
|---|---|---|---|
| **Monodentate CO (256 meV)** | 0.54 | 0.34 | 0.28 |
| **Bidentate CO (238 meV)** | 0.85 | 0.50 | 0.10 |

Table 5.3 – Desorption energy for the single and double coordinated CO moiety, as obtained by fitting the temperature dependence of the corresponding CO stretch intensity (see text).

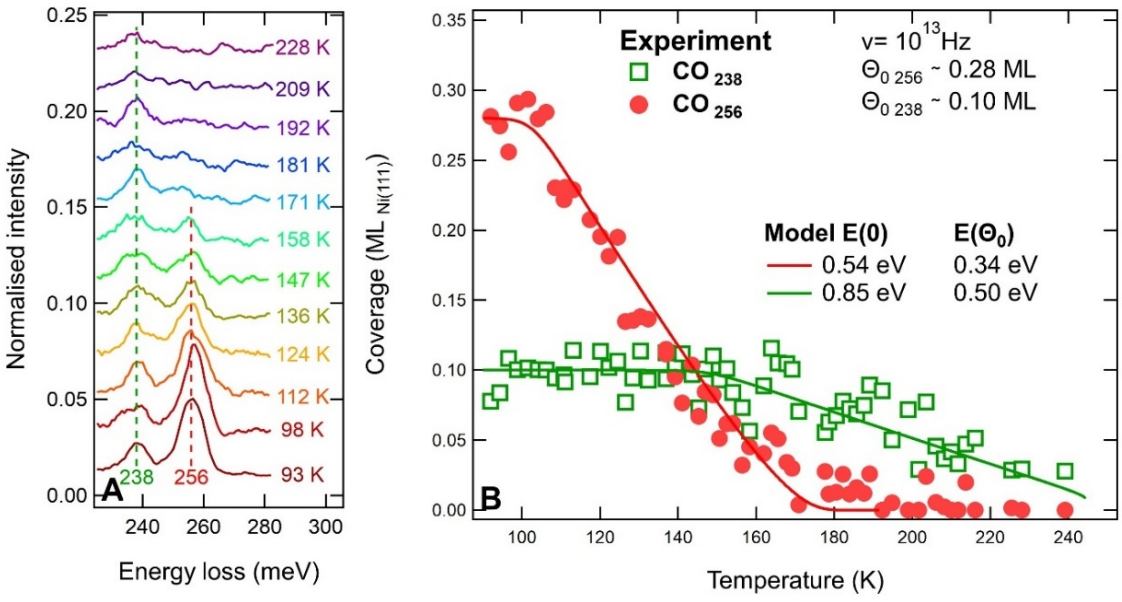


Figure 5.3 A: HREEL spectra recorded sequentially on the N-doped G/Ni(111) layer exposed to 40 L of CO at T= 87 K while slowly warming up after switching off the cooling system. The temperature readings correspond to the average of T at the beginning and at the end of each spectrum. The $N_2^+$ dose is ~$10^{15}$ ions/cm$^2$, yielding an N doping of ~11 % as estimated by XPS. B: Coverage of the two CO moieties (derived from the area of the CO-stretch peaks in HREELS) vs. crystal temperature.

The frequency of the mono dentate species (254 256 meV) is close to the one observed on pristine G/Ni(111) (260 meV [17]), so we assign it to CO adsorbed at bare graphene sites. The slight redshift with respect to the pristine G case is due either to a larger charge transfer, and thus a possibly slightly stronger chemisorption, or to a lower local coverage or to a combina tion of both effects. By comparing the intensity (normalized to the background) of the 256 meV peak with the one found for pristine G/Ni(111), we can roughly estimate the coverage of mono dentate CO to be ~85 % of the one reported for the CO saturated pristine sample. Since in that case a local coverage of 0.33 ML (in ML of Ni(111)) was estimated from analysis of STM images, here we can assume a maximum coverage of~0.28 ML for the 256 meV species.

We assign the feature at 238 meV to CO adsorbed close to doped sites. From the intensity ratio between the two CO stretch peaks, which is initially between ¼ (Figure 5.2) and 1/3 (Figure 5.3), we deduce the coverage of the bidentate moiety to be ~0.10 ML, under the assumption that the dynamical dipole moments of the two species are comparable. The temperature dependence of the peak intensity (and hence of the coverage) of the two CO species is reported in Figure 5.3B together with simulations performed to estimate the CO desorption energy. Assuming an initial coverage of 0.10 ML and 0.28 ML for bi dentate and mono dentate species, respectively, and a pre factor for desorption $\upsilon_{des} = 10^{13}$ Hz, the desorption energy could be estimated applying the following rate equation:

$$\frac{d\Theta}{dt} = -\upsilon_{des}\Theta\, e^{-\frac{E(\Theta)}{kT(t)}}$$

in which T(t) is the time dependence of the sample temperature obtained by allowing the sample to warm up by switching off the cooling system, k is the Boltzmann constant and E(Θ) is the coverage dependent desorption energy. We mention that fitting the data with a coverage independent heat of adsorption was not possible. Therefore, in absence of calorimetric data for this system, we assumed a linear dependence of E with coverage to account for the presence of repulsive interactions between the adsorbates [91]:

$$E(\Theta) = E(0) - a\Theta$$

Numeric integration of the related finite difference equation:

$$\Theta(t+\Delta t) = \Theta\,(t) - \upsilon_{des}\Theta(t)\, e^{-\frac{E(\Theta)}{kT(t)}}\Delta t$$

has been used to obtain the curves reported in Figure 5.3B (continuous lines) with the fitting parameters shown in table III. We observe that the temperature dependence of the 256 meV species is described reasonably well by the same values of the heat of adsorption obtained for pristine G/Ni(111). We thus conclude that the reason for the slightly lower frequency is most likely the lower local coverage.

On the contrary, the increase of the heat of adsorption for the bidentate CO molecules in proximity of a doped site is quite relevant. In the low coverage limit, it implies a lifetime of about 180 s at RT, to be compared with 0.2 ms for non doped graphene. Even if such values can be affected by systematic errors due to the choice of the pre factor for desorption, the substantial stabilization of adsorbed CO induced by N doping is evident.

## 5.4 Conclusions

The present study does not allow to determine which nitrogen species among those detected in the XPS spectrum of Figure 5.1 are responsible for the stabilization of bidentate CO. However, nitride is ruled out since it is buried below graphene, so it is not part of the layer and it is expected to be a spectator. This conclusion is supported by the fact that the estimated coverage of bidentate CO (~0.10 ML) is close to the amount of N (11 %) included in the graphene layer (pyridinic and pyrrolic N). However, we cannot exclude that more than one CO molecule is stabilized by each dopant atom, implying then that only one N species may be active. Although additional experiments performed with different ratios of pyrrolic, pyridinic and, possibly, graphitic N species would be required to clarify this point, the identification of the active site with pyridinic and/or pyrrolic N is already evident. The possibility that the newly observed CO species is adsorbed at nickel carbide sites is ruled out because, in presence of $Ni_2C$, adsorbed CO should desorb between 290 and 320 K [108]. Finally, to the best of our knowledge, there are no surface science studies of adsorption of CO on nickel nitride but, for the chemically similar reduced $Ni_2P$, CO desorbs above RT [111], at variance with the observations of the present experiment. This suggests that also nickel nitride is not responsible for the observed CO.

# 6 Vacancies at G/Ni(111) and at G/$Cu_{poly}$ and their reactivity with CO

## 6.1 Introduction

Graphene (G), is known to be chemically "inert" in its pristine configuration, i.e. in absence of defects [112], although it can induce complexation reactions by its delocalized π electron sys tem [113]. Both intercalation and reaction of CO below G have been reported previously[58,60,114]. As reported in the previous chapters, theoretical calculations confirm low adsorption energies for simple molecules on pristine, free standing graphene [40] (8 meV 14 meV for CO, depending on adsorption site), but predict strong bonds at graphene vacancies and at substitutional defects (up to ~1.7 eV and ~6.3 eV respectively) [43,44,115]. Defects affect also the electronic properties of the G layer: a local modification of the density of states has been indeed reported by STS following ion irradiation [116], and opening of the gap occurs for patterned adsorption [52,117] (with a possible influence on the electric response to adsorbates and, consequently, on the sensor properties [1,118]).

The possibility to realize graphene based devices for sensing CO in concentration of 1 to 100 ppm[1,118] has been recently reported. Such devices are based on the fact that CO acts as an electron donor and causes a reproducible increase in the resistance of the graphene film at taining its final value on a time scale of several minutes. The nature of the CO adsorption site remained, however, unexplored. The high exposure required to observe a CO related signal indicates a low net sticking probability. On the other hand, the need to operate the sensor at 300°C [119] or to re generate it by annealing to 150°C [1] suggests that the active sites have a relatively high adsorption energy, i.e. that adsorption occurs at defects. Indeed, we have recently demonstrated that pristine G layers are reactive towards CO only when supported on a strongly interacting substrate such as Ni(111). Also then, CO adsorbs reversibly at room temperature [17].

## 6.2 Experimental

To clarify this issue, we investigated experimentally CO adsorption at defected graphene single layers under Ultra High Vacuum (UHV) conditions and compared their reactivity when grown or deposited on two different substrates: Ni(111) (G/Ni in the following) and polycrystalline Cu (G/Cu). The chemical properties of the films were investigated by X Ray Photoelectron Spectroscopy (XPS) and by High Resolution Electron Energy Loss Spectroscopy (HREELS). For the G/Ni(111) sample also a morphological analysis by STM was performed by repeating the preparation in a dedicated UHV apparatus.

For all samples, vacancies were created by 150 eV $Ne^+$ ion bombardment at normal incidence for the spectroscopy experiments. On the contrary, ion bombardment was applied ~55° off normal incidence in the STM experiments for G/Ni(111) due to geometrical constraints of the

corresponding apparatus. According to previous experimental [120,121] and theoretical [122] studies, $Ne^+$ irradiation under very similar conditions produces single and double vacancies (i.e. situations in which only one C atom or two adjacent C atoms of the G lattice are removed, respectively) in ~5:2 ratio.

## 6.3 Results and discussion

While the surface presents extended corrugated protrusions (in a quite disordered arrangement), the elongated shape of the "scars" suggests that, most likely, they derive from the healing of short array of single vacancies such as those apparent in Figure 6.2C.)

Figure 6.1 compares HREEL spectra recorded for different samples before and after exposure to 400 L CO at room temperature (RT). Given the density of C atoms in G (~3.85 $10^{15}$ at oms/$cm^2$) in order to produce a low density of isolated vacancies the sputtering dose is $\chi_{Ne+}$=3.2 $10^{14}$ $Ne^+/cm^2$ for both the G/Ni and the G/Cu samples.

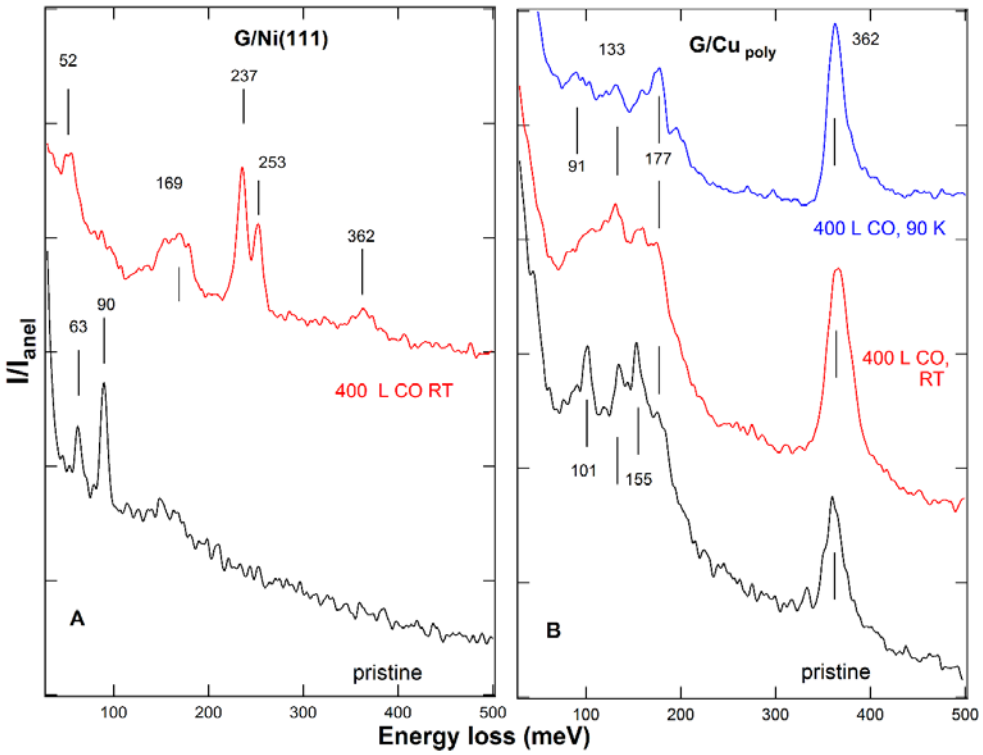


Figure 6.1 – HREEL spectra recorded in-specular and corresponding to experiments performed for: (A) G on Ni(111), (B) G on polycrystalline Cu and. In each panel, the spectra are normalized to the inelastic background $I_{anel}$ between 450 and 500 meV loss energy and are vertically shifted for sake of clarity.

Starting from the G/Ni(111) (Figure 6.1A), we can see that before ion bombardment weak losses at 63 meV and 90 meV are present corresponding to defects of graphene[80] and to the z polarized phonon[79], respectively. No vibrational signature of CO adsorption has been ob served on the pristine layer exposed at RT under UHV conditions [17], while additional peaks show up at 52 meV, 237 meV and 253 meV for the ion bombarded graphene layer (indicated as G*). They correspond to the molecule – surface and to the internal C O stretch mode for

bridge and atop configurations, respectively[84]. Their presence proves that CO adsorption has occurred. A further broad peak is visible at about 169 meV, a frequency close to the one of the D band in Raman spectra[123] and which is considered a marker of surface disorder. It is present also for defected samples not exposed to CO (not shown[2]) so that we assign it to distorted G configurations. The loss at 362 meV corresponds to the C H stretch resulting from water dissociation [124].

For G/$Cu_{poly}$ (Figure 6.1B), we observe that in the initial spectrum (black) losses are already present at 101 meV, 133 meV, 155 meV, 177 meV and 362 meV. Since the as delivered sample was introduced into vacuum and treated only by a mild annealing to 390 K, these modes correspond to residual traces of contaminants (in particular the losses at 177 meV and at 362 meV correspond to the presence of CH groups[124]) and to distorted configurations of the graphene layer (see SM for details). Contrary to the case of G*/Ni(111), no additional losses are detected following the exposure to 400 L CO (neither at RT nor at 90 K) indicating that the G* layer on Cu is inert.

The energy of the losses at 52 meV, 237 meV, and 253 meV observed for G*/Ni(111) are close to those reported for CO/Ni(111)[84] at high coverage (50 meV, 237 meV and 254 meV, respectively). The CO stretch frequency is notably lower than the one reported for CO chemisorbed on pristine G/Ni at 90 K[17,125]. This leads to the conclusion that CO reaches the Ni substrate through the vacancies. Since intercalation below G/Pt(111) causes a *red shift* of the CO stretch frequency of ~2 meV[60], we conclude that a high local coverage of CO is reached for G*/Ni(111) when exposed to CO.

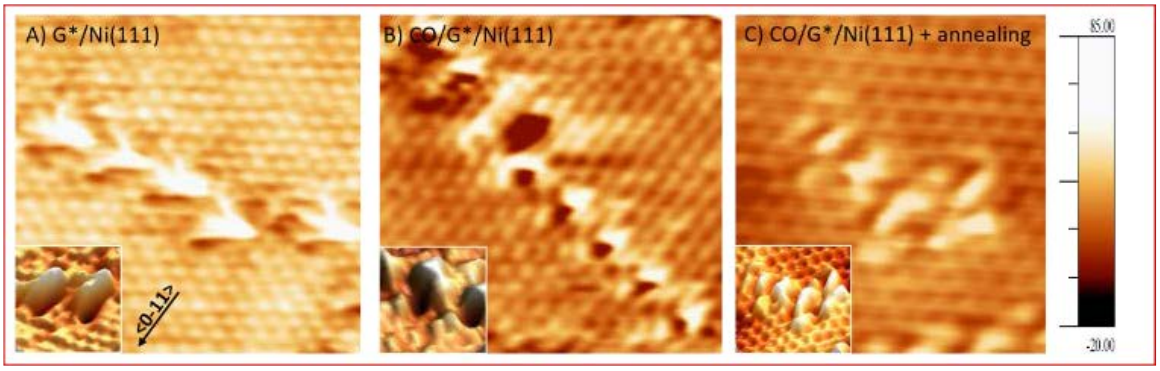


Figure 6.2 – STM image of (A) G*/Ni(111) without CO exposure (V=0.05 V, I=0.6 nA), (B) G*/Ni(111) after 400 L CO exposure (V=-0.02 V, 0.7 nA) and (C) G*/Ni(111) with 400 L CO after annealing to 400 K (V=-0.15 V, 0.7 nA). For all images, size: 35x35 $nm^2$; the same scale, reported on the right side, was employed for the apparent height (in pm).

[2]In the experiments reported in Figure 6.1, no HREEL spectra of the defected G* layer immediately after sputtering and prior to CO exposure have been recorded. This was done to avoid unwanted CO contamination from the residual vacuum during the time necessary to record the HREEL spectrum.

The corresponding STM image for G*/Ni(111) (see Figure 6.2A) shows localized defects. They are compatible in size with the production of mostly monoatomic vacancies following ion irradiation. Since each hole has a protrusion on its side[126], it is reasonable that the displaced C atom has ended up above the G* layer close to the defect.

Even if it is not possible to resolve the presence of CO ad molecules close to or into the gra phene vacancies, inspection of a typical image recorded before and after CO dose (panel A and B respectively) shows a change in the apparent shape and dimensions of the defects, indicating that the system is modified by adsorption.

The data reported clearly indicate that CO adsorption occurs only for G*/Ni(111), i.e. in presence of a reactive substrate. Adsorption was investigated as a function of $\chi_{Ne+}$ (sputtering dose) by XPS and HREELS (see Figure 6.3).

XPS spectra were recorded after sputtering and prior to CO exposure. Vice versa, HREEL spectra were recorded after exposing the samples to 400 L CO at RT.

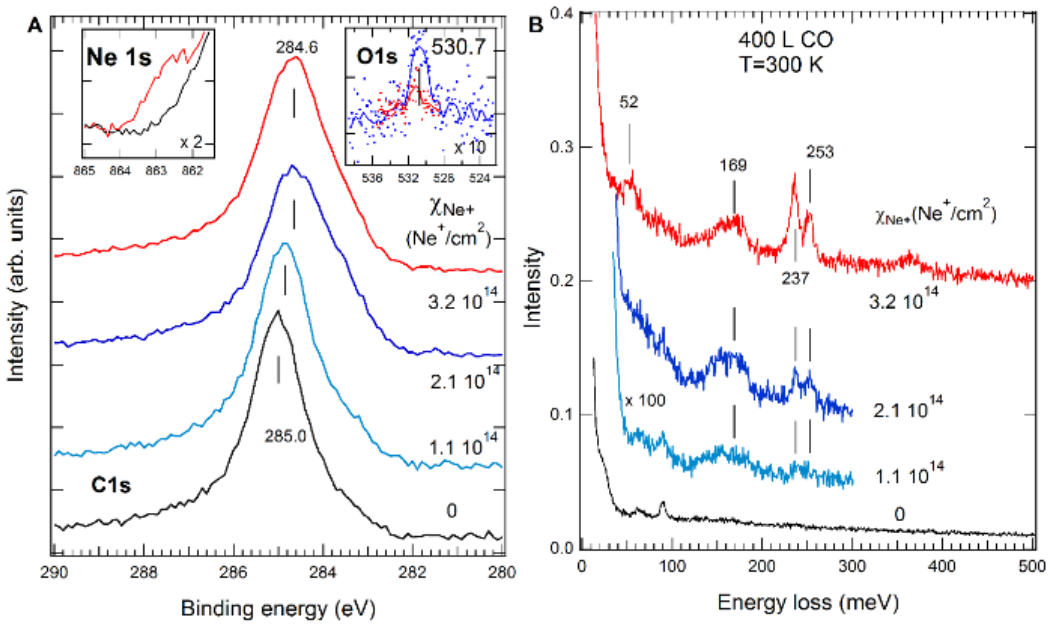


Figure 6.3 – A: XPS spectra of the C 1s line following ion bombardment and prior to CO exposure. Inspection of the Ne 1s region after the highest sputtering dose proves intercalation[127] (see left inset; black/red spectrum corresponds to pristine/defected G layer). The inset on the right shows the O 1s signal after 400 L CO following $\chi_{Ne+}$ =2.1 10 $^{14}$ $Ne^+/cm^2$ (blue) and after annealing to 450 K (red). B: HREEL spectra recorded in-specular and normalized to the elastic intensity, after exposing pristine and ion bombarded G/Ni(111) to 400 L CO at RT.

After the mildest sputtering dose (second spectrum from the bottom), the C1s peak in XPS shifts to lower binding energy while a broad energy loss develops around 169 meV in HREELS. This change is due to the detachment of G from the Ni(111) substrate when vacancies form and when Ne atoms intercalate. Indeed, $E_b$ (C 1s) downshifts towards 284.3 eV, a value close to the one reported in the literature for graphene on Ni(111) "decoupled" by CO intercalation at high pressure [108]. Moreover, at the largest $Ne^+$ dose (3.2 $10^{14}$ $Ne^+/cm^2$), a Ne 1s signal is visible at

863 eV as a shoulder of the Ni $2p^{3/2}$ peak, corresponding to a concentration of ~4 % with respect to C. Given the surface density of Ni(111), for this ion dose each C atom has a probability of ~9% of being hit by one $Ne^+$ ion during irradiation. Assuming the defect creation probability given in ref.[122], we can thus estimate a population of single/double vacancies of ~4.5/1.5 %, respectively.

CO binds at the defected G*/Ni(111) surface as witnessed by the additional relevant energy losses. The relative intensity of the CO stretch mode for molecules at bridge and on top sites depends on $\chi_{Ne+}$ : initially the two sites are equally populated while with increasing sputtering dose the relative population observed for bare Ni(111) is approached.

The low intensity of the CO stretch modes is due to the low concentration of vacancies in the G* layer and to the screening of the modes by the latter. Comparing the measured intensity of $\nu$(CO) with the one reported for a coverage $\Theta_{CO}$=0.5 ML on Ni(111)[84], we estimate $\Theta_{CO}$~0.03 $ML_{Ni(111)}$ (1 $ML_{Ni(111)}$ =1.86 $10^{15}$ atoms/$cm^2$ ) for $\chi_{Ne+}$ = 2.1 $10^{14}$ $Ne^+$. In accord with this, XPS inspection shows only a very weak O1s intensity around 531 eV (see inset of Figure 6.3A), while the C1s signal of CO expected around 286 eV[108] is too small to emerge from the much larger G related component at 285 eV[67]. From comparison of the O 1s and C 1s intensities, we estimate a O/C ratio of ~2 %, i.e. $\Theta_{CO}$~0.04 $ML_{Ni(111)}$, compatible with the coverage estimated by HREELS."

Although both estimates of defect density and of CO coverage may be affected by systematic errors, both the HREELS and the XPS analysis agree that the number of defects introduced by ion bombardment in the G layer is only a few % of a ML. The distortion of the layer around the vacancies affects several neighbouring sites, causing a detectable shift of the C1s peak. This is coherent with the STM information, which shows a modified density of states over an area significantly larger than the one corresponding to the single vacancy.

Figure 6.4A shows the effect of annealing the CO/G*/Ni(111) sample. After flashing the sample above 400 K, all the CO related losses disappear, while the broad energy loss feature around 169 meV survives, confirming that the latter loss is due to the distortion of C C bonds in G*. The C 1s line remains unchanged up to T=500 K (Figure 6.3B) and it up shifts towards the value of pristine G/Ni(111) when heating to 700 K. At the same T, the vibrational loss at 169 meV decreases in intensity. These observations indicate that the G sheet attaches again to the Ni substrate, although the initial state is not fully recovered: a shoulder at $E_b$=283.4 eV is indeed present in the C1s region and small losses at 90 and 62 meV are also visible. The C 1s component at 283.4 eV corresponds to nickel carbide[108] while the vibration at 62 meV is compatible with its vertical stretch (reported at 50 meV for C/Ni(100)[128] and at 59 meV for C/Ni(111) in presence of Na[80]).

For subsequent adsorption/annealing cycles (see Figure 6.4C), a decreasing amount of CO adsorbs in the second and third uptake. In particular, on top sites are de activated more rapidly than bridge sites.

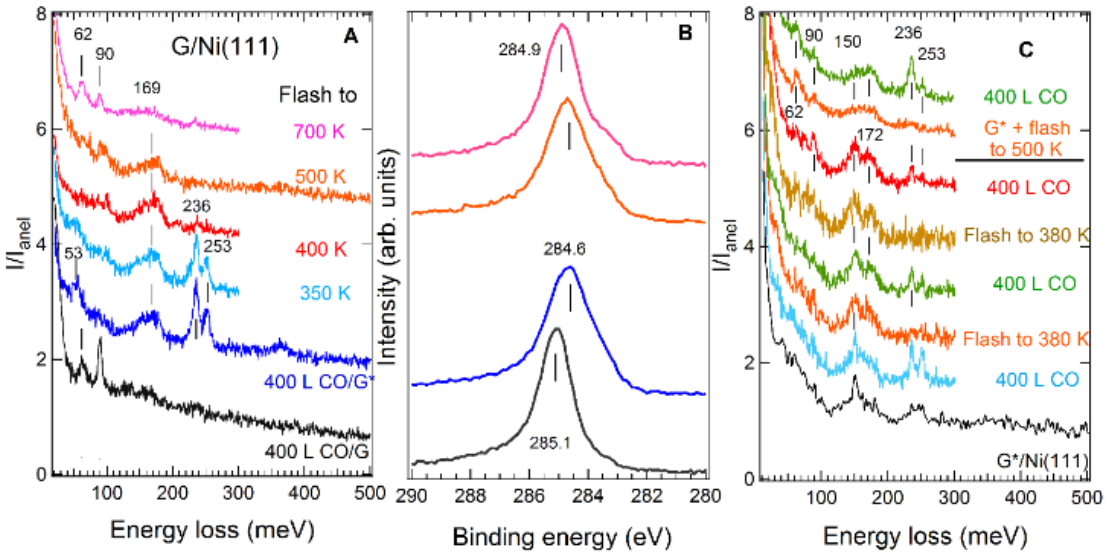


Figure 6.4 – (A) HREEL spectra recorded in-specular after annealing the CO covered G* layer to different temperatures. (B) XPS spectra for pristine G/Ni(111) (black), CO covered G*/Ni following 3.2 $10^{14}$ $Ne^+$ irradiation (blue) and after annealing to 500 K (orange) and to 700 K (pink). (C) HREEL spectra of: (black trace) G*/Ni(111) immediately after ion bombardment ($\chi_{Ne+}$=2.8 $10^{14}$ $Ne^+/cm^2$). Notice that the broad loss around 150-172 meV is present also before dosing CO; (Light blue to red traces) the same layer after subsequent cycles consisting of an exposure to 400 L at RT followed by annealing to 380 K; (Top orange and green traces) G*/Ni(111) obtained after annealing freshly sputtered G/Ni(111) ($\chi_{Ne+}$=3.2 $10^{14}$ $Ne^+/cm^2$) to 500 K without CO exposure and after exposing to 400 L CO at RT. The different ratio of top and bridge CO depends on $\chi_{Ne+}$.

If we anneal the sputtered surface to 500 K *without pre adsorbing CO,* the vacancies remain reactive since thermal healing of vacancies occur at a definitely higher temperature (920 K according to Jacobson et al.[129]).

STM images of the annealed CO/G*/Ni(111) system (see Figure 6.2C) confirm a significant modification of the surface morphology. Indeed, after annealing, the vacancies induced by sputtering are no longer detected, while the surface presents extended corrugated protrusions (in a quite disordered arrangement), the elongated shape of the “scars” suggests that, most likely, they derive from the healing of short array of single vacancies such as those apparent in Figure 6.2A."

CO dissociation with reactive oxygen removal and healing of the original vacancy by the residual C atom was predicted by Wang and Pantelides for CO + NO reaction[44] and by Liu and Lee for CO + CO[115] on free standing graphene. If this were the relevant mechanism, then it should be active also for G* on $Cu_{poly}$, contrary to our experimental evidence. The theoretical calculations performed for free standing graphene are thus inadequate to describe the behaviour of supported graphene even for weakly interacting substrate as Cu. Indeed it has been recently demonstrated by L. Ferrighi et al. [130] that the dangling bonds of the carbon atoms formed upon vacancy creation get immediately saturated towads the substrate both for G/Cu(111) and for G/Pt(111).

The graphene layers become slightly corrugated and the binding with the substrate is strong enough that one atom is partially pulled out of the surface.

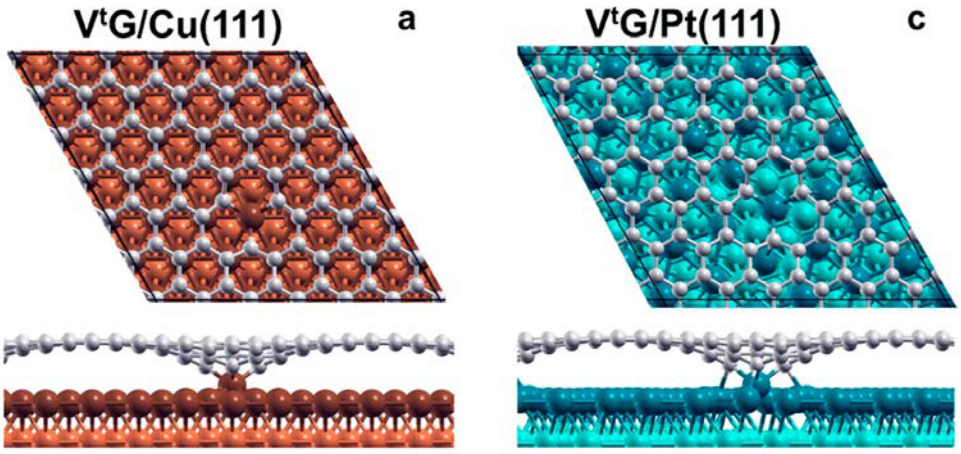


Figure 6.5 - Top and side views for G/Cu (a) and G/Pt (c). Color coding: C atoms in gray; first layer of Cu in dark brown and all other Cu atoms in brown; first layer of Pt atoms in dark blue and all other Pt atoms in light blue. Adapted from [130].

CO dissociation does not take place at regular bare Ni(111) sites. However, by introducing defects on a G/Ni(111) system, the ad molecules are trapped between the metallic substrate and the G layer. Since only traces of oxygen remain when annealing to 450 K, it is reasonable that a Boudouard reaction, catalysed by Ni, has occurred[131,132]:

$$2\,CO\,(ad) \underset{Ni}{\rightarrow} C + CO_2\,(g)$$

We thus conclude that vacancies allow CO adsorption in presence of a reactive substrate such as Ni. Intercalated CO molecules react when the system is annealed above 380 K leading to carbide formation, which can repair the vacancy and inhibit further CO adsorption in subse quent exposures.

The temperature range for the desorption of the molecules (between 350 and 400 K) falls in the same range of temperatures for which desorption off Ni(111) occurs, and their frequencies are close to those reported for CO adsorption on Ni(111).

If the vacancy itself would be reactive, as theoretical predicted for free standing graphene, adsorption should occur also for G*/$Cu_{poly}$, contrary to experimental evidence. The logical conclusion is that the adsorption occurs not *at the vacancy* but it intercalates between graphene and the Ni substrate: no adsorption can be observed for G* on Cu because the heat of adsorption of CO on Cu is too low for stable intercalation to occur.

Recently published results [133] however suggest an active role of vacancies in graphene grown on 4H SiC(0001): an enhancement of the reactivity has been observed for selective oxidation of the amino group and subsequent integration of the nitrogen within the graphene network.

The difference lies again in the substrate: in the former case the dangling bonds are saturated by bonding with the metallic substrate, while this does not happen on the carbon layer of SiC.

## 6.4 Conclusions

Since vacancies are active only in presence of a reactive substrate and annealing does not restore the initial reactivity, we also conclude that neither single nor double vacancies can be the active sites responsible for the previously reported [1,118,119], sensing of CO. We suggest, therefore, that the effect must be due to defects, which are rare for high quality G films. Possible candidates could be Stone Wales defects or edges of the graphene domains for which the heat of adsorption is notoriously higher than at pristine G sites (thus explaining the need for annealing to 150 °C to regenerate the sensor). No healing of such defects upon CO adsorption can occur (thus explaining the reversibility of detection upon annealing [1] or at high temperature [119]). The small density of such sites for G/Ni(111), as well as for G/$Cu_{poly}$, and their lower heat of adsorption with respect to vacancy sites requires a relevant CO partial pressure to gain a significant transient CO coverage. This explains why no CO adsorption is observed under the UHV conditions of our experiment: a partial pressure of $10^{-6}$ mbar corresponds indeed to a relative concentration of 0.001 ppm at atmospheric pressure, i.e. to an expected equilibrium coverage of CO three orders of magnitude lower than the sensitivity of our spectroscopies.

The role of vacancies in the chemistry of graphene is thus not as straightforward as pioneering theoretical studies for free standing graphene had suggested and the substrate does indeed play a key role. Other results indicate an active role of vacancies for functionalization. An enhancement of the reactivity towards selective oxidation of the amino group and the subsequent integration of the nitrogen atom within the graphene network was reported, e.g. for graphene deposited on 4H SiC [133]. The effect was ascribed to the excess of charge at carbon dangling bonds at single atomic vacancies. Graphene deposited on silica behaves thus differently from graphene on metals. The difference is presumably due to the formation of bonds between the C at the edge of the vacancy and the metallic substrate.

# 7 Synthesis of different boron-nitrogen-carbon heterostructures on Pt(111) and their reactivity with CO

## 7.1 Introduction

As already pointed out in the introduction, in the last few years, 2D materials, such as graphene, hexagonal–boron nitride (*h*–BN) and their combination have gained a clear prominence for their potential applications in next generation 2D atomic layer circuits, energy storage, electronic and novel spintronic devices [134,135] or as metal free electrocatalysts [136].

As discussed in section 5.1, after some understanding of the properties of pristine G has been reached, [95,96] attention has focused on the possibility to tailor these properties by introducing dopants such as N and B atoms [97–99], which either donate or withdraw free electrons.

A further challenge consists in the synthesis of co doped graphene layers in which more than one heteroatom species is present. For example, B and N atoms inside G have similar size, but opposite doping effects; therefore, their simultaneous presence at different concentration and relative ratio allows a tuning of the electronic band structure, band gap and chemical physical properties.

Several strategies of B and N doping or co doping of G have been developed in the last years. These preparation methods generally require the use of two or more molecular precursors in one or more synthesis steps, including chemical vapor deposition (CVD) [99,137–139], thermal annealing [140–142], plasma [106] and arc discharge [143,144] techniques, ball milling [145] or wet chemical methods [146,147] two step doping method [148] or ion exchange methods [149]. Following these routes, different B–N–C lateral and stacked layers have been synthetized [139,150–152]. Recently, more sophisticated three dimensional composites of G and *h*–BN have also been reported [153].

Recently, F. Bondino et al. have proposed a new one step route to get a layer formed by in plane complementary domains of *h*–BN and G (*h*–BNG) on Pt(111) using a single molecular precursor, dimethylamine borane (DMAB: $(CH_3)_2NH \cdot BH_3$)[154].

In this chapter, I report the follow up of this work, which I performed in collaboration with the research group mentioned above.

I show that using the same precursor but following different preparation routes, it is possible to get B N C layers with different composition. Besides *h*–BNG, also *h*–BN doped G and other B–N–C hybrids can be obtained just by tuning the substrate temperature (T). The bonding arrangement within B, C and N atoms strongly affects the electronic structure, enabling in principle to manipulate the chemical physical properties of B–N–C materials.

Two different preparation routes based on the thermal evolution of the precursor have been considered:

a) direct exposure of the hot (700–1000 K) Pt(111) substrate to precursor (HT);
b) molecular adsorption of DMAB on Pt(111) at room temperature (RT) followed by stepwise annealing in ultra high vacuum (UHV).

Both growth procedures were studied by two complementary spectroscopic techniques, high resolution X ray photoemission spectroscopy (XPS), performed at Bach beamline (Elettra Synchrotron Radiation Source) by F. Bondino and co workers, and high resolution electron energy loss spectroscopy (HREELS), performed at the Difi IMEM laboratory in Genova. We correlated the evolution of the C 1s, N 1s and B 1s core levels with the vibrational modes observed after every annealing or deposition step. For selected layers angle resolved photoelectron spectroscopy (ARPES), Pt 4f core level XPS and near edge X ray absorption fine structure spectroscopy (NEXAFS) measurements have also been carried out.

The *high temperature (HT) preparation method* consists in tuning the substrate temperature *during* the deposition of the precursor. This preparation allows a controlled growth of either co existing in plane G and *h*–BN domains (*h*–BNG) or hybridized B–C–N materials. The formation of *h* BNG heterostructures with large and distinct G and *h*–BN domains nearly free standing on Pt(111) was observed only at 1000 K [154], while at lower T hybridized B–N–C structures are obtained.

The alternative, *RT preparation method* consists in tuning the substrate temperature *after* the deposition of the precursor at RT. In this case, there is an initial formation of molecular adlayers with different intermediate species followed by a development of non planar BN structures, a decrease of boron and nitrogen content above 500 K and, finally, the formation of a G layer doped with small domains of both BN $sp^3$ and $sp^2$ structures and non planar B–N–C heterostructures above 1000 K.

## 7.2 Experimental

XPS, ARPES and NEXAFS measurements were carried out in the photoemission end station of the CNR beamline BACH at the Elettra synchrotron facility in Trieste, while vibrational spectroscopy experiments were performed in the Spectroscopy Chamber available at the Difi IMEM laboratory in Genova (see section 3.3).

In both experimental setups the preparations were performed *in situ*, under UHV conditions at a base pressure of ~$3x10^{-10}$ mbar. Before each DMAB exposure the Pt(111) single crystal (MaTecK, GmbH, 99.999% purity) was cleaned by sputtering with $Ar^+$ or $Ne^+$ ions at 1.5 kV at 300 K, followed by 120 s annealing at 873–923 K in $5x10^{-7}$ mbar $O_2$ partial pressure and flashed to 1023 K in UHV. Several cycles were performed until no traces of contaminants were detected by photoemission or HREELS. The degree of the long range order of the surface was monitored by low energy electron diffraction (LEED). The temperature of the sample was measured in

both setups by a thermocouple in direct contact with the crystal. Dimethylamine borane, DMAB (Sigma Aldrich, 97.0%) was contained in a glass tube and purified by several freeze pump thaw cycles. It was dosed on Pt (111) at a fixed T via a leak valve, while heating the vial at 314 K. In the HREELS apparatus a doser positioned at ~2 cm from the sample was employed to reduce the background pressure and improve vacuum recovery after the dose.

The pyrolytic decomposition of DMAB was obtained by dosing for 5–10 min on the Pt substrate, at four different temperatures: 700, 800, 900 and 1000 K at a partial pressure of $6.7\times10^{-7}$ mbar.

Molecular exposure was performed dosing DMAB on Pt substrate at RT (T≤310 K), followed by annealing steps from 340 to 1130 K.

XPS, ARPES and NEXAFS data were acquired using a VG Scienta R3000 hemispherical analyser. The core level spectra were measured at 60° from the normal emission using a photon energy of 520 eV and the total energy resolution was set to 0.2 eV. All photoemission binding energies are referenced to the Fermi level. The core level spectra were decomposed into spectral components using Doniach Šunjić line shapes convoluted with Gaussian profile, including Shirley type background.

| **Energy Losses at RT cm$^{-1}$ (meV)** | **Energy Losses at T>RT cm$^{-1}$ (meV)** | **$B_3N_3H_6$/Pt(111) [31] cm$^{-1}$** | **DMA/Pt(111) [28][30] cm$^{-1}$** | **Assignment** |
|---|---|---|---|---|
| | 363 460 (45 57) | 400 | | γ(BN) |
| | 709 (88) | 710 | | γ(NH) |
| | 871 (108) | | 887 | NH def. |
| | | 915 | | γ(BH) |
| | | | 999 | $\nu_s$(C–N) |
| 983 1008 (122 125) | 983 1008 (122 125) | | 1019 | $\nu_a$(C–N) |
| 1120 (139) | | | 1190 | $CH_3$ rock |
| 1411 (175) | 1338 1411 (166 175) | | 1451 | $CH_3$ as. def. |
| | | 1465 | | $\nu_a$(B–N) |
| | | | 1418 | $CH_2$ scissors |
| | | 2535 | | $\nu_a$(B–H) |
| 2934 (364) | 2950 (366) | | 2760 2930 | ν(C–H) |
| | | 3485 | | $\nu_a$(N–H) |

Table 7.1 – Summary of the vibrational frequencies observed in this work for DMAB on Pt(111) at RT (column 1) and upon annealing the layer. Previous results for $B_3N_3H_6$/Pt(111) (column 3) and DMA/Pt(111) (column 4) are reported for comparison. The assignment of the observed vibrational modes proposed from comparison with the cited papers is reported in column 5

The vibrational spectra were recorded in specular geometry, using a primary electron energy E = 5.0 eV and an angle of incidence of the impinging electrons of 62°. A typical resolution of ~56 $cm^{-1}$ (~7 meV) was achieved. Before collecting the spectrum, the sample was cooled down close to RT. Spectra are normalized to the inelastic background in the region around 450 meV, where no losses are ever present. Assignment of the vibrational frequencies is performed by analogy with previously investigated systems bearing similar vibrational modes of dimethylamine (DMA) on Pt(111) [155–157] and borazine/Pt(111)[158], as summarized in Table 7.1.

## 7.3 Results and Discussion

*High temperature preparation*. We firstly followed the HT growth protocol, which consists of the thermal decomposition of DMAB precursor catalysed by the hot Pt(111) substrate (700≤T≤1000K).

Figure 7.1 reports the evolution of the XPS C1s, B1s, N1s and Pt4f $_{7/2}$ core levels recorded for the layers obtained by growth at different temperatures of the Pt substrate: 700 K, 800 K, 900 K and 1000 K.

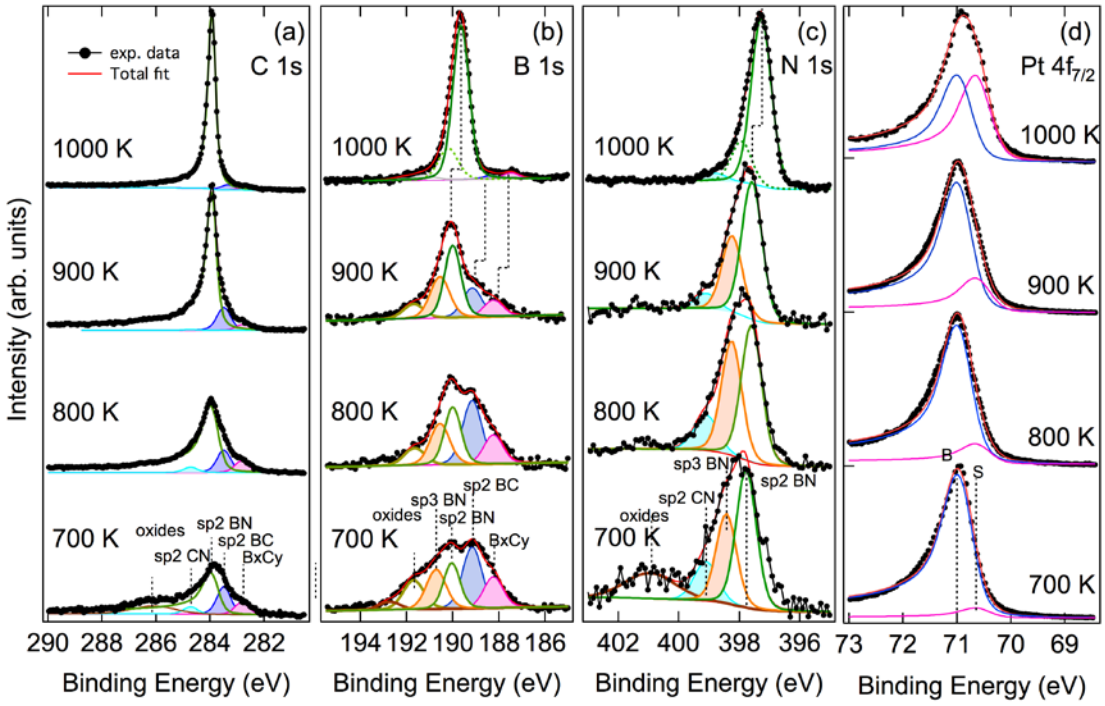


Figure 7.1 - C 1s, B 1s and N 1s XPS as measured spectra of DMAB dosed on hot Pt(111) at different temperature (700, 800, 900, 1000 K) and the corresponding Pt $4f_{7/2}$ normalized spectra. Green lines in N 1s, C 1s, B 1s correspond to $sp^2$ components. The blue and pink components in C 1s and B 1s correspond to B–C bonds ($sp^2$ BC and non-stoichiometric $B_xC_y$). The light blue components in C 1s and N 1s correspond to $sp^2$ CN bonds. The orange component in B 1s and N 1s are assigned to $sp^3$ B–N bonds. The dashed vertical line marks the upshift of the main peaks in N 1s and B 1s from 1000 K deposition to lower temperature deposition due to a stronger interaction of the layer with the substrate. The lines with markers are the experimental data. The red curves are the result of the fit.

Figure 7.2A shows the parallel HREELS experiment performed for a DMAB deposition at T=1000 K.

For the layer prepared at 1000 K the dominating peak in C 1s (Figure 7.1a) is located at 283.9 eV and it is assigned to $sp^2$ CC bonds in G like structures [159]. N 1s and B 1s spectra display slightly asymmetric peak shapes (Figure 7.1B and C). Each spectrum has been simulated with two components, a main peak at 189.7 and 397.3 eV for N 1s and B 1s, respectively, and a second weaker component at 190.1 and 397.9 eV, respectively. All these components are ascribed to $sp^2$ BN bonds in *h*–BN domains [160,161]. The presence of two $sp^2$ components shifted by 0.4 0.6 eV in each spectrum can be explained by the presence of a slight (~0.5 Å) geometrical corrugation in *h* BN domains [162], so that some *h* BN patches are located farther and some others closer to the Pt surface. The presence of a low binding energy component identical to that of the clean Pt surface in the Pt 4f core level (Figure 7.1D) and the strong polarization dependence of NEXAFS spectra [154] clearly indicate that both G and *h* BN domains are mostly flat lying and weakly interacting with the Pt substrate.

The vibrational spectrum recorded for the same layer (Figure 7.2A) shows almost no vibrational features. This is consistent with the planar nature of C–C (in G) and B–N (in *h*–BN) bonds, which are hardly detected by HREELS due to selection rules for dipolar scattering. However, a weak peak is detected around 983 $cm^{-1}$. This peak can be ascribed to the C N asymmetric stretch [155] likely from the bonds at the interface between *h*–BN and G domains. Such vibration is expected to be dipole active if the distance of G and *h*–BN from Pt(111) is different, so that the C N bonds at the border of adjacent G and *h*–BN domains are not planar. This is indeed the case since the distance from Pt is ~3.48 Å for G [163] and less than 3.1 Å for *h*–BN with a 0.5 Å corrugation of the *h*–BN layer and a 0.1 Å buckling between N and B atoms in *h*–BN [162]. An even weaker feature is present between 600 $cm^{1}$ and 750 $cm^{1}$, centred at 661 $cm^{1}$. Its origin is not clear, but it can be ascribed to C–B bonds (detected by XPS, see later), for example at the G/*h*–BN boundary, in analogy with the vibrations detected for boron carbides by infrared spectroscopy [164–166]. Finally, the very small shoulder at 363 $cm^{1}$ can be assigned to the BN deformation by comparison with the thermal evolution of the DMAB layer reported in Figure 7.2B and discussed later in the text.

For layers grown at T<1000 K, the C 1s, B 1s and N 1s spectra (Figure 7.1) get broader than those of the layer grown at 1000 K suggesting the presence of a different bond coordination. In detail, the C 1s spectrum is still dominated by the $sp^2$ C component, but additional shoulders appear. The high binding energy shoulder (around 284.7 eV, slightly visible) is mainly ascribed to C N bonds, but additional contributions cannot be excluded such as $sp^3$ defects [167], or hydrogenated bonds in G [168].

The low $E_B$ shoulders (283.4, 282.6 eV) are ascribed to carbon bound to one or two substitutional boron atoms [169,170] and to carbon bound to two substitutional boron atoms [169] or non stoichiometric $B_xC_y$, [170] respectively. These shoulders are slightly visible at 900 K, but more and more pronounced for the layers prepared at 800 K and 700 K.

The B 1s and N 1s spectra present two components each, ascribed to $sp^2$ and $sp^3$ BN bonds. They are at 190.1 eV and 190.8 eV for B 1s, and at 397.6 and at 398.3 for N 1s, respectively [171].

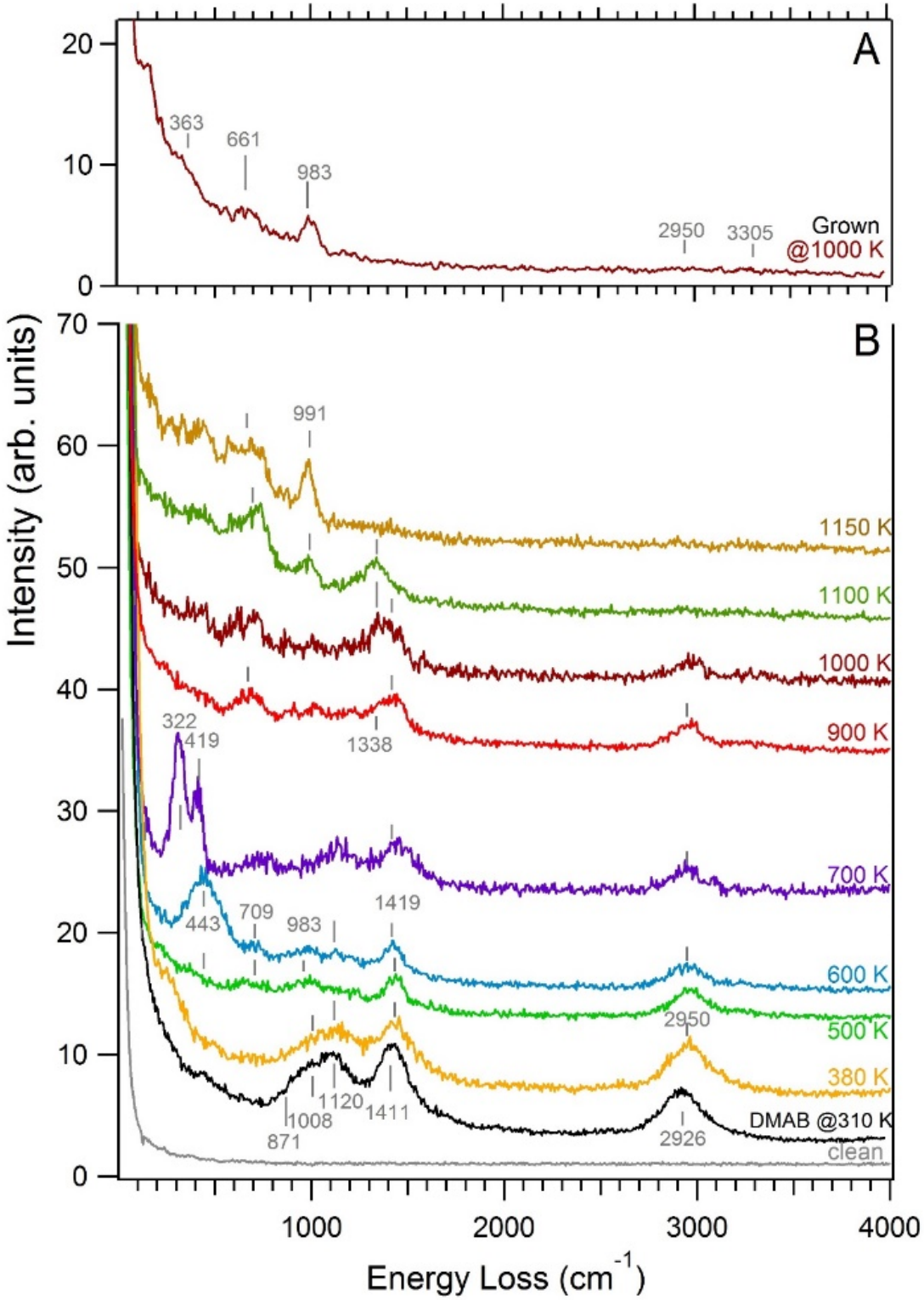


Figure 7.2 - A: HREEL spectrum (after a light smoothing process of the raw data) recorded after depositing DMAB on Pt(111) at 1000 K (DMAB dose: 600 s at P=5×10$^{-7}$ mbar). The peak is dominated by the $\nu_a$(CN) peak at 983 cm$^{-1}$ and by a weaker feature around 700 cm$^{-1}$, i.e. in the region for both the non-planar C-B bond motion and the $\gamma$(NH) mode. B: HREEL spectra showing the evolution of DMAB/Pt(111) from RT to 1150 K. The low energy peak related to the formation of BN aggregates starts to grow at 500 K and shows maximum at 700 K, where we can distinguish two different components of the BN vibration. These peaks completely disappear at 900 K. Above 1000 K also the CH stretch at 2950 cm$^{-1}$ disappears, while the CN asymmetric stretch at 991 cm$^{-1}$ becomes dominant.

The ~0.4–0.5 eV upshift with respect to the layer prepared at 1000 K can be explained by a stronger interaction of the deposited layer with the Pt substrate; this hypothesis is supported by the decrease of Pt $4f_{7/2}$ low energy component intensity [see Figure 7.1D].

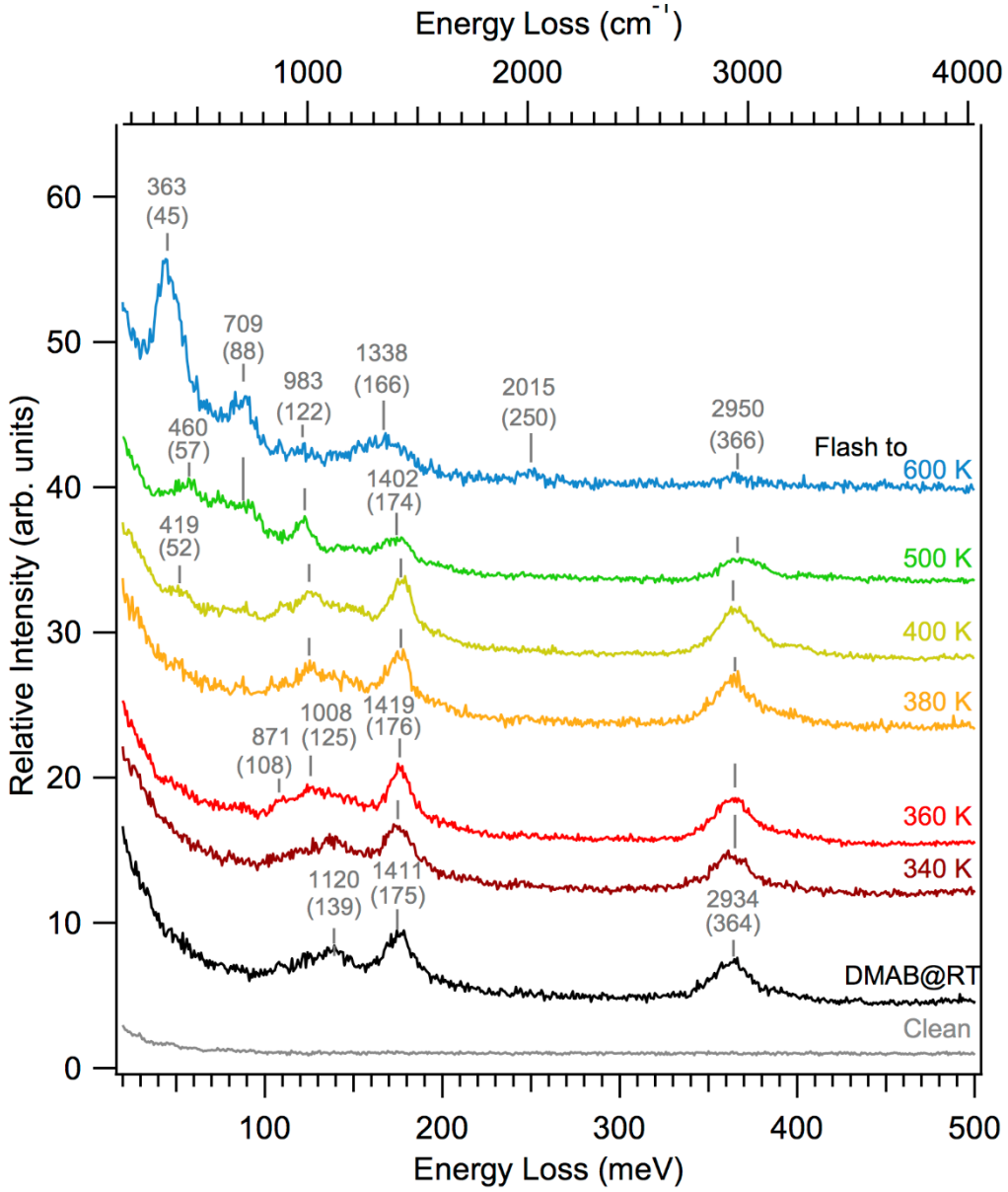


Figure 7.3 - HREEL spectra showing the evolution of DMAB/Pt(111) from RT to 600 K. Although the sample was prepared under nominally identical conditions as the one of Figure 2B of the manuscript, a slightly lower initial coverage is achieved in this case. Considering that these data were recorded before those of Figure 2B, a possible explanation is that the degree of purification of the DMAB in the glass vial was not exactly the same but improved with time in vacuum and with the additional cool-pump-heat cleaning cycles performed before each sample preparation.

In N 1s there is a further component located at 399 eV which can be assigned to N C bonds [105,172]. In the B 1s region, additional peaks at 189.2 eV, 188.2 eV and 191.7 eV are present. The first two components can be ascribed to B–C bonds with different coordination in B doped G domains with different doping levels [169,170] and/or at the boundaries of the hybridized G and *h*–BN domains [99,172]. The 189.2 eV B 1s component can be associated with $sp^2$ BC bonds

of carbon bound to one substitutional boron atoms [170] in the honeycomb lattice, while the 188.2 eV peak to bonds in non stoichiometric $B_xC_y$ boron carbide [170]. The 191.7 eV component is probably an oxide originating from residual oxygen contamination, [170,173], such as some hydroxides/oxidized species formed during DMAB evaporation in spite of the repeated purification cycles. For the sample grown at 700 K all core levels display extra weak and broad components at 192.7 eV, 401 eV and 286.1 eV for B 1s, N 1s and C 1s, respectively, which can be attributed to oxidized species [170,173].

When the layer is obtained by depositing the molecules on the substrate at 1000 K, large, ordered and well defined *h*–BN and G domains form and all core levels display mainly only G or $sp^2$ BN components. For 700 K≤T≤900 K, on the contrary, a large multi component distribution is observed in the XPS spectra due to the presence of different coordination numbers, as it was previously observed in B–N–C film prepared using different protocols of growth [172,174–176]. These components can originate for example from species at the boundary between hybridized G and *h*–BN domains, B doped/N doped G areas or domains with C–N–B or C–B–N coordination.

For the HT preparation method at 1000 K the relative atomic concentrations of N, B and C are 21%, 25% and 55%, respectively. For the layers prepared at 700–900 K, the concentrations are approximately 17%, 31% and 52%. The relatively higher concentration of boron with respect to nitrogen at the lower temperatures can be assigned to simultaneous formation of boron nitride and boron carbide or $B_xN_yC_z$ (y>x) species accompanied with desorption of some nitrogen in the form of $N_2$ and $NH_3$ molecules.

B K edge and N K edge NEXAFS spectra recorded at two different angles (s and p polarization – not shown) clearly indicate that the samples grown at 900 K, 800 K are made of G, *h*–BN and B–N–C domains with various atomic compositions and almost flat geometry. Vice versa, the growth at 700 K produces B–N–C structures with non planar bonds.

*Room temperature preparation*. The second on surface synthesis procedure that we have examined was the thermal evolution of the molecular layer deposited at RT followed by stepwise annealing up to 1150 K.

Figure 7.2B and Figure 7.3 show the evolution of the HREELS spectra recorded after exposing the Pt(111) surface at RT to DMAB and step annealing to the indicated temperatures. The two experiments differ for the starting experimental conditions. The former sequence refers to a preparation with a slightly higher initial DMAB coverage and to a complete annealing range (from RT to 1150 K); the latter is performed starting from a lower initial coverage and annealing only up to 600 K in smaller steps. The tentative assignments of the observed vibrational frequencies are reported in table 1. The corresponding evolution of the XPS core levels and the area of the different components deduced from the fitting procedure are shown in Figure 7.4 and Figure 7.5, respectively. In Table 7.2 we summarize the proposed assignments for the binding energies of B 1s, C 1s and N 1s components.

| T RANGE (K) | B 1s (eV) | Assignment | N1s (eV) | Assignment | C1s (eV) | Assignment |
|---|---|---|---|---|---|---|
| 300 -500 | 188.8 | BH | 398.3 | NH in DMA | 285.4 | $CH_3$ in DMA |
| 300 -500 | | | 399.7 | –N–C–Pt amino carbyne | 286.1 | –N–C–Pt amino carbyne |
| 300 | | | 401 | Physisorbed species | | |
| 300-500/ 500 -1130 | | | | | 283.9 | C or CH/ $sp^2$ CC |
| 400 -1130 | 190.1 | $sp^2$ BN | 397.6 | $sp^2$ BN | | |
| 400 -1130 | 189.2 | $sp^2$ BC | | | 283.4 | $sp^2$ BC (C bound to one substitutional B) |
| 400 -1130 | | | 399 | $sp^2$ CN | 284.7 | $sp^2$ NC bonds, $sp^3$ defects, hydrogenated G |
| 400 -600 | | | 397.0 | $CN_{ads}$ /Pt | | |
| 400-1130 | 190.8 | $sp^3$ BN | 398.3 | $sp^3$ BN | | |
| 500-1090 | 188.2 | Non-stoichiometric B–C $B_xC_y$ | | | 282.6 | Non-stoichiometric $B_xC_y$, C bound to two substitutional B |
| 500-1000 | 191.7 | Oxidized species | | | | |

Table 7.2 - Summary of the B 1s, N 1s and C 1s binding energies observed in this work during the stepwise annealing up to 1130 K after RT deposition of DMAB on Pt(111). The proposed assignment of the observed XPS components is reported in column 4. For the references and more details, see text.

At RT DMAB adsorbs on Pt surface in a dissociated form consisting of the main parts of the molecule. In fact, the DMAB complex is formed by two units, dimethylamine (DMA, $(CH_3)_2NH$:) and borane ($BH_3$) stabilized through a dative bond. The two molecular units are highly polarized, and they can easily interact with the 5d electrons of Pt surface atoms. The HREEL spectrum (Figure 2b) recorded after DMAB deposition at RT shows four main features: two overlapping peaks at 1008 $cm^{-1}$ and 1120 $cm^{-1}$, a single loss at 1411 $cm^{-1}$ and one at 2926 $cm^{-1}$. From the comparison with previous vibrational studies of DMA/Pt(111) [155,157] (see Table 1), we assign these frequencies to the C N asymmetric stretch (1008 $cm^{-1}$), $CH_3$ rocking mode (1120 $cm^{-1}$), $CH_3$ asymmetric deformation mode (1411 $cm^{-1}$) and CH stretching mode (2926 $cm^{-1}$). We also underline the presence of a weak tail around 900 $cm^{-1}$, which is most probably due to the presence of unresolved components corresponding to the NH deformation mode at 871 $cm^{-1}$, the BH out of plane motion, $\gamma$(BH)[158] and the symmetric stretch vibration $\nu_s$(C–N) vibrations. The absence of a significant intensity in the region below 800 $cm^{-1}$, in which a $\gamma$(BN) vibration is expected (around 320–420 $cm^{-1}$), proves that DMAB adsorbs in the dissociated form (DMA+BH fragments) already at RT. The presence of $BH_3$ on the surface is unlikely since on Pt(111) this species is metastable at RT and tends to dissociate into (BH+2H)*, due to the high activity of Pt(111) for B H dissociation and strong binding of the so formed fragments [177]. On

the other hand, no signature of Pt–H stretching modes [178,179] is observed. This is not surprising considering the weak cross section of atomic hydrogen under the employed measuring conditions.

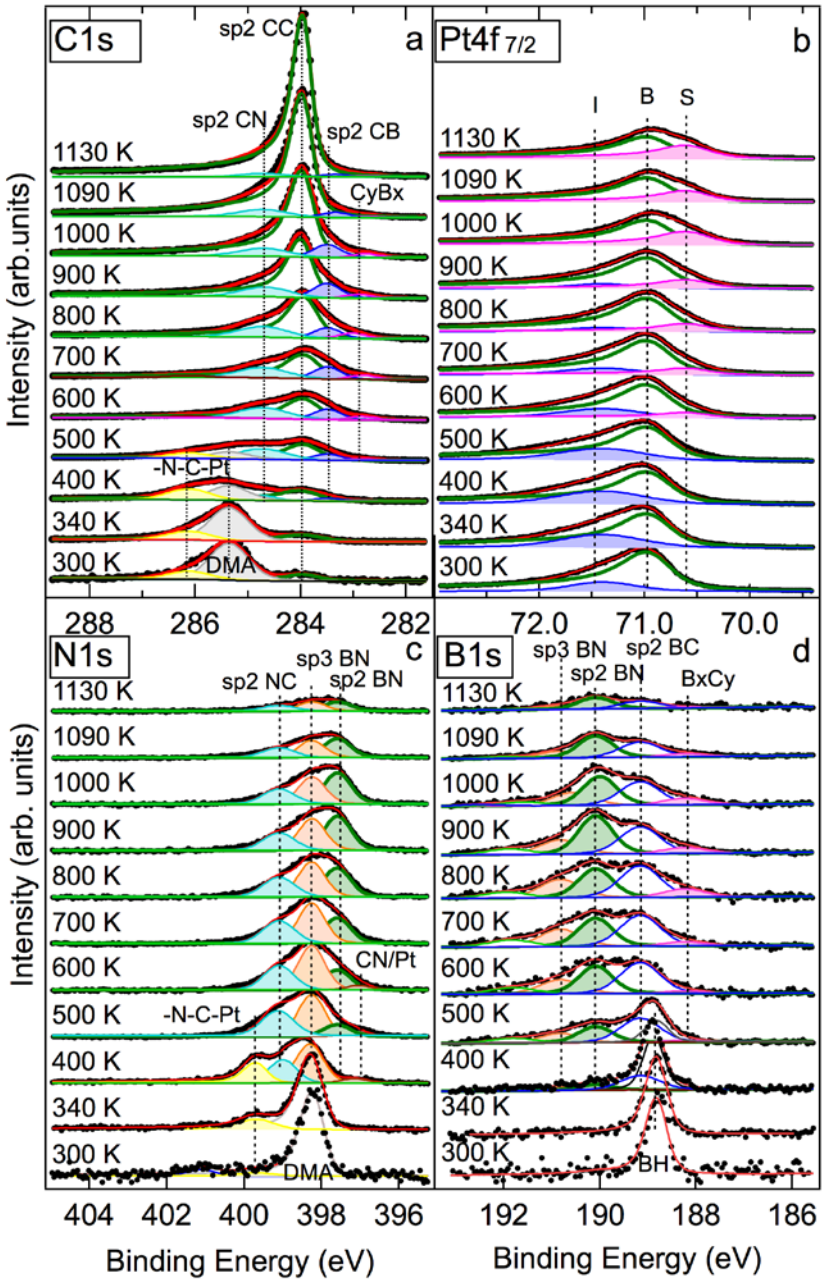


Figure 7.4 – XPS thermal evolution of B 1s, C 1s and N 1s core levels of DMAB after RT deposition followed by stepwise annealing up to 1130 K. In C 1s, N 1s and B 1s the grey components are ascribed to DMA and BH adsorbed fragments, the light blue components to $sp^2$ CN bonds, the blue and pink components to $sp^2$ BC and nonstoichiometric $B_xC_y$ bonds, the yellow components in Pt–C–N– bonds, the green components to $sp^2$ bonds, the orange components to $sp^3$ BN bonds. For more details and further discussion on the assignment, see text. In Pt, the three components are labelled B (Pt bulk atoms), S (Pt atoms at the interface, weakly bond to the overlayer) and I (Pt atoms at the interface, strongly bound to overlayer species). The lines with markers are the experimental data. The red curves are the result of the fit.

Moving to the photoemission experiment, we observe that, at RT, three peaks are present in the C 1s region (Figure 7.4A) at 285.4 eV (associated with the C atoms inside methyl groups [180,181] of DMA), 286.1 eV (ascribed to different molecular intermediate species containing –N–C–Pt bonds such as acetonitrile/methylisocyanide ($CNCH_3$)[155,157,180]) and 283.9 Ev (due to isolated atomic C[58] and/or CH[59] adsorbed species). This last component remains at the same binding energy up to the highest investigated temperature, T=1130 K, but with a progressively lower width.

The B 1s spectrum (Figure 7.4D) shows a single peak at 188.8 eV likely due to the expected BH species on the surface. In the N 1s region (Figure 7.4C) a main component is observed at 398.3 eV that can be ascribed to NH in adsorbed DMA. A further small peak around 401 eV may be related to a second layer/physisorbed species disappearing above at 340 K. An additional feature at 399.7 eV disappears above 500 K (in parallel with the C 1s peak at 286.1 eV) and can be associated with species adsorbed with one or more amino carbyne groups through a –N–C–Pt bond [155,156]. Interestingly, the Pt 4f spectrum (Figure 7.4B) can be decomposed in two peaks: the former is ascribed to Pt bulk atoms [154], the latter, upshifted by 0.50 eV, corresponds to Pt atoms strongly bound to DMAB fragments [154].

Between RT and 400 K we observe the evolution from the DMA + BH fragments into molecular intermediate species.

At 380 K the NH deformation mode at 871 $cm^{-1}$ disappears from the HREEL spectrum. This indicates an evolution of the surface catalysed reaction with a conversion of DMA to different surface intermediates. Such behaviour is confirmed by inspection of XPS. Above 300 K the DMA methyl carbon component at 285.4 eV decreases and the component at 283.9 eV (adsorbed C or CH species) grows up.

Between 400 K and 600 K, a new N 1s component around 397.0 eV is also present but its assignment is not clear. The binding energy is compatible with HB N(H) bonds (e.g. HB $N(H)CH_x$) but also with the presence of atomic N species [182,183] or of CN adsorbed molecular species (N 1s BE=397.0–397.4 eV, C 1s BE=284.1–284.3 eV for $CN_{ads}$ /Pd or $CN_{ads}$/Rh) [184,185]. Indeed the presence of surface CN adsorbed intermediate species above 400 K has also been detected in previous RAIS investigations of the DMA thermal evolution on Pt(111) [155]. At T=400 K no variations were detected in the Pt $4f_{7/2}$ spectrum, indicating the presence of species that are still strongly bound to the substrate. We interpret all the changes observed in the 300 K to 500 K T range as a signature of the progressive dissociation of the methyl groups in the intermediate molecular species and of the consequent formation of different adsorbed species on Pt.

From 400–500 K up to 1090 K a clear evolution takes place in the XPS spectra. At 400–500 K, the narrow 398.3 eV N 1s component associated with NH species in DMA is replaced by a broader one at around the same binding energy and by a further peak at 399 eV.

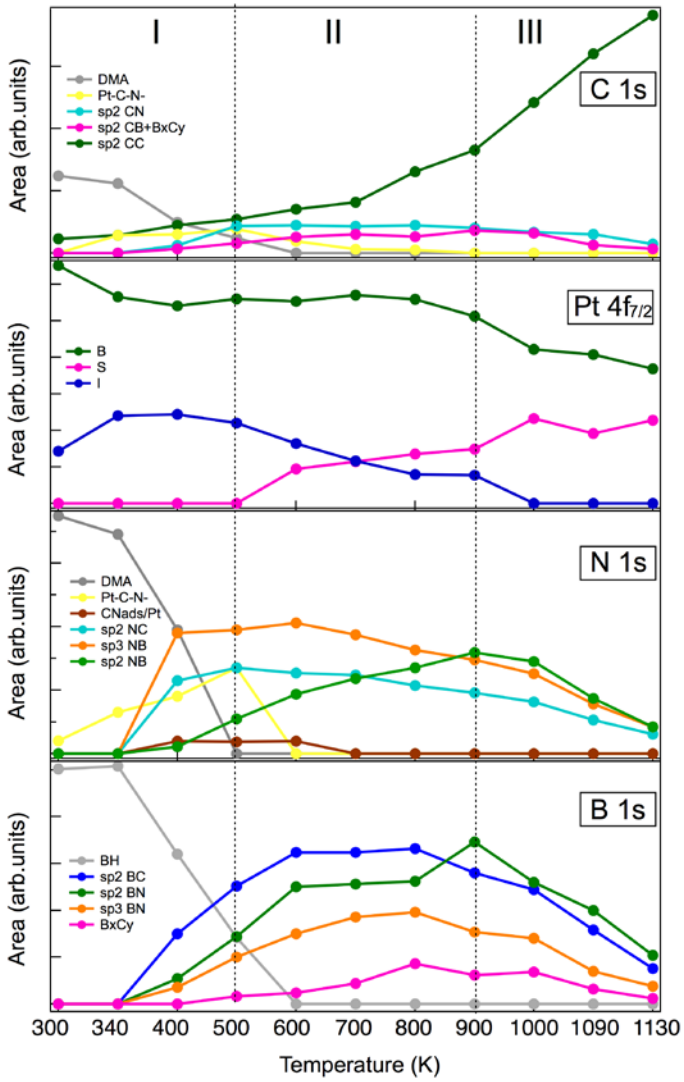


Figure 7.5 – Evolution of the areas of the fitting components in the XPS spectra reported in Figure 7.4 as a function of the stepwise annealing. I, II, and II mark the three phases described in the text.

Simultaneously, B 1s components at 189.2 eV and 190.8 eV and new C 1s components at 284.7 eV and 283.4 eV appear. The C 1s peak at 284.7 eV and the N 1s component at 399 eV can be associated with $sp^2$ CN bonds such as in pyridinic ones[45]. Additional contributions such as $sp^3$ defects [167], or hydrogenated G [168] may also contribute to the 284.7 eV component. The 189.2 eV B1s and 283.4 eV C 1s components can be associated with $sp^2$ BC bonds of carbon bound to one substitutional boron atoms [170] in the honeycomb lattice. The 190.8 eV B 1s component and the broad one in N 1s at 398.3 eV are instead associated with $sp^3$ BN bonds [186]. At the same temperature $sp^2$ BN bonds start to develop. This is indicated by the appearance of features at BE= 190.1 eV and 397.6 eV in B 1s and N 1s core level spectra, respectively, and in parallel by the growth of a new vibrational feature around 419 $cm^{-1}$ in HREEL spectra, signature of the formation of BN bonds (Figure 7.3).

At 500 K the 419 $cm^{-1}$ vibrational peak moves to slightly higher frequency and a second vibration at ~709 $cm^{-1}$ grows up. The position of the latter peak is compatible both with non planar motion of C–B bonds (697 $cm^{1}$) [164,166] and out of plane NH motion (710 $cm^{1}$) [158].

Furthermore, the peak associated with the C–N asymmetric stretch mode becomes more pronounced and narrower. At such T we also see a reduction of the intensities of the $CH_3$ deformation and CH stretch modes, which also are slightly shifted to 1419 $cm^{-1}$ and 2950 $cm^{-1}$, respectively. All these changes are consistent with a substantial de hydrogenation as observed in a previous temperature programmed desorption study of DMA/Pt(111) between 340 K and 425 K [155]. HREELS data confirm therefore that the molecules are still de hydrogenating and that new species may form on the surface, in agreement with XPS results.

Above 500 K the high BE components associated with amino carbyne disappear from both C 1s and N 1s spectra and at the same time further components grow up at 282.6 eV and 188.2 eV, which can be associated with C–B [172] bonds in non stoichiometric $B_xC_y$ boron carbide [170]. Above 500 K also the main C 1s component (283.9 eV) gradually becomes sharper and more intense (the peak width in the fit is progressively reduced). Such behaviour is due to a gradual formation of $sp^2$ CC bonds in a more and more ordered and larger G layer. The B 1s and N 1s spectra show a small gradual increase of the $sp^2$ BN bond related components up to 900 K. Concurrently, the Pt $4f_{7/2}$ peak at BE=71.4 eV starts to decrease and the low energy component at BE=70.6 eV appears, confirming the formation of weakly interacting species such as G and *h*–BN.

In the vibrational spectra, annealing to 600 K leads to an intense and relatively broad out of plane B–N vibration centred at 443 $cm^{1}$, which converts into a doublet at 322 and 419 $cm^{1}$ at 700 K, possibly indicative of the formation of two non equivalent sites/compounds. Above this T the intensity of these modes starts to decrease.

Above 900 K B 1s and N 1s spectra do not show any further changes in their shape, but only a progressive decrease in the overall intensity. In parallel, all the C 1s components decrease with exception of the $sp^2$ one, which gets more and more intense and sharper. The pronounced increase of C in the layer at high T is likely due to additional C atoms coming from the Pt substrate.

At variance with C 1s, even after a flash at the highest T (1130 K), neither the B 1s nor the N 1s core levels get narrow, nor downshift as it happens after the formation of large *h*–BN domains by deposition DMAB on hot Pt at 1000 K. In XPS spectra, besides the $sp^2$ BN components there is always a significant contribution of the components associated with C–B and $sp^3$ BN bonds. Thus, from the core levels there is no evidence of the presence of large *h*–BN domains even after the flash to T=1130 K.

Annealing to T=900 K causes significant changes also in the HREEL spectrum, since the lowest energy peaks (in the 320–450 $cm^{-1}$ range) disappear while the mode at ~709 $cm^{-1}$ increases slightly. The disappearance of the B–N out of plane vibrations can be associated with the

change in their orientation with respect to the surface normal. However, it is only above 1000 K, that complete de hydrogenation of the organic layer occurs, as witnessed by the vanishing of the CH stretch mode at 1100 K and of the $CH_3$ asymmetric deformation at 1150 K.

We note how the vibrational spectrum (Figure 7.2) and XPS core levels obtained upon annealing the DMAB layer deposited at RT to 1000 K are qualitatively different from the one recorded after deposition directly at this T, to confirm the different products generated by the two growth methods. However, the B 1s, C 1s, N 1s NEXAFS spectra collected after annealing to 1000 K (not shown) indicate that at this T most of the bonds (C–C, B–N, C–N) are in the plane.

At 1150 K the vibrational spectrum is flat except for the presence of a peak at 991 $cm^{-1}$ and a broad feature around 600–800 $cm^{-1}$. The former frequency is associated again with the CN asymmetric stretch while the large feature at lower energy can contain more than one com ponent consistent with out of plane motion of C–B bonds [164,166]. The simultaneous presence of C–N and C–B related vibrations can be ascribed either to non planar bonds at the boundary between *h*–BN and G domains or to the presence of B–N–C hybrids. This agrees with XPS data, where components due to $sp^3$ BN, C–N and C–B bonds are still detected even at 1130 K.

The presence of the low energy component in Pt 4f core level (Figure 7.4D) indicates that the layer obtained after annealing at 1130 K is also weakly interacting with Pt(111). However, the formation of uncovered areas of Pt cannot be excluded for this layer.

For the RT preparation method, we estimated that, after the deposition, the N,B and C atomic concentration ratios are close to the stoichiometric values, as expected from the atomic composition of the DMAB molecule or fragments, while at 1130 K the relative concentrations of N and B decrease to 3.6% and 7.1% respectively.

Therefore, following the stepwise annealing method after RT DMAB deposition, a G layer with a smaller amount (11%) of B, N and BN is formed at 1130 K. This layer is still weakly interacting with the underlying substrate and non planar bonds are present at the domain boundaries.

In summary the thermal evolution of DMAB during the stepwise annealing from RT up to 1130 K can be described as composed of three phases (see Figure 7.5): in the first one (from RT to 400/500 K) the DMA + BH fragments change their atom coordination to form molecular intermediate species that are strongly interacting with Pt substrate. In the second phase (from 500 to 900 K) a significant evolution of the molecular fragments takes place leading to the formation of $sp^2$ and $sp^3$ BN, CN and BC bonds. In the third phase (from 900 to 1130 K) a gradual disappearance of B–N, C–N and B–C bonds occurs, and the simultaneous formation of large and weakly interacting G domains is observed.

### 7.3.1 Preliminary results on the chemical reactivity of the B-N-C layers

In order to study the chemical reactivity of the layers produced following the RT and the HT growth methods, we have exposed them to CO dosed at room temperature and at low temperature.

The spectra in Figure 7.6 were recorded after exposing the layer obtained with the RT growth protocol after 40 L of CO dosed at 100 K. Two vibrational peaks are detected at 236 and 257 meV, which can be associated with the C O stretch of CO ad molecules in two different adsorption sites. The two peaks are unchanged after flashing the sample at 170 K, while after flashing at 220 K a small decrease of the intensity has been observed for both beaks.

They completely disappear after heating the sample at 273 K so that the desorption temperatures of both species must lie in between 220 and 273 K and thus differ by less than a few tens of degrees. This is at variance with the results obtained for n doped graphene on Ni(111) (see Section 5.3 and Figure 5.3): in that case the two adsorbed species showed a significantly dif ferent desorption temperature enabling to associate the less strongly bound moiety to CO at pristine sites and the more strongly bound one to "doping related" adsorption sites. In the present case, on the contrary, both species can be associated with doping related adsorption sites.

It is likely that the low energy mode corresponds to doubly coordinated (bridge site) CO while the high energy one to singly coordinated (on top) ad molecules, and from the desorption temperatures we can estimate that the adsorption energies per molecule are comprised between 0.6 and 0.7 eV

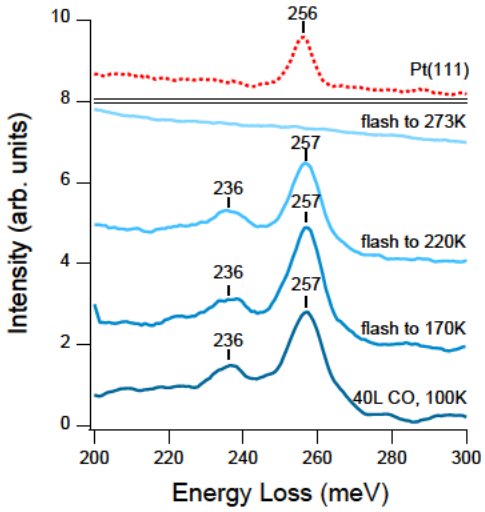


Figure 7.6 – HREELS spectra show CO adsorption at low temperature on the RT preparation: two vibrational modes are visible and both of them disappear after flashing at 273 K. The red spectra reported as comparison is taken after exposing the clean Pt(111) to the residual CO present in the chamber.

We can exclude the occurrence of CO adsorption on the bare Pt(111) since in that case, as reported in the red spectra reported in Figure 7.6 , only a single vibrational peak is detected in

the low coverage limit and since such species is stable at room temperature and desorbs only around 500 K [187].

The same CO adsorption experiments have been performed also on the film resulting from the HT preparation method, and the results are reported in Figure 7.7A. No CO adsorption has been detected after exposing the sample at Room Temperature (red spectra) or at 90 K (green spectra) even after a quite large dose of CO (1000 L, blue spectra) indicating that the produced layer is inert towards CO.

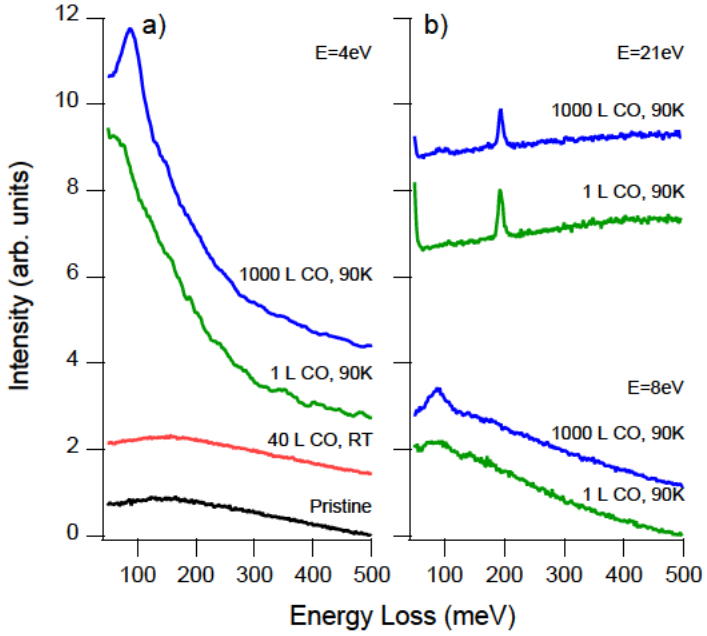


Figure 7.7 – (a) No CO adsorption is detected on HREEL spectra for the HT preparation exposing the sample either at room temperature (red) or at 90 K (green) even after a huge dose (blue). When the sample is cooled down a large feature appears at low energy which is due to an acoustic plasmon. - (b) no adsorption is detected also in spectra recorded with a primary energy of 8 eV (bottom) and 21 eV (top). The sharp feature visible in the top spectra at 194 meV is due to a phonon.

The conclusions we can draw from this last set of experiments must be taken with caution: while the fact the film we grew is chemically inert holds valid, it must be noted that the spectra of the pristine film we obtained here (Figure 7.7A, black line) are noticeably different from the spectra of the previous experiment (Figure 7.2A, dark red line), despite the fact that the same preparation protocol has been followed in these experiments. In particular, no trace of the C N vibration at 122meV could be detected in the spectra recorded before CO exposure, while the only visible structure is a very large feature centered around 150meV. This feature is enhanced on the spectra recorded at low temperature (Figure 7.7A, green and blue). We believe that this is due to the excitation of an acoustic surface plasmon of the graphene layer, containing only little amount of h BN. Unfortunately, no XPS spectra could be recorded on this preparation due to technical problems with the instrument, thus we could not determine the rela tive amount of carbon, boron and nitrogen *in situ*.

The chemical inertness of the film is confirmed by HREELS spectra recorded using different electron energies as reported in Figure 7.7B where no signal of CO vibration modes could be detected. The only molecular vibration we detected (90meV peak in the lower blue spectra recorded with E=8eV) is due to some water contamination detected after keeping the sample at low temperature for long time.

The sharp peak visible around 194 meV while using higher energy electrons (E=21eV) is due to a phonon of the film we have grown. We thus decided to exploit the possibility of detecting phonons in order to obtain additional informations on the film, and we recorded spectra in off specular conditions at different scattering angles. The results are reported in Figure 7.8A.

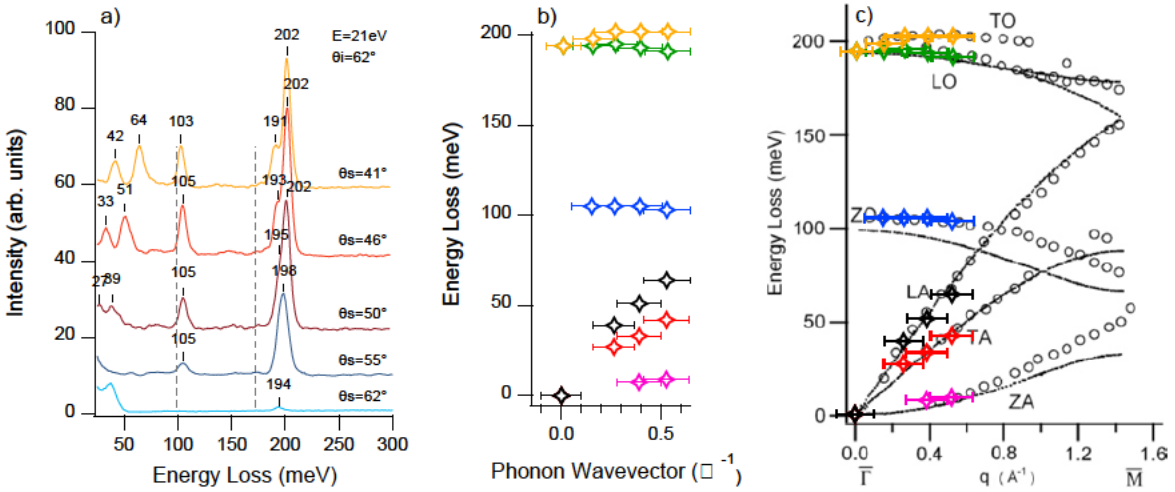


Figure 7.8 – (a) HREELS spectra recorded using an electron energy E=21eV and at different scattering angles in order to trace the (b) phonon dispersion. As shown in panel c) the data are compatible with the phonon dispersion measured for a graphene layer grown on Pt(111) [188]. The dashed lines in panel (a) refers to the expected phonons energies of h-BN [189].

Given the energies of the different phonons detected at various scattering angles and knowing the geometrical parameters and the energy of the electrons we used, we can obtain the phonon dispersion curves reported in Figure 7.8B. Comparison with the phonon dispersion of a pure graphene layer grown on Pt(111) [188] shows excellent agreement. It is remarkable that the phonons expected for a layer of h BN [189] (dashed lines in Figure 7.8A) are not present.

We thus conclude that the film we obtained is mostly graphene, and, while we cannot completely exclude the presence of traces of h BN, their relative amount is less than few % of the layer at maximum (less than the experimental error affecting our measurements).

This difference with the previous experiment we performed can be justified considering that in the reactivity experiments a different, newly polished, Pt(111) single crystal was used, with an unknown quantity of dissolved carbon embedded into the bulk of the sample. The carbon content in the bulk might indeed result in the production of a layer, which is different from the

usual mixed layer obtained while using a sample, which had undergone many cleaning cycles, and increase the graphene fraction at the expense of the h BN patches.

Nevertheless, the result we obtained still holds significance: even if we obtained a layer made ony (or mostly) of graphene, the chemical inertness supports the conclusion drawn in chapter 4.4. The role of the substrate is essential in enhancing the chemical properties of graphene: only strongly interacting substrates like Ni(111) can lead to a chemically reactive supported graphene layer, while less reacting substrates like copper and also Pt(111) cannot.

I am aware of the preliminary nature of these results and I plan to perform additional experi ments to draw more definitive conclusions about the chemical reactivity of the layer obtained with the HT protocol.

## 7.4 Conclusions

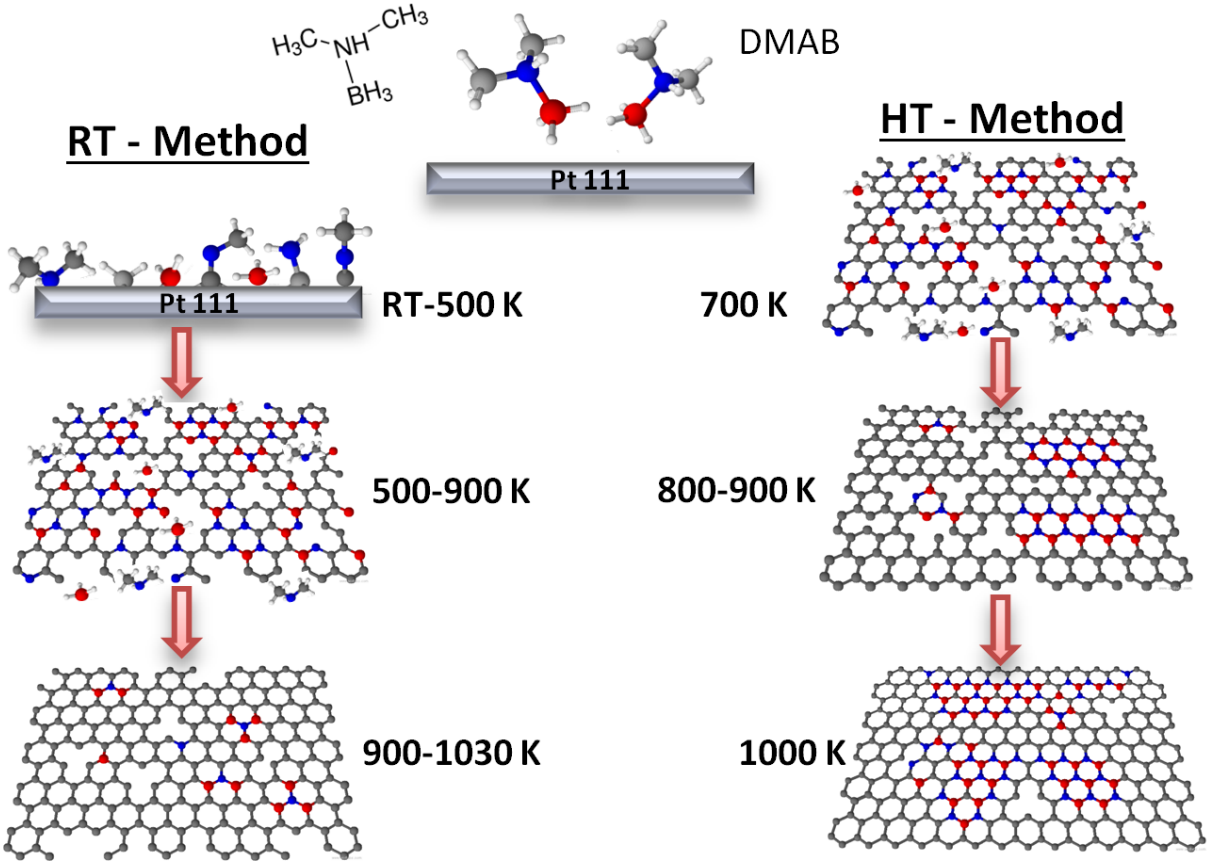


Figure 7.9 – Schematic representation of the two processes studied and the resulting layer obtained – RT temperature deposition of the DMAB molecule and subsequent heating results in a weakly interacting graphene layer with a low doping by B, N and BN species embedded inside the layer. – HT deposition leads to a monolayer composed of both graphene and h-BN domains.

In conclusion, a selective control of the B–N–C bonding is simply achieved by tuning the substrate T either during or after the deposition of a molecular precursor, dimethylamine borane (DMAB) on Pt(111). We have compared the different layers obtained upon pyrolytic decomposition of DMAB dosed on the Pt(111) substrate at high T (700≤T<1000 K), or upon stepwise

annealing of a molecular layer deposited on Pt(111) at RT. By monitoring the evolution of the core level and vibrational spectra, both layers have been characterized.

Upon pyrolytic decomposition, the layer obtained at 1000 K consists of a continuous monolayer formed by complementary *h*–BN and G domains on Pt(111), as schematically indicated in the right side of Figure 7.9. At lower T non planar hybridized boron carbonitride (BCN) layers were observed.

Upon stepwise annealing of the layer deposited at RT, a weakly interacting G with few B, N species inside is formed at the highest T (1130 K) (Figure 7.9, left side). At lower T (340 K–500 K) we observed the evolution from a DMA molecular layer to intermediate stable molecular species towards a progressive intermolecular coupling after molecular rearrangement and bond activations.

Preliminary results about the chemical reactivity of the RT and HT produced films suggest that only the film resulting from the RT method is reactive towards CO. The reactivity can be due to the corrugated nature of the film or to doping.

Two different adsorbed species could be detected (probably an on top and a bridge configuration) both desorbing between 220 and 273 K.

The inertness of the HT layer indicates, on the other hand, that pristine G sites for G/Pt(111) are inert as expected for graphene when its interaction with the substrate is weak.

# 8 Graphene on 6H-SiC(0001) and its reactivity with atomic hydrogen

## 8.1 Introduction

Graphene is a one atom thick layer with extraordinary properties and numerous applications ranging over the most varied fields, including nano electronics and hydrogen storage. The use in nano electronics exploits the high mobility of its carriers. It has, however, been shown that the latter is affected and significantly reduced by the interaction with the support so that de-coupling of graphene from the substrate is necessary [7]. Intercalation provides an effective way to attain this goal whereby the result depends critically on the final morphology of the layer [190]. Hydrogen storage in graphene has been extensively investigated, too, because of its relevance for sustainable mobility. Dissociation of $H_2$ may occur at reactive substrate sites below the graphene layer after its intercalation or at convex sites on a curved graphene sheet [191,192].

H intercalation under graphene on Ir(111) [193,194], on Ni(111)[13] and on SiC(0001) [7,195–202] has been studied with surface science methods providing the gas either from the gas phase as $H_2$ at high pressures and at high crystal temperature or as H in ultra high vacuum via an atomic hydrogen source. In the former case, $H_2$ penetrates through defects of the graphene layer or through the edges of the graphene domains. Indeed free standing graphene is impermeable to He, Ar and air [203]. The mechanism is less clear when H is provided in atomic form.

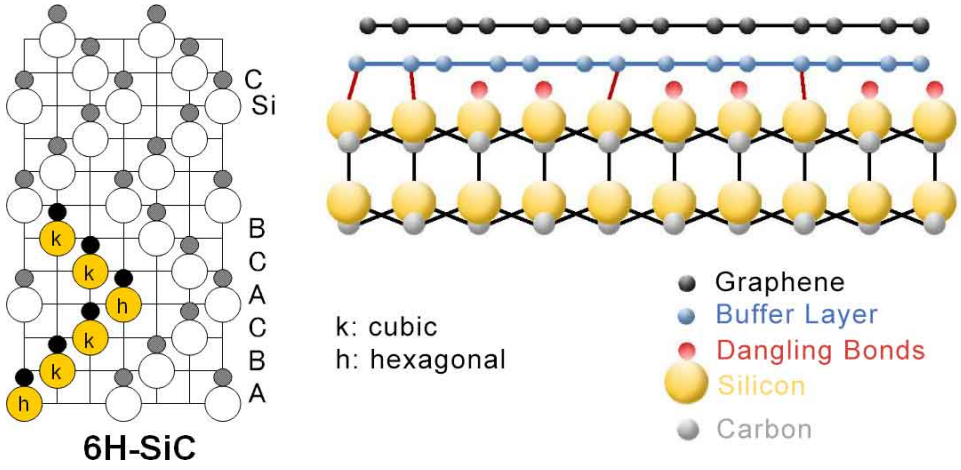


Figure 8.1 - *side views of: left) 6H SiC (Si atoms yellow, carbon atoms grey) and right) bare graphene/SiC system, consisting of a buffer layer (also addressed as zero-layer, bluish atoms) with about 30% of Si-C bonds and of an outer layer (black atoms), which is an intrinsically n-doped graphene monolayer.*

In SiC, the Si C bond has 88% of covalent character and a bond length of 1.89 Å, while the Si Si distance is 3.08 Å. The crystalline structure can be viewed as resulting from a compact packing of double layers consisting of C and Si. Depending on the packing sequence, different polytypes can be obtained. They are classified following Ramsdell [204]: the letters C, H, R indicate

thereby the three possible Bravais lattices (cubic, hexagonal and rhombohedric, respectively). Some of the most common polytypes are shown in the figure.

The case of graphene on SiC is particularly intriguing since it is nearly free standing and in contact with a large gap semiconductor; in addition, H intercalation detaches the carbon buffer (or zero) layer present between graphene and SiC. Detachment of graphene from SiC has also been attained by intercalation of Li atoms [205] for the purpose of understanding Li ion batteries. Intercalation was then demonstrated to occur at room temperature via the step edges. For Li/Graphene/SiC system the barrier for the process is 3.98 eV at pristine sites and lower at Stone Wales defects (3.52 eV for heptagonal arrangements and 1.15 eV for octagonal arrangements of the C atoms) [206].

Here we present new data for the adsorption of atomic hydrogen on graphene grown on 6H SiC.

## 8.2 Experimental

The sample is provided by NovaSiC and consists of a 6H SiC single crystal with a monolayer of graphene grown on it by thermal treatment. As shown in Figure 8.1 right panel the bare surface consists of a buffer layer (also addressed as zero layer) with about 30% of Si C bonds [7]. The topmost layer consists of intrinsically n doped graphene layer.

$H_2$ ($D_2$) is provided through a doser pointing towards the sample. The gas is dissociated by a hot W filament (light yellow taint, ~1400 K) placed in between doser and sample at 3 cm from the surface. A reactive H or D gas is thus produced at the temperature of the filament, corresponding to a distribution centred at $\sim 0.1$ eV energy. Undissociated hydrogen molecules do not stick on graphene/SiC so that their partial pressure does not affect the experiment. The exact exposure is not known since it depends on the dissociation probability and on the local pressure enhancement due to the doser. The exposure is therefore given in Langmuirs of the molecular $H_2/D_2$ partial pressure read at the pressure gauge position and this value has only a relative significance. The factors connected to dissociation efficiency of the cracker and doser local pressure enhancement must, however, nearly compensate since we observe important effects already between 4 and 40 L exposure, implying a significant H/D coverage.

## 8.3 Results and discussion

We investigated experimentally the adsorption of atomic H (and D) on G/6H SiC by High Resolution Electron Energy Loss Spectroscopy (HREELS). The latter technique enables to obtain information on the plasmaron frequency resulting from the hybridization of the graphene acoustic plasmon and the SiC Fuchs Kliewer mode and on the H/D carbon vibration. H in deeper layers is too heavily screened to contribute to the inelastic signal.

In Figure 8.2 we show the outcome of a hydrogen (panel A) and deuterium (panel B) uptake performed on the sample at T~320 K. The spectra were recorded in specular (incidence and

reflection angles $\theta_{in}=\theta_s=55°$) with a primary electron energy E=12 eV. The position of the maximum has been determined by fitting the peak in an interval of approximately 50 meV around it with a Gaussian function.

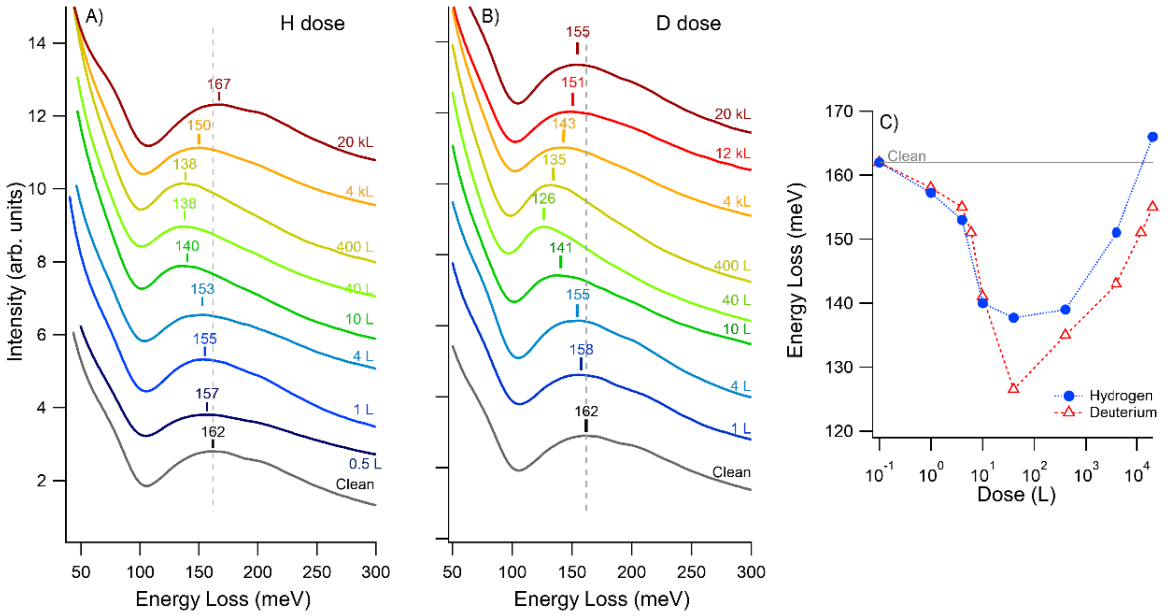


Figure 8.2 - HREELS spectra recorded in-specular following H (Panel A) or D (panel B) uptakes and frequency of the ω+ component of the plasmaron vs exposure (panel C). The exposure is given in Langmuir of the H2/D2 partial pressure at the position of the pressure gauge. For both isotopes, the loss red-shifts with exposure, reaches a minimum energy at 40 L and then recovers to the initial energy. The effect is largest at 40 L exposure for both isotopes (32 meV shift for D and 24 meV for H). An isotope effect is present since the downshift is larger for deuterium (ΔE=32 meV for D and 24 meV for H) but at large exposures H recovers more efficiently the original value (E=12eV, θin=θout=55°).

In Figure 8.3 we show the corresponding spectra of the CH stretch region recorded at E=5 eV and under non specular scattering conditions ($\theta_{in}$ = 62° and $\theta_s$ =47°) corresponding to a good loss intensity. Panels A and B refer to the H and D uptakes, respectively, panel C reports the intensity of the CH /CD stretch as a function of exposure.

The spectra recorded in specular for the clean surface exhibit the typical features reported in the literature and summarized in Figure 8.4 for graphene on SiC. Two broad energy losses, ω and $\omega_+$, are expected, which result from the hybridization of the graphene plasmon with the SiC Fuchs Kliewer phonon ($\omega_{SO}$ = 940 cm $^1$, 116 meV). In our spectra (see Figure 8.2), ω appears as a shoulder of the elastic peak while $\omega_+$ corresponds to the well defined loss in the 130 165 meV energy range. A further shallow maximum is visible around 205 meV.

Such feature, indicated as $\omega_{++}$ in Figure 8.4, corresponds to the hybridization of the graphene plasmon with the graphene $\omega_{LO}$ phonon (at 1600 cm $^1$ or 198 meV). Such maximum was reported also by Koch et al. [207], and, according to their theoretical model [208], it should be most intense for the double graphene layer produced by detaching the zero layer from the SiC substrate by H intercalation (see right panel H QFBLG).

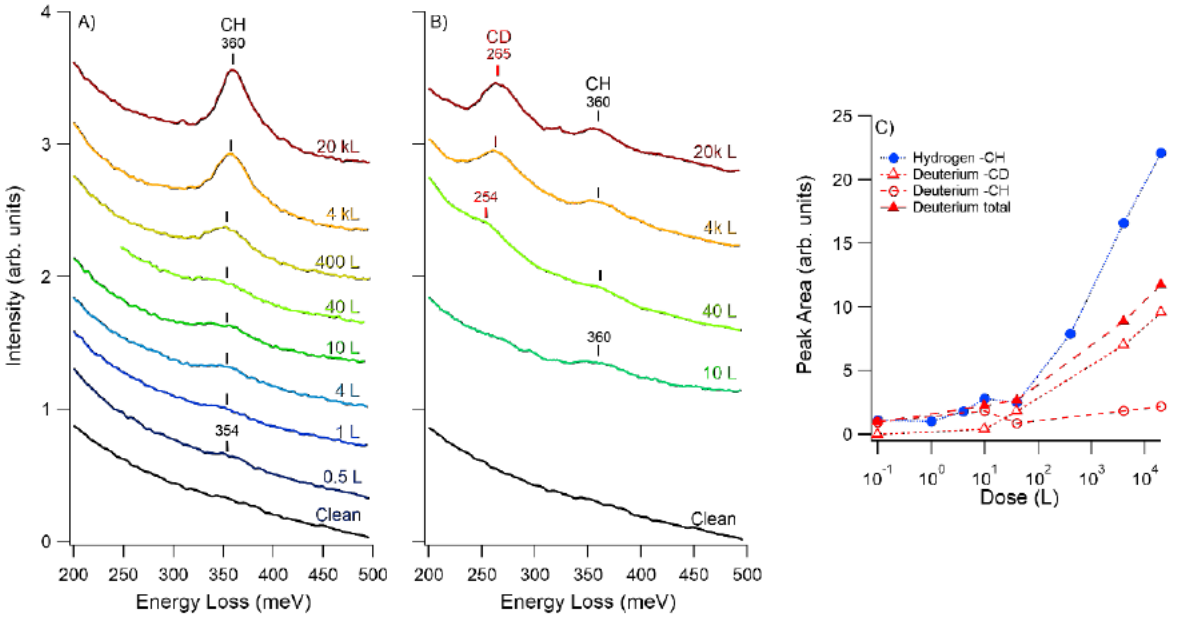


Figure 8.3 – Off-specular HREEL spectra (panels A and B for H and D exposures, respectively) and loss peak area vs H/D exposure (panel C). Deuterium –CH indicates the intensity of the weak CH loss observed when D is exposed and originating, most probably, to some contamination from the H2 present in the background atmosphere of the chamber and dissociating in presence of the hot filament. (E=5eV, θin=62° θout=47°)

In such conditions according to ref. [208] the $\omega_+$ mode red shifts by ~7 meV. Such effect is results from the lower doping level associated to the detaching of the graphene layers from the SiC substrate.

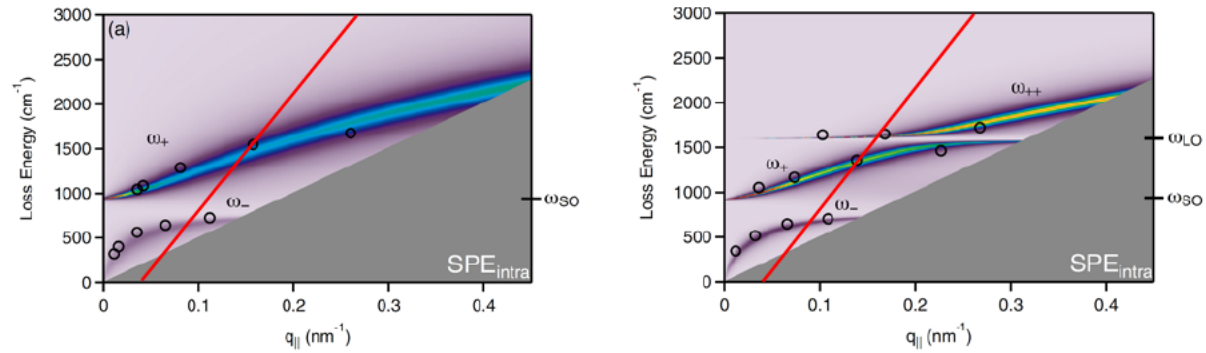


Figure 8.4 - Calculated surface loss function as a 2D color-coded intensity map for monolayer graphene (left panel) and H-QFBLG (right panel). The three branches of the coupled phonon-plasmon dispersion are marked by ω–, ω+, and ω++. ωSO and ωLO correspond to the energy values for the SiC Fuchs Kliewer mode and the graphene longitudinal optical phonon, respectively. The black circles mark the peak positions in the HREELS spectra taken at different primary beam energies by Koch et al. The gray shaded triangle corresponds to the area where single particle electron hole excitations are possible (SPEintra). The red line indicates the theoretical scan curve for the experimental geometry and energy used in-specular for the present investigation (E=12eV, θin=θout=55°). Figure taken from ref [208].

From the spectra of Figure 8.2, we notice that the energy of the $\omega_+$ is strongly affected by exposure to H/D. Initially, it decreases with H coverage (panel A) and D coverage (panel B), red shifting from 162 meV for the bare graphene to 138 meV and 128 meV after 40 L of H or D, respectively. Such shift is not accompanied by relevant CH or CD signals neither in specular

(Figure 8.2) nor off specular (Figure 8.3), thus excluding the presence of a significant coverage of adsorbed H(D) on the topmost graphene layer.

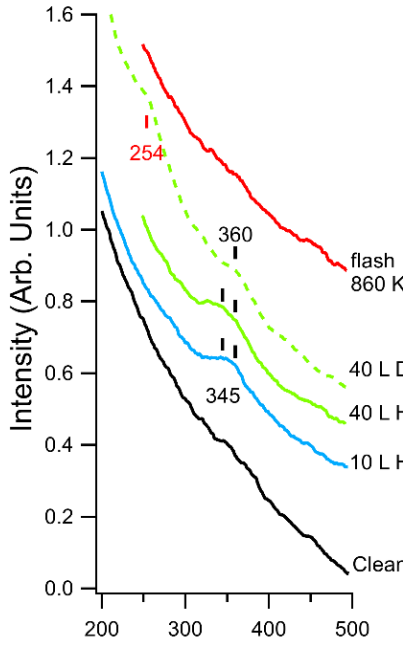


Figure 8.5 - Comparison of the spectra recorded off-specular ($E_P$=5eV, $\theta_{in}$=62° $\theta_{out}$=47°) for different H/D exposures. Unfortunately, some intensity at 360 meV remained after flashing the sample complicating the analysis of H dosed samples. The loss recorded for the 40 L H dose is centered at lower energy implying the presence of lower frequency components as expected for H adsorbed on one side of the carbon layer only.

Indeed, in such conditions a faint loss is present at 360 meV, resulting from residual H traces which survived previous annealing procedures, as mostly evident for the D exposures in Figure 8.3. As shown in Figure 8.5, at the lowest exposures (10 and 40 L) such loss is accompanied by a further component around 345 meV for H (254 meV for D). The lower energy loss value is indicative of H atoms sitting on one side of the graphene film only (or possibly of the buffer layer) [193,209].

Above 40 L exposure, the shift in the plasmaron frequency reverts, reaching asymptotically a value close to the one of the bare graphene film, the CH/CD stretch intensity, measured off specular, increases and upshifts to 360 meV (265 meV), see Figure 8.3. This loss energy indicates graphanization of the film, i.e. H adsorption at both sides of the graphene layer, since it is close to the value of 353 meV reported for H on $sp^3$ hybridized carbon samples. Such process is not complete even at the largest exposures since the plasmaron loss persists, proving that a graphene layer is still present.

In Figure 8.6 and Figure 8.7, we show the evolution of HREEL spectra upon annealing the surface exposed to 40 L and 4000 L of H (D), respectively, to the given temperature.

Annealing the layer dosed with 40 L H(D) we observe that the plasmaron shifts back to almost the bare surface value around 580 K. The remaining small difference is recovered only after heating to 1050 K, the effect being more marked for the hydrogenated surface than for the deuterated one.

For the 4000 L dosed samples the effect on the plasmaron is smaller since it moves up in frequency with hydrogen dose. The larger intensity of the CH stretch mode allows to trace it vs dose. Our data show that it nearly remains constant up to 450 K and then drops rapidly to about 1/3 of its initial value. Such drop is correlated with an energy upshift of the plasmaron by some 6 meV.

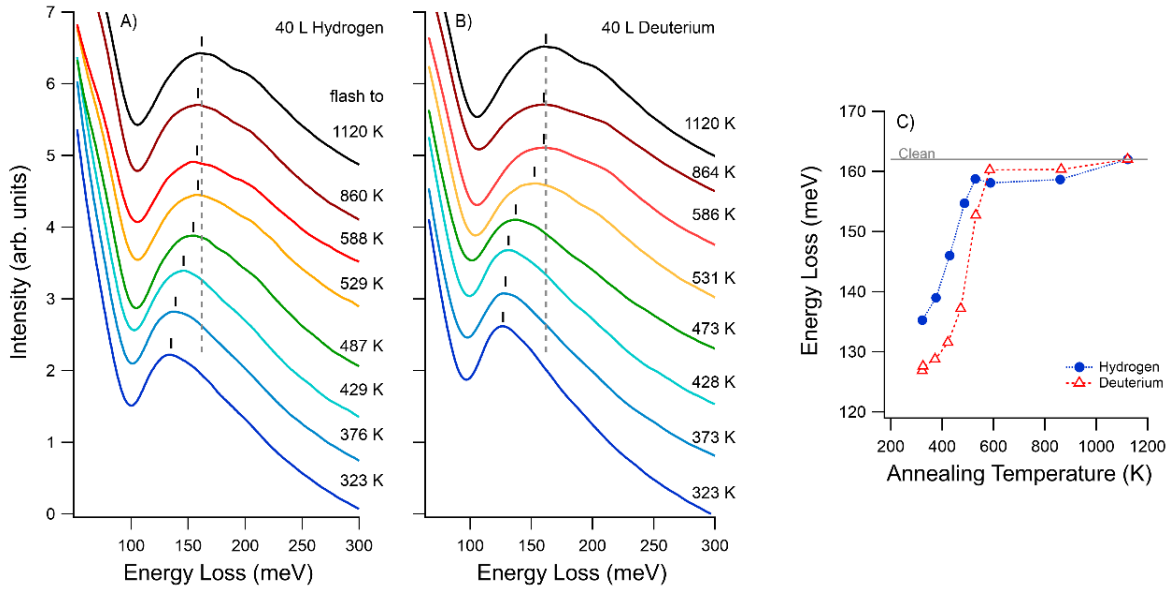


Figure 8.6 – Spectra recorded in specular after annealing the graphene layer pre-exposed to 40 L H (panel A) or D (panel B) at different temperatures. The frequency of $\omega_+$ as a function of the annealing temperature is shown in panel C. The sample was cooled back to room temperature before recording the spectra.

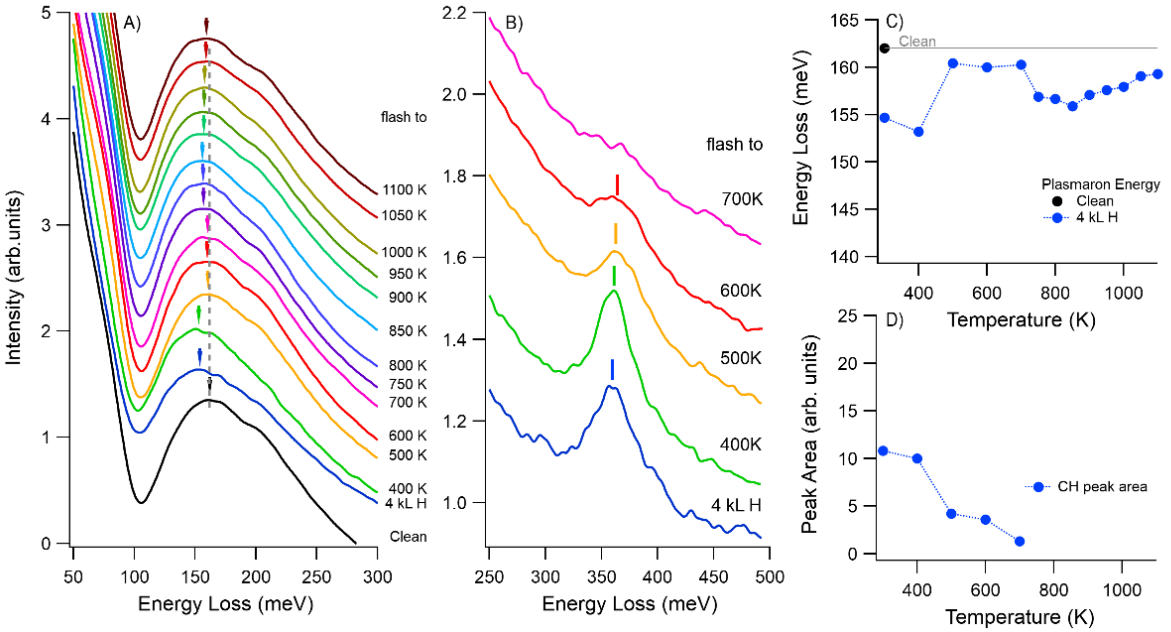


Figure 8.7 – HREELS Spectra of the $\omega_+$ *region* recorded in specular (panel A) and of the CH stretch region recorded off-specular (panel B) after annealing the graphene layer pre-exposed to 4000 L of H. Panels C and D show the frequency of $\omega_+$ and the intensity of the CH stretch loss vs annealing temperature, respectively.

Heating further the intensity of the CH loss faints around 700 K. Interestingly at the same temperature $\omega_+$ redshifts by some 3 meV. Though small we believe that such effect is real since it is consistently present in the subsequently recorded spectra. Also in this experiment the bare system plasmaron energy is recovered only when annealing above 1050 K. Interestingly 700 K

correspond to the temperature at which H may intercalate through the buffer layer, while de intercalation occurs at 1050 K.

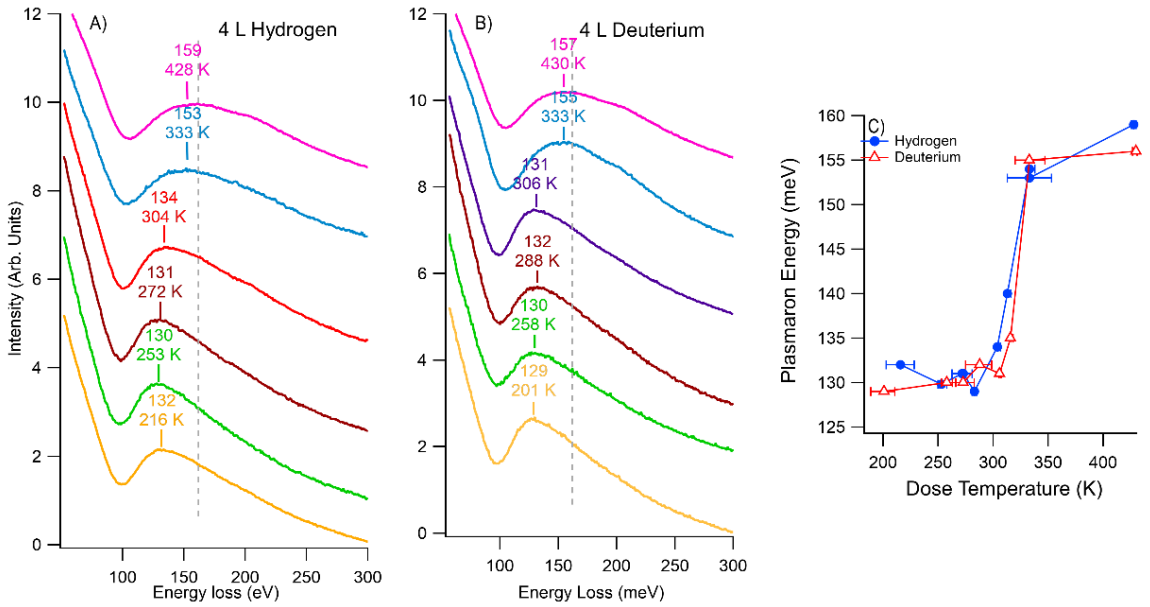


Figure 8.8 – HREEL spectra recorded in specular after exposure to 4 L of H (panel A) or D (panel B) at different temperature. The data are recorded after cooling back the sample to room temperature or liquid nitrogen temperature depending on the investigated temperature range. The loss frequency does not change with crystal temperature. Panel C shows the plasmaron frequency $\omega_+$ after dosing at the different sample temperatures.

In Figure 8.8 experimental spectra recorded after a short (4 L) exposure to H/D at different substrate temperatures are shown. Between 200 and 300 K, the frequency $\omega_+$ is independent of exposure, while dosing at higher temperature causes only a minor shift of the plasmaron with respect to the bare surface value indicating that H exposure becomes less effective.

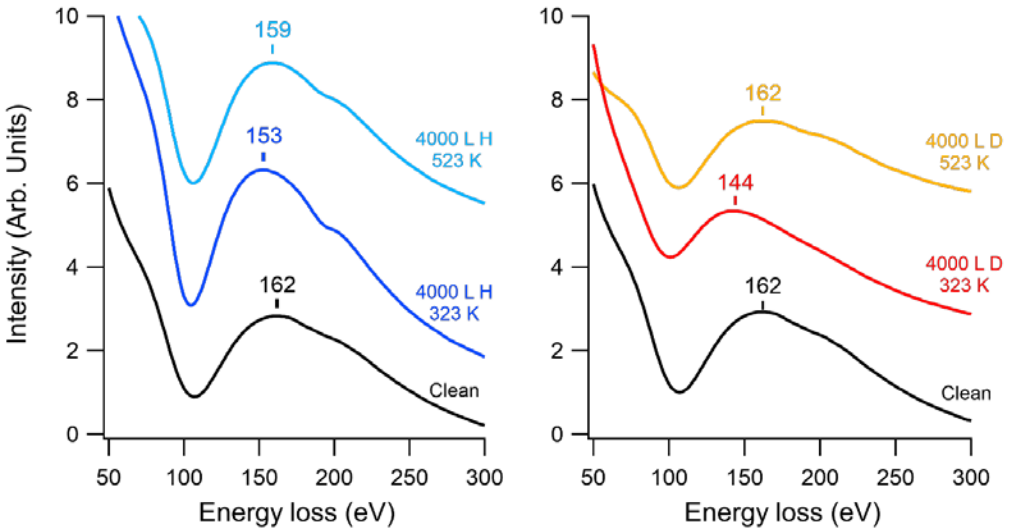


Figure 8.9 – Spectra recorded in-specular following exposure to 4000 L of H/D (left and right panels, respectively) performed at two different temperatures of the sample.

In Figure 8.9 a similar experiment is shown for high exposure (4000 for H and 8000 L for D). While at 323 K causes a significant red shift of the plasmaron frequency, exposure at T ≥ 520 K leaves $\omega_+$ nearly unaffected. This result clearly correlates with the outcome of the experiments at lower doses reported in Figure 8.6 and Figure 8.7, which indicates that the process does not occur above 450 K especially for D.

## 8.4 Discussion

By inspection of our data it is apparent that:

1) A relatively low exposure to H /D, if performed below or around 300 K, causes a significant (> 15 meV) red shift of the plasmaron frequency. A weak and broad CH peak is then visible at 345 meV/260 meV for H/D in off specular spectra.
2) With increasing exposure to H/D, the plasmaron frequency blue shifts attaining a value slightly higher (H) or lower (D) than the one observed for the bare surface. The CH (CD) stretch visible in off specular spectra has now a vibrational frequency around 360 meV for CH (260 meV for CD).
3) Upon annealing the layer exposed to 40 L H/D, the plasmaron frequency of the bare surface is recovered at around 450 K.
4) When annealing the layer exposed to 4000 L H, the CH stretch decreases to about 1/3 of its initial value around 450 K while $\omega_+$ blue shifts by some 5 meV. Around 700 K the intensity of the residual CH stretch vanishes and $\omega_+$ red shifts again by some 4 5 meV. The value of $\omega_+$ of the bare surface is fully recovered only after annealing above 1050 K.
5) There is an isotope effect in hydrogen adsorption at large dose. From the frequency shift of $\omega_+$ vs H dose we infer that at large exposures H is about 30 times more efficient than D.

| SYSTEM | CH (meV) | CD (meV) | REFERENCE | NOTES |
|---|---|---|---|---|
| HOPG | 295: monomers;<br>330: dimers;<br>345: clusters | 243: dimers<br>257: clusters | Aréou et al. [210] | Hot H(D) from plasma<br>HREELS |
| G/Ir(111) | 305: dimers<br>335: clusters<br>360: defects | | Kyhl et al. [194] | H from hot capillary<br>HREELS |
| G/Ir(111) | 318: para dimers<br>337:ortho dimers | 233: para<br>251: ortho | Kim et al. [211] | H/D from hot capillary<br>SFG |
| Gr/Ir(111) | 353: $sp^3$ bound H/D | 264 | Kim et al. [209] | H/D hot capillary; SFG |
| Diamond(111) | 352 | 262 | Chin et al. [212] | Filament cracker<br>HREELS |
| Crystalline graphane | 353: graphane | | Kolesnikov et al. APS March Meeting 2012, abstract #H11.010 | IR |

Table 8.1 – HREELS vibrational mode of CD and CH on different graphene like systems

We also observe that the frequency of the CH stretch observed in our case for significant H/D exposures is significantly higher than the one reported by Aréou et al. [210] for H/graphite (335 meV). This result as well as the absence of the CH stretch loss for in specular experiments indicates that H/D adsorption takes place in our case on both sides of the G layer [193]. The lower frequency reported by Bisson et al. corresponds indeed to H adsorption only above the graphene plane.

An overview of the energy losses reported in literature for similar systems is shown in Table 8.1.

Our results can be rationalized as schematized in Figure 8.10 – Scheme of the coverage and temperature evolution. The buffer layer (also addressed as zero layer) is drawn as a corrugated grey line with about 30% of Si C bonds (outermost Si atoms are drawn as blue circles). Gra phene is represented as a black line.

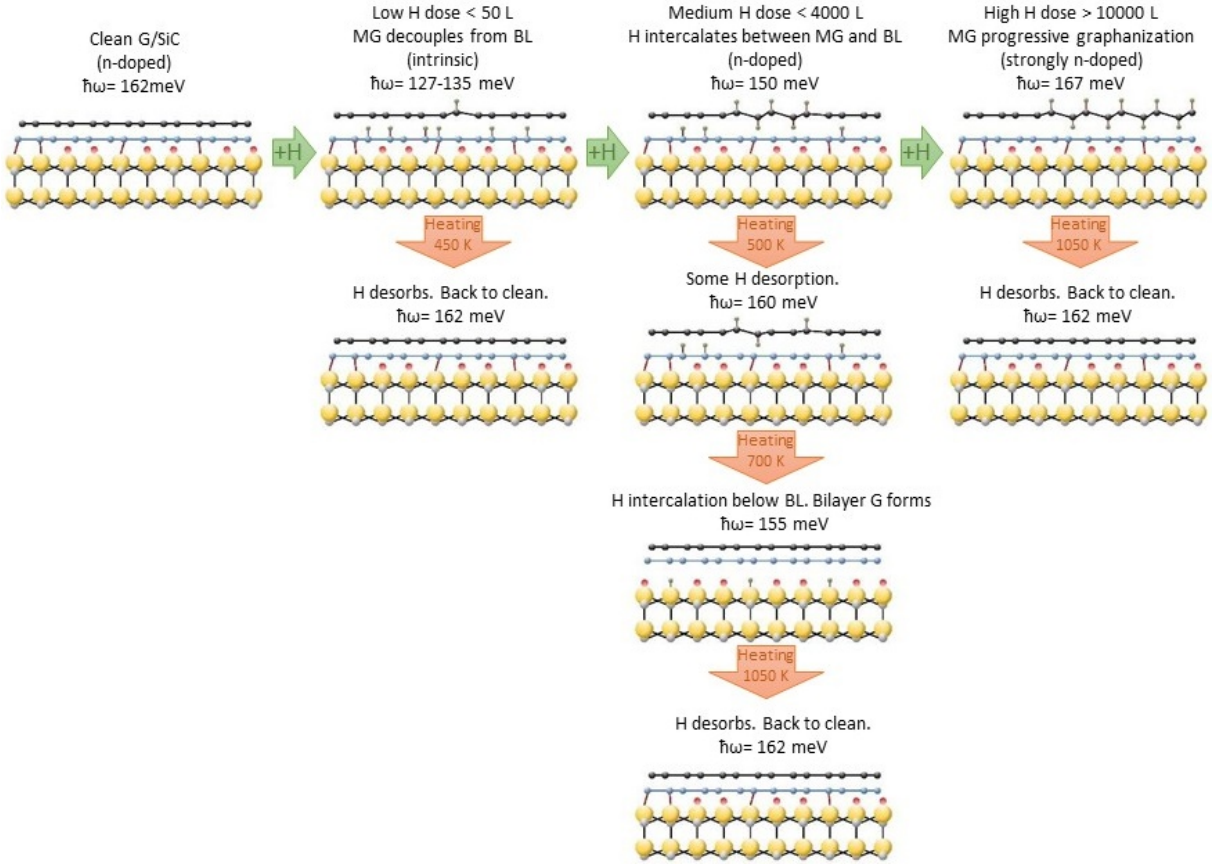


Figure 8.10 – Scheme of the coverage and temperature evolution. The buffer layer (also addressed as zero layer) is drawn as a corrugated grey line with about 30% of Si-C bonds (outermost Si atoms are drawn as blue circles). Graphene is represented as a black line.

The bare surface consists of a buffer layer (also addressed as zero layer) with a significant amount of Si C bonds and of an outer graphene layer, which is intrinsically n doped [213,214]

Upon a short exposure to H (or D) at RT and below, some H decorates the buffer layer or sits above the MG, yielding the weak CH loss around 345 meV. Despite the relatively low amount,

the plasmaron frequency $\omega_+$ is significantly red shifted implying a relatively high sticking probability. According to literature, intercalation below the buffer layer is inhibited at this temperature. Adsorption above MG is consistent with a previous STM investigation showing H decoration for a very low exposure to atomic H [215]. This situation is, however, not compatible with the large red shift we observe for $\omega_+$. Indeed if H were adsorbed mainly at the outermost layer, the latter should become significantly n doped [216] and the frequency of the plasmaron should increase [217], contrary to the present experimental evidence. We have thus to conclude that enough H intercalates between MG and BL to detach the MG layer which becomes nearly free standing and thus less n doped. Since the intrinsic n doping of the bare surface is now compensated, the frequency of graphene plasmon (and thus $\omega_+$) decreases.

Our HREELS data do not allow to separate the relative amount of H attached to the outer layer and to the buffer layer. It is, however, evident that the latter must be large enough to decouple the graphene layer from the buffer layer already at 40 L exposure as well as to compensate for the n doping due to the H adsorbed on the MG. The observed broad energy loss at the H/D stretch regions results therefore most probably both from intercalated and screened as well as adsorbed H/D.

From the thermodynamic point of view, adsorption on the buffer layer is energetically more convenient than adsorption on the upper graphene layer [218]. The buffer layer is indeed def initely more reactive than a single layer graphene sheet: theory predicts even a site for which the adsorption energy is higher than the dissociation energy of $H_2$, thus allowing for its exo thermic dissociation.

Once the so obtained hydrogenated layer is annealed to 450 K, H desorbs. This result is in reasonable agreement with TPD of H adsorbed on graphite [219] and with data thermal de composition of graphone [13]. This explains why no shift of the plasmaron takes place when H or D is dosed on the bare surface above 325 K (see experiment reported in Figure 8.8).

If a larger H exposure is performed, more and more H accumulates between the buffer layer and MG. Above some critical coverage, local graphanization of the outer layer sets in, giving rise to an intense CH loss at 360 meV. Such energy loss is indicative of the presence of H on both sides of the layer [193,209].

The hydrogenation energy has been calculated for G/Ni(111) by DFT: the hydrogenation energy increases with increasing H coverage being 2.11 eV/atom for graphone and 2.50 eV/atom for graphane [13]. When the local coverage becomes high enough, graphanization of the outer layer becomes thus energetically favored with respect to further hydrogenation of the buffer layer. The process of graphanization must however be incomplete even at the largest exposure performed in the present experiment since otherwise a quenching of the plasmaron loss would be expected [198].

When annealing the layer obtained after 4000 L several processes may take place. At 450 K decomposition of graphanized patches sets in causing a large and abrupt decrease of the in tensity of the CH stretch in accord with [220]. The plasmaron frequency $\omega_+$ increases then by some 5 10 meV, corresponding to an increased n doping of the MG layer. Upon reaching 700 K, H intercalation below the buffer layer is activated [221]. The decrease in H coverage in the outermost layers is witnessed by the decrease and subsequent vanishing of the residual CH stretch intensity. Intercalation and H bonding to the Si atoms below the BL implies the detachment of the latter and the formation of a detached graphene bilayer. Under such conditions we observe a plasmaron energy loss of 155 meV, in accord with the previous investigation by Koch et al. [208].
Finally, above 1050 K H starts to de intercalate[7], the buffer layer binds back again to Si and the system moves back to the pristine original condition. $\omega_+$ moves then back to its original level, rising by some 5 meV [208].

In our experiments at high exposure H turns out to me more efficient than D: an isotope effect is thus present in the graphanization process. This result is at variance with the work of Paris et al.[222] for graphanization of (quasi) free standing G deposited on Au intercalated Ni(111), for which D is found to be more efficient than H. The mechanism proposed by these authors is that H initially physisorbs at the graphene and then tunnels into the chemisorption configuration. The latter process is in competition with desorption off the physisorbed state, which is more efficient for H adatoms because of the lower zero point energy of D thus causing an inverse isotope effect.

Our observation of a more effective graphanization while using H instead of D indicates that, for our system, the limiting step is the diffusion of H/D under or above the MG layer, a process which we expect to be more efficient for the lighter isotope. This observation implies that for graphene on SiC the chemisorption barrier is different from the one of H on graphene on Au/Ni studied by Paris et al. (e.g. because of a different doping of the graphenic layer). An isotope effect with the correct sign is reported also for the hydrogenation of organic molecules (see. e.g. Goumans et al. [223]). The isotope effect could, however, be associated with the intercalation process through the MG layer, whereby H is more mobile. Indeed, all initial data points of the $\omega_+$ vs H exposure indicate consistently a slight but higher efficiency for H (see Figure 8.2).

There remains to explain why and how hydrogen (or deuterium) reaches the BL and chemisorbs there instead of remaining at the outer graphene side. The buffer layer, being partially bonded with the underlying Si atoms, is more reactive than the flat graphene layer above it, so that adsorption of H on the partially corrugated buffer layer might be favored. However, it is necessary to explain how H can pass through the graphene cap.

Since the diffusivity for H(D) atoms on G/SiC(0001) is not very high (D=0.37 Å/s [224]) and is only activated above room temperature, we can exclude that the H(D) atoms can diffuse on the surface to intercalate through defects. According to [225] the barrier to move a H atom through free standing graphene is 2.55 eV so that also this route is not possible.

## 8.5 Kinetic model

To attempt a semi quantitative description of the processes taking place during H adsorption we developed a kinetic model.

Let $\theta_{bl}$, $\theta_1$ e $\theta_{1sub}$ be the coverage of H in the buffer (otherwise called zero) layer, in the outer graphene layer and on the backside of the outer layer respectively.

There are several possible processes which can occur with a given probability

a) Sticking of impinging H on the outer layer: $H_g \rightarrow H_{ad1}$, which occurs with probability $P=s_0(1\ \theta_1)$.
b) The term $(1\ \theta_1)$ prevents adsorption on an already occupied site.
c) $H_g + H_{ad1} \rightarrow H_{ad1} + H_{adbl}$ (which occurs with probability $p_1*(1\ \theta_{bl})$ )
d) $H_g + H_{ad1} \rightarrow 2\ H_{adbl}$
e) This process occurs with probability $p_2*(1\ \theta_{bl})$. The term $(1\ \theta_{bl})$ guarantees that the coverage of the buffer layer cannot increase above 1 ML.
f) Desorption of molecular hydrogen when H hits a pre adsorbed H on the outer layer:
g) $H_g + H_{ad} \rightarrow H_{2g}$ (This process occurs with probability $(1\ \ p_2*(1\ \theta_{bl})\ \ p_1*(1\ \theta_0))$
h) Graphanization of the outer layer by removal of one H from the buffer layer $H_{adbl} \rightarrow H_{sub1}$ . This process occurs with probability $p_{graf}*\theta_{bl}*(1\ \theta_{1sub})$. This term accounts for the fact that the coverage on the backside of the outer layer cannot exceed 1 ML and that the process requires to have H on the buffer layer.

The picture below shows the result of a simulation with $s_0=0.03$, $p_1=0.9$, $p_2=0.1$ and $p_{graf}=10^{-4}$.

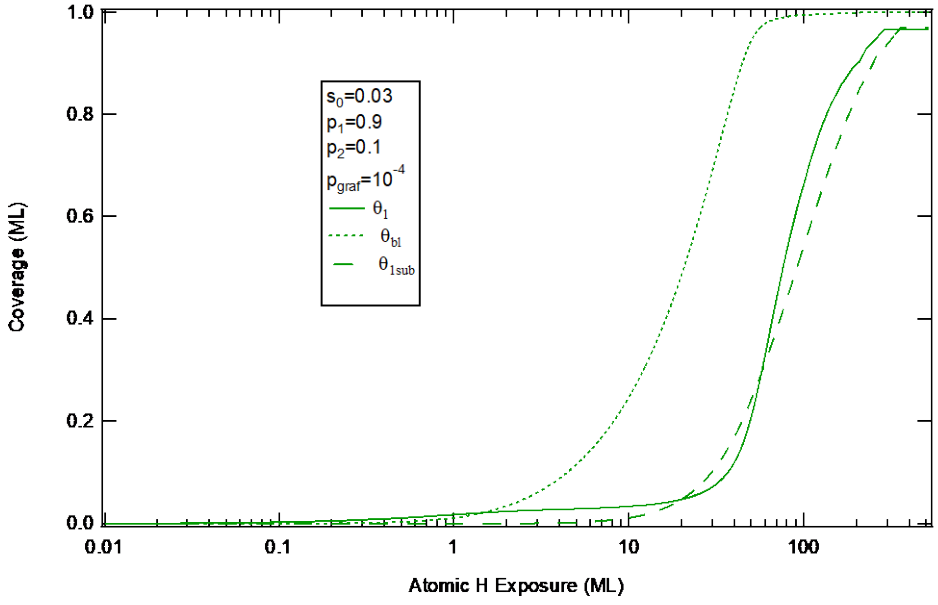


Figure 8.11- Simulated H coverage behaviour as function of exposure

This model can *qualitatively* account for the observed experimental trends provided that:

The sticking probability at a bare site is lower than the probability that when one H hits close to a pre adsorbed H on the outer layer both H atoms are sent to the buffer layer. In the opposite case the coverage of H at the upper layer would be larger than the coverage of H on the buffer layer.

The probability $p_{graf}$ for one H adsorbed onto the buffer layer to graphanize the upper layer adsorbing in the subsurface site of the outer layer is low. In the opposite case the intensity due to CH at the graphane like frequency should appear at significantly lower exposure.

The intensity of the stretch due to H adsorbed on the outer layer and/or on the buffer layer is quite low so that it is hardly detectable in the initial part of the experiment. Despite that, a significant amount of H adsorbs on the buffer layer to justify the drop of the plasmaron frequency already at relatively low exposures.

## 8.6 Conclusions

In conclusion, based on the shift of the plasmaron energy, we have shown that when graphene grown on SiC is dosed with H atoms below 450 K the latter intercalate below graphene detaching it form the buffer layer below. H is unable to pass also through the buffer layer, except when the system is annealed at 450 K. A detached bilayer of graphene forms then which is stable up to some 700 K. Our results are consistent with literature data and imply the possibility for the H atoms to move through the graphene layer already at low temperatures. Theoretical investigation of the possible mechanisms are currently under way.

# 9 Conclusions

In my PhD Thesis I have investigated experimentally under controlled UHV conditions the chemical reactivity of single layer graphene with carbon monoxide and atomic hydrogen. In particular, I have considered the influence of the metallic substrate, the effect of N doping, the role of vacancies and the effect of the presence of both graphene and boron nitride patches on the reactivity with CO. In the final part I have devoted my attention to the reactivity of graphene on SiC with atomic hydrogen, a system relevant in itself ad a sample model for covalent functionalisation.

The main original, and to large extent unexpected, results can be summarised as follows.

a) The reactivity of pristine single layer graphene with CO depends strongly on the chemical nature of the substrate: indeed, adsorption of CO occurs with an initial heat of adsorption of 0.58 eV/molecule in the low coverage limit and of 0.35 eV/molecule at 1/3 ML coverage when graphene is supported on Ni(111), while no signature of CO adsorption is observed under UHV conditions even at 80 K when graphene is supported on a Cu foil. The values of the vibrational frequencies for the molecule surface stretch and for the CO stretch are indicative of weak molecular chemisorption and indicate adsorption at on top sites. This result is relevant also under non UHV conditions, since such relatively high values of the adsorption energy allow for an equilibrium coverage close to 0.1 ML under a pressure of 10 mbar around RT[17]. Comparison of the reactivity of G on Ni(111) grown with different protocols leads to the conclusion that the top fcc phase is the most reactive one among the top fcc, top bridge and top hcp phases[18]. The values of the heat of adsorption are larger than theoretically predicted and stimulated theorists to consider more carefully the role of the support in the graphene CO Interaction[125].

c) When doping graphene on Ni(111) with N atoms by 100 eV $N_2$ ion bombardment rela tively high doping levels can be attained: on this layer a further, more strongly bound and doubly coordinated CO species has been observed by High Resolution Energy Loss Spectroscopy. The reactive site is most likely close to pyridinic or to a pyrrolic N site and enables and adsorption energy larger by about 50 % with respect to the one of a pristine (i.e. non doped) G site for G/Ni(111) [19].

d) The presence of single and/or double vacancies enables CO intercalation under UHV conditions and at Room Temperature in between the graphene layer and the Ni(111) substrate. No signature of stable CO intercalation/adsorption is observed for graphene supported on a Cu foil under UHV, even at 80 K.
This result is explained by the fact that in presence of a metallic substrate, the bonds at the vacancy back bonds to the metallic substrate (Ni or Cu), so that the vacancy itself is not reactive. The large amount of theoretical calculations addressing the reactivity of vacancies of non supported graphene are thus not adequate to describe the real behaviour of graphene supported onto a metal substrate [20].

As demonstrated recently, when graphene is supported on silica, vacancies are on the contrary reactive because back bonding does not occur in such case [133]. Intercalation through the vacancy can occur if the substrate is reactive enough, thus explaining the observation of adsorbed CO for ion bombarded G on Ni(111) but not for G on polycrystalline Cu.

Intercalated CO molecules can react leading to the formation of desorbing $CO_2$ and C, thus providing evidence for a Boudouard reaction catalysed by the NI(111) substrate under a G cover[61]. The residual C atoms are eventually used to mend the vacancy in the graphene layer, so that after a few cycles the surface is no longer reactive with CO at RT. This result suggests the possibility to repair the graphene layer by taking advantage of reaction occurring between it and the reactive substrate.

e) In order to investigate the role of co doping and of the presence of domains we have also exposed to CO a mixed graphene and Boron nitride layer, grown on Pt(111) in the frame of a collaboration with Bondino et al [21]. Preliminary results indicate that the layer presenting N and B sites is reactive with CO while graphene on Pt(111) is inert even at liquid nitogen temperature. This result can be rationalised considering that G interacts weakly with the underlying Pt(111) substrate so that adsorption of CO can occur only thanks to doping.

f) Finally, we explored the possibility of covalent functionalisation of G on SiC. Even if extensive theoretical calculations are being performed to unravel the adsorption mechanism, I have convincing evidence that adsorption occurs mostly on top of the buffer layer and not on the outer layer, thus removing the intrinsic doping of such G layer. At significantly larger exposures, graphanization of the external G sheet sets. This result is surprising because indicates a preference for H adsorption on the buffer layer (and not on the outer G layer) even at RT. The results seem to arise from the higher reactivity of the corrugated graphene of the buffer layer with respect to the free standing outer layer, indicating again the importance of the support in the chemistry of graphene.

# Appendix A) Estimate of adsorption energy from HREEL spectra

In order to *measure* rigorously the isosteric heat of adsorption one should record the coverage (Θ) at given equilibrium pressure and temperature and then use the Clausius Clapyeron equation. Alternatively, the same information can be retrieved by performing microcalorimetric measurements.

It is however possible to *estimate* the *molar* adsorption energy (*Edes*) of adsorbed CO from the experimental desorption temperature Tdes if a value for the pre factor for desorption (ν) is known.

The rate of uni molecular desorption at temperature T is indeed given by:

$$\frac{d\Theta}{dt} = -\nu\Theta e^{-\frac{E_{des}(\Theta)}{RT}}$$

The lifetime τ of the molecule at temperature T and at coverage Θ is defined as:

$$t(T,\Theta) = \frac{e^{\frac{E_{des}(\Theta)}{RT}}}{\nu}$$

From this, it follows that:

$$E_{des} = RT\ln(\tau\nu)$$

For the adsorption energy per molecule ($E_{des}$) one should divide $E_{des}$ by the Avogadro number, obtaining:

$$E_{des} = K_B T\ln(\tau\nu)$$

In our HREELS experiments we observed that the initial ν(CO) intensity is unaffected by flashing the sample to 125 K and decreases eventually after a flash to 150 K. Since annealing is performed manually, we can estimate say that the sample remained at the maximum annealing temperature for a time Δt~1 s before being rapidly cooled down again. The fact the ν(CO) intensity in Figure 4.8 remains unperturbed after flashing to $T_1$ =125 K implies then that the lifetime of the molecule at $T_1$ is larger than Δt; similarly the decrease of the HREEL feature after flashing to $T_2$= 150 K indicates that τ< Δt at temperature $T_2$. We can thus safely deduce that the molecules have a lifetime τ=Δt~1 s at a temperature $T_{des}$ such that $T_1<T_{des}<T_2$.

If we now *assume* that ν=$10^{13}$ Hz, a value frequently assumed for the rate of desorption [87], $E_{des}$ can be *estimated* from the coverage at which the decrease in the HREEL signal is observed.

In this operation we set $T_{des}$=1/2($T_1$+$T_2$=137.5 K for the desorption at 1/3 ML coverage (measured with respect to the Ni substrate) and $T_{des}$=225 K in the low coverage limit. The uncertainty on $T_{des}$ causes a relative error on $E_{des}$ lower than ~10 %. We are well aware that quite different pre

factors for desorption have been suggested, e.g. $\nu$=3 $10^{15}$ Hz for CO on Ni [88] and values as high as $10^{18}$ Hz for other systems [89].

However, if we assume $\nu$=$10^{15}$ Hz or $\nu$=$10^{17}$ Hz (instead of $10^{13}$ Hz), the estimated values for $E_{des}$ at $\Theta$=1/3 ML increase to 0.40 eV/molecule and 0.46 eV/molecule, respectively. So, an even larger binding energy would be obtained. The value $E_{des}$=0.35 eV/molecule given in the manuscript is thus *a conservative lower limit* to the adsorption energy, the exact value of which cannot be retrieved by our experimental means.

In order to assess on a more quantitative basis our estimate of the adsorption energy we have computed numerically the coverage as a function of temperature for three different heating rates (1 K/s, 5 K/s and 10 K/s) and for

a) $E_{des}$=0.35 eV/molecule (corresponding to the estimated heat of desorption at 1/3 ML coverage)
b) $E_{des}$=0.58 eV/molecule (corresponding to the estimated heat of desorption in the low coverage limit)
c) Assuming that $E_{des}$ changes linearly with coverage between such values $E_{des} = E_{des}(0) - a\Theta$ where $a = \frac{E_{des}(0) - E_{des}(0.33\ ML)}{0.33\ ML}$).

The results are reported in Figure 9.1 below, which compares the area of the CO stretch peaks of Figure 4.8 (normalised to the peak area in the spectrum recorded immediately after exposure at 77 K) with the relative change in the coverage obtained with our numerical model, assuming always $\nu$= $10^{13}$ Hz as pre factor).

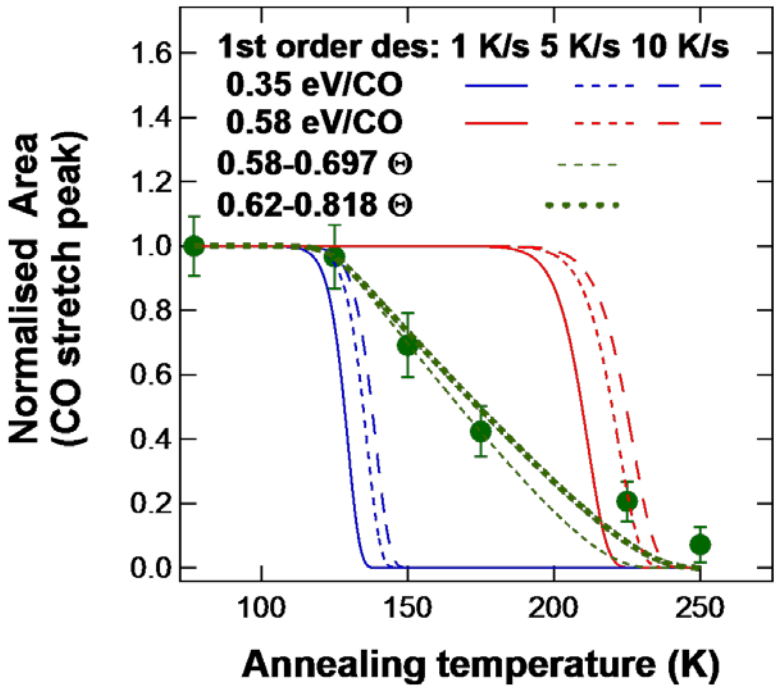


Figure 9.1 – Normalised area of the CO stretch peak (Figure 4.8) vs. annealing temperature (see text for details). The error bar is determined by the error on the fitting parameters of the Gaussian function used to fit the loss spectrum.

It is apparent that:

a) The adsorption energy of 0.35 eV at 0.33 ML (blue curves) is in accord with the fact that the area of the CO stretch peak starts to decrease above 125 K.
b) The desorption energy of 0.58 eV in the low coverage limit (red curves) is needed to account for the residual intensity present after annealing to 225 K.
c) A desorption energy decreasing linearly with coverage between 0.58 eV/molecule and 0.35 eV/molecule (thin green dotted line) is compatible with our experimental data (green points). An even better agreement can be obtained for the slightly larger value $E_{des}(0)$=0.62 eV/molecule while keeping $E_{des}$(0.33 ML)=0.35 eV/molecule (thick green dotted line). A decreasing desorption energy with increasing coverage is reasonable due to the presence of significant repulsive interactions between adsorbed CO molecules.

The average sticking probability in the coverage range $0 \leq \Theta \leq 1/3$ ML is given by the ratio of coverage and exposure and is close to 1 since 1 L of CO corresponds for Ni(111) to a dose of ~0.3 ML CO Ni(111). This indicates the absence of a significant activation barrier for adsorption and, therefore, confirms the correctness of our assumption in identifying $E_{ads}$ with $E_{des}$.

Given the estimated value of $E_{ads}$, the order of magnitude of the equilibrium coverage at a given pressure and temperature can then be calculated using the Langmuir isotherm.

# 10 Bibliography


[1] F. Schedin, A.K. Geim, S. V. Morozov, E.W. Hill, P. Blake, M.I. Katsnelson, K.S. Novoselov, Detection of individual gas molecules adsorbed on graphene, Nat. Mater. 6 (2007) 652–655. doi:10.1038/nmat1967.

[2] T.O. Wehling, K.S. Novoselov, S. V Morozov, E.E. Vdovin, M.I. Katsnelson, a K. Geim, a I. Lichtenstein, Molecular doping of graphene., Nano Lett. 8 (2008) 173–7. doi:10.1021/nl072364w.

[3] L. Liao, H. Peng, Z. Liu, Chemistry Makes Graphene beyond Graphene., J. Am. Chem. Soc. (2014). doi:10.1021/ja5048297.

[4] L. Ferrighi, M. Datteo, C. Di Valentin, Boosting Graphene Reactivity with Oxygen by Boron Doping: Density Functional Theory Modeling of the Reaction Path., J. Phys. Chem. C. 118 (2014) 223–230. doi:10.1021/jp410966r.

[5] L. Qu, Y. Liu, J. B. Baek, L. Dai, Nitrogen doped graphene as efficient metal free electrocatalyst for oxygen reduction in fuel cells., ACS Nano. 4 (2010) 1321–6. doi:10.1021/nn901850u.

[6] S. Guo, S. Zhang, S. Sun, Tuning nanoparticle catalysis for the oxygen reduction reaction, Angew. Chemie Int. Ed. 52 (2013) 8526–8544. doi:10.1002/anie.201207186.

[7] C. Riedl, C. Coletti, T. Iwasaki, A.A. Zakharov, U. Starke, Quasi free standing epitaxial graphene on SiC obtained by hydrogen intercalation, Phys. Rev. Lett. 103 (2009) 1–4. doi:10.1103/PhysRevLett.103.246804.

[8] Q. Wu, Y. Wu, Y. Hao, J. Geng, M. Charlton, S. Chen, Y. Ren, H. Ji, H. Li, D.W. Boukhvalov, R.D. Piner, C.W. Bielawski, R.S. Ruoff, Selective surface functionalization at regions of high local curvature in graphene, Chem. Commun. 49 (2013) 677–679. doi:10.1039/c2cc36747e.

[9] Q.H. Wang, Z. Jin, K.K. Kim, A.J. Hilmer, G.L.C. Paulus, C. J. Shih, M. H. Ham, J.D. Sanchez Yamagishi, K. Watanabe, T. Taniguchi, J. Kong, P. Jarillo Herrero, M.S. Strano, Understanding and controlling the substrate effect on graphene electron transfer chemistry via reactivity imprint lithography, Nat. Chem. 4 (2012) 724–732. doi:10.1038/nchem.1421.

[10] L. Ferrighi, C. Di Valentin, Oxygen reactivity on pure and B doped graphene over crystalline Cu(111). Effects of the dopant and of the metal support, Surf. Sci. 634 (2015) 68–75. doi:10.1016/j.susc.2014.11.001.

[11] Z. Ao, J. Yang, S. Li, Q. Jiang, Enhancement of CO detection in Al doped graphene, Chem. Phys. Lett. 461 (2008) 276–279. doi:10.1016/j.cplett.2008.07.039.

[12] C. Morchutt, J. Björk, S. Krotzky, R. Gutzler, K. Kern, Covalent coupling via dehalogenation on Ni(111) supported boron nitride and graphene, Chem. Commun. 51 (2015) 2440–2443. doi:10.1039/C4CC07107G.

[13] W. Zhao, J. Gebhardt, F. Späth, K. Gotterbarm, C. Gleichweit, H. Steinrück, A. Görling, C. Papp, Reversible Hydrogenation of Graphene on Ni(111) Synthesis of “Graphone,” Chem. A Eur. J. 21 (2015) 3347–3358. doi:10.1002/chem.201404938.

[14] X. Feng, S. Maier, M. Salmeron, Water splits epitaxial graphene and intercalates, J. Am. Chem. Soc. 134 (2012) 5662–5668. doi:10.1021/ja3003809.

[15] L.L. Patera, C. Africh, R.S. Weatherup, R. Blume, S. Bhardwaj, C. Castellarin Cudia, A. Knop Gericke, R. Schloegl, G. Comelli, S. Hofmann, C. Cepek, In situ observations of the atomistic mechanisms of Ni catalyzed low temperature graphene growth., ACS Nano. 7 (2013) 7901–12. doi:10.1021/nn402927q.

[16] R.J. Koch, M. Weser, W. Zhao, F. Viñes, K. Gotterbarm, S.M. Kozlov, O. Höfert, M. Ostler, C. Papp, J. Gebhardt, H. P.P. Steinrück, A. Görling, T. Seyller, Growth and electronic structure of nitrogen doped graphene on Ni(111), Phys. Rev. B. 86 (2012) 75401. doi:10.1103/PhysRevB.86.075401.

[17] M. Smerieri, E. Celasco, G. Carraro, A. Lusuan, J. Pal, G. Bracco, M. Rocca, L. Savio, L. Vattuone, Enhanced Chemical Reactivity of Pristine Graphene Interacting Strongly with a Substrate: Chemisorbed Carbon Monoxide on Graphene/Nickel(1 1 1), ChemCatChem. 7 (2015) 2328–2331. doi:10.1002/cctc.201500279.

[18] E. Celasco, G. Carraro, M. Smerieri, L. Savio, M. Rocca, L. Vattuone, Influence of growing conditions on the reactivity of Ni supported graphene towards CO, J. Chem. Phys. 146 (2017) 104704. doi:10.1063/1.4978234.

[19] G. Carraro, E. Celasco, M. Smerieri, L. Savio, G. Bracco, M. Rocca, L. Vattuone, Chemisorption of CO on N doped graphene on Ni(111), Appl. Surf. Sci. 428 (2018) 775–780. doi:10.1016/j.apsusc.2017.09.194.

[20] E. Celasco, G. Carraro, A. Lusuan, M. Smerieri, J. Pal, M. Rocca, L. Savio, L. Vattuone, CO chemisorption at vacancies of supported graphene films: a candidate for a sensor?, Phys. Chem. Chem. Phys. 18 (2016) 18692–18696. doi:10.1039/C6CP02999J.

[21] S. Nappini, I. Píš, G. Carraro, E. Celasco, M. Smerieri, L. Savio, E. Magnano, F. Bondino, On surface synthesis of different boron–nitrogen–carbon heterostructures from dimethylamine borane, Carbon N. Y. 120 (2017) 185–193. doi:10.1016/j.carbon.2017.05.026.

[22] G.N. Dash, S.R. Pattanaik, S. Behera, Graphene for electron devices: The panorama of a decade, IEEE J. Electron Devices Soc. 2 (2014) 77–104. doi:10.1109/JEDS.2014.2328032.

[23] K.S. Novoselov, a K. Geim, S. V Morozov, D. Jiang, M.I. Katsnelson, I. V Grigorieva, S. V Dubonos, a a Firsov, Two dimensional gas of massless Dirac fermions in graphene., Nature. 438 (2005) 197–200. doi:10.1038/nature04233.

[24] A. Dahal, M. Batzill, Graphene–nickel interfaces: a review, Nanoscale. 6 (2014) 2548. doi:10.1039/c3nr05279f.

[25] N. Liu, L. Fu, B. Dai, K. Yan, X. Liu, R. Zhao, Y. Zhang, Z. Liu, Universal segregation growth approach to wafer size graphene from non noble metals, Nano Lett. 11 (2011) 297–303. doi:10.1021/nl103962a.

[26] A. Jorio, Raman Spectroscopy in Graphene Based Systems: Prototypes for Nanoscience and Nanometrology, ISRN Nanotechnol. 2012 (2012) 1–16. doi:10.5402/2012/234216.

[27] J. Lahiri, T. Miller, L. Adamska, I.I. Oleynik, M. Batzill, Graphene growth on Ni(111) by transformation of a surface carbide., Nano Lett. 11 (2011) 518–22. doi:10.1021/nl103383b.

[28] P. Jacobson, B. Stöger, A. Garhofer, G.S. Parkinson, M. Schmid, R. Caudillo, F. Mittendorfer, J. Redinger, U. Diebold, Nickel carbide as a source of grain rotation in epitaxial graphene., ACS Nano. 6 (2012) 3564–72. doi:10.1021/nn300625y.

[29] Z. Zou, L. Fu, X. Song, Y. Zhang, Z. Liu, Carbide forming groups IVB VIB metals: A new territory in the periodic table for CVD growth of graphene, Nano Lett. 14 (2014) 3832–3839. doi:10.1021/nl500994m.

[30] A. Dahal, M. Batzill, Graphene nickel interfaces: a review., Nanoscale. 6 (2014) 2548–62. doi:10.1039/c3nr05279f.

[31] Y. Dedkov, E. Voloshina, Graphene growth and properties on metal substrates, J. Phys. Condens. Matter. 27 (2015). doi:10.1088/0953 8984/27/30/303002.

[32] C. Riedl, C. Coletti, U. Starke, Structural and electronic properties of epitaxial graphene on SiC(0001): a review of growth, characterization, transfer doping and hydrogen intercalation, J. Phys. D. Appl. Phys. 43 (2010) 374009. doi:10.1088/0022 3727/43/37/374009.

[33] C. Virojanadara, M. Syväjarvi, R. Yakimova, L.I. Johansson, A.A. Zakharov, T. Balasubramanian, Homogeneous large area graphene layer growth on 6H SiC(0001), Phys. Rev. B. 78 (2008) 245403. doi:10.1103/PhysRevB.78.245403.

[34] J. Kunc, M. Rejhon, E. Belas, V. Dědič, P. Moravec, J. Franc, Effect of Residual Gas Composition on Epitaxial Growth of Graphene on SiC, Phys. Rev. Appl. 8 (2017) 44011. doi:10.1103/PhysRevApplied.8.044011.

[35] A. Al Temimy, C. Riedl, U. Starke, Low temperature growth of epitaxial graphene on SiC induced by carbon evaporation, Appl. Phys. Lett. 95 (2009). doi:10.1063/1.3265916.

[36] I. Gierz, C. Riedl, U. Starke, C.R. Ast, K. Kern, Atomic hole doping of graphene, Nano Lett. 8 (2008) 4603–4607. doi:10.1021/nl802996s.

[37] U. Starke, Bandstructure Manipulation of Epitaxial Graphene on SiC(0001) by Molecular Doping and Hydrogen Intercalation, MRS Proc. 1246 (2010) 1–12. doi:10.1557/PROC 1246 B10 01.

[38] S. Barja, M. Garnica, J.J. Hinarejos, A.L. Vázquez de Parga, N. Martín, R. Miranda, Self organization of electron acceptor molecules on graphene., Chem. Commun. (Camb). 46 (2010) 8198–200. doi:10.1039/c0cc02675a.

[39] K.S. Kim, A.L. Walter, L. Moreschini, T. Seyller, K. Horn, E. Rotenberg, A. Bostwick, Coexisting massive and massless Dirac fermions in symmetry broken bilayer graphene, Nat. Mater. 12 (2013) 887–892. doi:10.1038/nmat3717.

[40] O. Leenaerts, B. Partoens, F.M. Peeters, Adsorption of H2O, NH3, CO, NO2, and NO on graphene: A first principles study, Phys. Rev. B. 77 (2008) 125416. doi:10.1103/PhysRevB.77.125416.

[41] Y. Dan, Y. Lu, N.J. Kybert, Z. Luo, A.T.C. Johnson, Intrinsic Response of Graphene Vapor Sensors, Nano Lett. 9 (2009) 1472–1475. doi:10.1021/nl8033637.

[42] J. Dai, J. Yuan, P. Giannozzi, Gas adsorption on graphene doped with B, N, Al, and S: A theoretical study, Appl. Phys. Lett. 95 (2009) 232105. doi:10.1063/1.3272008.

[43] Y. H. Zhang, Y. Chen, K. G. Zhou, C. Liu, J. Zeng, H. Zhang, Y. Peng, Improving gas sensing properties of graphene by introducing dopants and defects: a first principles study, Nanotechnology. 20 (2009) 185504. doi:10.1088/0957 4484/20/18/185504.

[44] B. Wang, S.T. Pantelides, Controllable healing of defects and nitrogen doping of graphene by CO and NO molecules, Phys. Rev. B. 83 (2011) 245403. doi:10.1103/PhysRevB.83.245403.

[45] A.A. Peyghan, M. Noei, M.B. Tabar, A large gap opening of graphene induced by the adsorption of CO on the Al doped site., J. Mol. Model. 19 (2013) 3007–14. doi:10.1007/s00894 013 1832 x.

[46] J. Dai, J. Yuan, Adsorption of molecular oxygen on doped graphene: atomic, electronic and magnetic properties, Adsorpt. J. Int. Adsorpt. Soc. (2009) 1–8. doi:10.1103/PhysRevB.81.165414.

[47] B. Sanyal, O. Eriksson, U. Jansson, H. Grennberg, Molecular adsorption in graphene with divacancy defects, Phys. Rev. B. 79 (2009) 113409. doi:10.1103/PhysRevB.79.113409.

[48] L. Tsetseris, S.T. Pantelides, Adsorbate Induced Defect Formation and Annihilation on Graphene and Single Walled Carbon Nanotubes Adsorbate Induced Defect Formation and Annihilation on Graphene and Single Walled, Society. (2009) 941–944. doi:10.1021/jp809228p.

[49] A.T.S. Wee, W. Chen, Molecular interactions on epitaxial graphene, Phys. Scr. T146 (2012) 14007. doi:10.1088/0031 8949/2012/T146/014007.

[50] T. Ohta, A. Bostwick, T. Seyller, K. Horn, E. Rotenberg, Controlling the electronic structure of bilayer graphene, Science (80 . ). 313 (2006) 951–954. doi:10.1126/science.1130681.

[51] S.Y. Zhou, D.A. Siegel, A. V. Fedorov, A. Lanzara, Metal to insulator transition in epitaxial graphene induced by molecular doping, Phys. Rev. Lett. 101 (2008). doi:10.1103/PhysRevLett.101.086402.

[52] R. Balog, B. Jørgensen, L. Nilsson, M. Andersen, E. Rienks, M. Bianchi, M. Fanetti, E. Lægsgaard, A. Baraldi, S. Lizzit, Z. Sljivancanin, F. Besenbacher, B. Hammer, T.G. Pedersen, P. Hofmann, L. Hornekær, Bandgap opening in graphene induced by patterned hydrogen adsorption, Nat. Mater. 9 (2010) 315–319. doi:10.1038/nmat2710.

[53] F. Yavari, C. Kritzinger, C. Gaire, L. Song, H. Gulapalli, T. Borca Tasciuc, P.M. Ajayan, N. Koratkar, Tunable bandgap in graphene by the controlled adsorption of water molecules, Small. 6 (2010) 2535–2538. doi:10.1002/smll.201001384.

[54] E.J. Duplock, M. Scheffler, P.J.D. Lindan, Hallmark of perfect graphene, Phys. Rev. Lett. 92 (2004). doi:10.1103/PhysRevLett.92.225502.

[55] A. Chakradhar, N. Sivapragasam, M.T. Nayakasinghe, U. Burghaus, Support effects in the adsorption of water on CVD graphene: an ultra high vacuum adsorption study, Chem. Commun. 51 (2015) 11463–11466. doi:10.1039/C5CC03827H.

[56] a Chakradhar, U. Burghaus, Adsorption of water on graphene/Ru(0001) an experimental ultra high vacuum study., Chem. Commun. (Camb). 50 (2014) 7698–701. doi:10.1039/c4cc02762k.

[57] D. Guo, R. Shibuya, C. Akiba, S. Saji, T. Kondo, J. Nakamura, Active sites of nitrogen doped carbon materials for oxygen reduction reaction clarified using model catalysts, Science (80 . ). 351 (2016) 361–365. doi:10.1126/science.aad0832.

[58] R. Mu, Q. Fu, L. Jin, L. Yu, G. Fang, D. Tan, X. Bao, Visualizing Chemical Reactions Confined under Graphene, Angew. Chemie Int. Ed. 51 (2012) 4856–4859. doi:10.1002/anie.201200413.

[59] H. Li, J. Xiao, Q. Fu, X. Bao, Confined catalysis under two dimensional materials, Proc. Natl. Acad. Sci. 114 (2017) 5930–5934. doi:10.1073/pnas.1701280114.

[60] Y. Yao, Q. Fu, Y.Y. Zhang, X. Weng, H. Li, M. Chen, L. Jin, A. Dong, R. Mu, P. Jiang, L. Liu, H. Bluhm, Z. Liu, S.B. Zhang, X. Bao, Graphene cover promoted metal catalyzed reactions, Proc. Natl. Acad. Sci. 111 (2014) 17023–17028. doi:10.1073/pnas.1416368111.

[61] Q. Fu, X. Bao, Surface chemistry and catalysis confined under two dimensional materials, Chem. Soc. Rev. 46 (2017) 1842–1874. doi:10.1039/C6CS00424E.

[62] F.C. Henn, A simple means for reproducibly dosing low vapor pressure and/or reactive gases to surfaces in ultrahigh vacuum, J. Vac. Sci. Technol. A Vacuum, Surfaces, Film. 9 (1991) 10. doi:10.1116/1.577108.

[63] H. Ibach, D.L. Mills, Electron Energy Loss Spectroscopy and Surface Vibrations, in: Electron Energy Loss Spectrosc. Surf. Vib., Elsevier, 1982: pp. 363–366. doi:10.1016/B978 0 12 369350 1.50015 4.

[64] W. Ho, R.F. Willis, E.W. Plummer, Observation of Nondipole Electron Impact Vibrational Excitations: H on W (100), Phys. Rev. Lett. 40 (1978) 1463–1466. doi:10.1103/PhysRevLett.40.1463.

[65] J.. Liu, F.. Xie, Q.. Zhang, K.. Wu, X.. Ma, E.. Wang, W.. Liu, Investigations of Fuch–Kliewer phonons and hydrogen adsorption of 6H–SiC surfaces by high resolution electron energy loss spectroscopy, Thin Solid Films. 375 (2000) 77–81. doi:10.1016/S0040 6090(00)01265 7.

[66] P. Soukiassian, E. Wimmer, E. Celasco, C. Giallombardo, S. Bonanni, L. Vattuone, L. Savio, A. Tejeda, M. Silly, M. D'angelo, F. Sirotti, M. Rocca, Hydrogen induced nanotunnel opening within semiconductor subsurface., Nat. Commun. 4 (2013) 2800. doi:10.1038/ncomms3800.

[67] W. Zhao, S.M. Kozlov, O. Höfert, K. Gotterbarm, M.P.A. Lorenz, F. Viñes, C. Papp, A. Görling, H. P. Steinrück, Graphene on Ni(111): Coexistence of Different Surface Structures, J. Phys. Chem. Lett. 2 (2011) 759–764. doi:10.1021/jz200043p.

[68] W. Zhao, J. Gebhardt, K. Gotterbarm, O. Höfert, C. Gleichweit, C. Papp, A. Görling, H. P. Steinrück, Gold intercalation of boron doped graphene on Ni(111): XPS and DFT study, J. Phys. Condens. Matter. 25 (2013) 445002. doi:10.1088/0953 8984/25/44/445002.

[69] R.S. Weatherup, H. Amara, R. Blume, B. Dlubak, B.C. Bayer, M. Diarra, M. Bahri, A. Cabrero Vilatela, S. Caneva, P.R. Kidambi, M. B. Martin, C. Deranlot, P. Seneor, R. Schloegl, F. Ducastelle, C. Bichara, S. Hofmann, Interdependency of Subsurface Carbon Distribution and Graphene–Catalyst Interaction, J. Am. Chem. Soc. 136 (2014) 13698–13708. doi:10.1021/ja505454v.

[70] C.T. Campbell, Ultrathin metal films and particles on oxide surfaces: structural, electronic and chemisorptive properties, 1997. doi:10.1016/S0167 5729(96)00011 8.

[71] M.C. Biesinger, B.P. Payne, L.W.M. Lau, A. Gerson, R.S.C. Smart, X ray photoelectron spectroscopic chemical state quantification of mixed nickel metal, oxide and hydroxide systems, Surf. Interface Anal. 41 (2009) 324–332. doi:10.1002/sia.3026.

[72] R.S. Weatherup, B.C. Bayer, R. Blume, C. Baehtz, P.R. Kidambi, M. Fouquet, C.T. Wirth, R. Schlögl, S. Hofmann, On the Mechanisms of Ni Catalysed Graphene Chemical Vapour Deposition, ChemPhysChem. 13 (2012) 2544–2549. doi:10.1002/cphc.201101020.

[73] F.P. Netzer, T.E. Madey, The structure of CO on Ni(111), J. Chem. Phys. 76 (1982) 710. doi:10.1063/1.442674.

[74] J. Lahiri, M. Batzill, Graphene destruction by metal carbide formation: An approach for patterning of metal supported graphene, Appl. Phys. Lett. 97 (2010) 23102. doi:10.1063/1.3464173.

[75] G. Chiarello, A. Cupolillo, C. Giallombardo, R.G. Agostino, V. Formoso, D. Pacilè, L. Papagno, E. Colavita, Co adsorption of oxygen and carbon monoxide on Ni(1 1 1), Surf. Sci. 536 (2003) 33–44. doi:10.1016/S0039 6028(03)00573 9.

[76] F. Bianchini, L.L. Patera, M. Peressi, C. Africh, G. Comelli, Atomic Scale Identification of Coexisting Graphene Structures on Ni(111), J. Phys. Chem. Lett. 5 (2014) 467–473. doi:10.1021/jz402609d.

[77] D.A. Shirley, High resolution x ray photoemission spectrum of the valence bands of gold, Phys. Rev. B. 5 (1972) 4709–4714. doi:10.1103/PhysRevB.5.4709.

[78] D.E. Parreiras, E.A. Soares, G.J.P. Abreu, T.E.P. Bueno, W.P. Fernandes, V.E. de Carvalho, S.S. Carara, H. Chacham, R. Paniago, Graphene/Ni(111) surface structure probed by low energy electron diffraction, photoelectron diffraction, and first principles calculations, Phys. Rev. B. 90 (2014) 155454. doi:10.1103/PhysRevB.90.155454.

[79] T. Aizawa, R. Souda, Y. Ishizawa, H. Hirano, T. Yamada, K. Tanaka, C. Oshima, Phonon dispersion in monolayer graphite formed on Ni(111) and Ni(001), Surf. Sci. 237 (1990) 194–202. doi:10.1016/0039 6028(90)90531 C.

[80] A. Cupolillo, G. Chiarello, F. Veltri, D. Pacilè, M. Papagno, V. Formoso, E. Colavita, L. Papagno, CO dissociation and CO2 formation catalysed by Na atoms adsorbed on Ni(111), Chem. Phys. Lett. 398 (2004) 118–122. doi:10.1016/j.cplett.2004.09.035.

[81] D. Chakarov, L. Österlund, B. Kasemo, Water adsorption and coadsorption with potassium on graphite (0001), Langmuir. 11 (1995) 1201–1214. doi:10.1021/la00004a028.

[82] D.. Boyd, F.. Hess, G.. Hess, Infrared absorption study of physisorbed carbon monoxide on graphite, Surf. Sci. 519 (2002) 125–138. doi:10.1016/S0039 6028(02)02207 0.

[83] W. Hansen, M. Bertolo, K. Jacobi, Physisorption of CO on Ag(111): investigation of the monolayer and the multilayer through HREELS, ARUPS, and TDS, Surf. Sci. 253 (1991) 1–12. doi:10.1016/0039 6028(91)90576 E.

[84] S.L. Tang, M.B. Lee, Q.Y. Yang, J.D. Beckerle, S.T. Ceyer, Bridge/atop site conversion of CO on Ni(111): Determination of the binding energy difference, J. Chem. Phys. 84 (1986) 1876. doi:10.1063/1.450435.

[85] J. Gebhardt, F. Viñes, A. Görling, Influence of the surface dipole layer and Pauli repulsion on band energies and doping in graphene adsorbed on metal surfaces, Phys. Rev. B Condens. Matter Mater. Phys. 86 (2012) 1–15. doi:10.1103/PhysRevB.86.195431.

[86] H.I. Rasool, C. Ophus, Z. Zhang, M.F. Crommie, B.I. Yakobson, A. Zettl, Conserved Atomic Bonding Sequences and Strain Organization of Graphene Grain Boundaries, Nano Lett. 14 (2014) 7057–7063. doi:10.1021/nl503450r.

[87] K.W. Kolasinski, Surface Science, John Wiley & Sons, Ltd, Chichester, UK, 2012. doi:10.1002/9781119941798.

[88] K. Liao, V. Fiorin, D.S.D. Gunn, S.J. Jenkins, D. a King, Single crystal adsorption calorimetry and density functional theory of CO chemisorption on fcc Co{110}., Phys. Chem. Chem. Phys. 15 (2013) 4059–65. doi:10.1039/c3cp43836h.

[89] C.T. Campbell, L. Árnadóttir, J.R. V. Sellers, Kinetic Prefactors of Reactions on Solid Surfaces, Zeitschrift Für Phys. Chemie. 227 (2013) 1–20. doi:10.1524/zpch.2013.0395.

[90] L. Vattuone, L. Savio, M. Rocca, Bridging the structure gap: Chemistry of nanostructured surfaces at well defined defects, Surf. Sci. Rep. 63 (2008) 101–168. doi:10.1016/j.surfrep.2007.11.001.

[91] Y.Y. Yeo, L. Vattuone, D.A. King, Calorimetric investigation of NO and CO adsorption on Pd{100} and the influence of preadsorbed carbon, J. Chem. Phys. 106 (1997) 1990–1996. doi:10.1063/1.473306.

[92] M. Batzill, The surface science of graphene: Metal interfaces, CVD synthesis, nanoribbons, chemical modifications, and defects, Surf. Sci. Rep. 67 (2012) 83–115. doi:10.1016/j.surfrep.2011.12.001.

[93] a. Varykhalov, J. Sánchez Barriga, a. Shikin, C. Biswas, E. Vescovo, a. Rybkin, D. Marchenko, O. Rader, Electronic and Magnetic Properties of Quasifreestanding Graphene on Ni, Phys. Rev. Lett. 101 (2008) 157601. doi:10.1103/PhysRevLett.101.157601.

[94] A. Zecchina, E.E. Platero, C.O. Areán, Low temperature CO adsorption on alum derived active alumina: An infrared investigation, J. Catal. 107 (1987) 244–247. doi:10.1016/0021 9517(87)90290 9.

[95] K.S. Novoselov, V.I. Fal'ko, L. Colombo, P.R. Gellert, M.G. Schwab, K. Kim, A roadmap for graphene., Nature. 490 (2012) 192–200. doi:10.1038/nature11458.

[96] B.J. Schultz, R. V. Dennis, V. Lee, S. Banerjee, An electronic structure perspective of graphene interfaces, Nanoscale. 6 (2014) 3444. doi:10.1039/c3nr06923k.

[97] X. Wang, X. Li, L. Zhang, Y. Yoon, P.K. Weber, H. Wang, J. Guo, H. Dai, N doping of graphene through electrothermal reactions with ammonia, Science. 324 (2009) 768–771. doi:10.1126/science.1170335.

[98] T.B. Martins, R.H. Miwa, A.J.R. Da Silva, A. Fazzio, Electronic and transport properties of boron doped graphene nanoribbons, Phys. Rev. Lett. 98 (2007). doi:10.1103/PhysRevLett.98.196803.

[99] L. Ci, L. Song, C. Jin, D. Jariwala, D. Wu, Y. Li, A. Srivastava, Z.F. Wang, K. Storr, L. Balicas, F. Liu, P.M. Ajayan, Atomic layers of hybridized boron nitride and graphene domains, Nat. Mater. 9 (2010) 430–435. doi:10.1038/nmat2711.

[100] C. Ma, X. Shao, D. Cao, Nitrogen doped graphene as an excellent candidate for selective gas sensing, Sci. China Chem. 57 (2014) 911–917. doi:10.1007/s11426 014 5066 2.

[101] F. Niu, L. M. Tao, Y. C. Deng, Q. H. Wang, W. G. Song, H. Feng, X.J. Huang, S. Alvarez Garcia, A. de Andres, F. Pariente, E. Lorenzo, X.H. Bao, Phosphorus doped graphene

nanosheets for room temperature NH3 sensing, New J. Chem. 38 (2014) 2269. doi:10.1039/c4nj00162a.

[102] W. Zhao, O. Höfert, K. Gotterbarm, J.F. Zhu, C. Papp, H. P. Steinrück, Production of Nitrogen Doped Graphene by Low Energy Nitrogen Implantation, J. Phys. Chem. C. 116 (2012) 5062–5066. doi:10.1021/jp209927m.

[103] A. Sala, G. Zamborlini, T.O. Menteş, A. Locatelli, Fabrication of 2D Heterojunction in Graphene via Low Energy N 2 + Irradiation, Small. 11 (2015) 5927–5931. doi:10.1002/smll.201501473.

[104] T. Susi, T. Pichler, P. Ayala, X ray photoelectron spectroscopy of graphitic carbon nanomaterials doped with heteroatoms, Beilstein J. Nanotechnol. 6 (2015) 177–192. doi:10.3762/bjnano.6.17.

[105] D. Usachov, O. Vilkov, A. Grüneis, D. Haberer, A. Fedorov, V.K. Adamchuk, a B. Preobrajenski, P. Dudin, A. Barinov, M. Oehzelt, C. Laubschat, D. V Vyalikh, Nitrogen doped graphene: efficient growth, structure, and electronic properties., Nano Lett. 11 (2011) 5401–7. doi:10.1021/nl2031037.

[106] H.M. Jeong, J.W. Lee, W.H. Shin, Y.J. Choi, H.J. Shin, J.K. Kang, J.W. Choi, Nitrogen doped graphene for high performance ultracapacitors and the importance of nitrogen doped sites at basal planes., Nano Lett. 11 (2011) 2472–7. doi:10.1021/nl2009058.

[107] J.J. Yeh, I. Lindau, Atomic subshell photoionization cross sections and asymmetry parameters: $1 \leqslant Z \leqslant 103$, At. Data Nucl. Data Tables. 32 (1985) 1–155. doi:10.1016/0092 640X(85)90016 6.

[108] M. Wei, Q. Fu, Y. Yang, W. Wei, E. Crumlin, H. Bluhm, X. Bao, Modulation of Surface Chemistry of CO on Ni(111) by Surface Graphene and Carbidic Carbon, J. Phys. Chem. C. 119 (2015) 13590–13597. doi:10.1021/acs.jpcc.5b01395.

[109] J.C. Bertolini, B. Tardy, Vibrational EELS studies of CO chemisorption on clean and carbided (111), (100) and (110) nickel surfaces, Surf. Sci. 102 (1981) 131–150. doi:10.1016/0039 6028(81)90312 5.

[110] M. Gajdo, A. Eichler, J. Hafner, CO adsorption on close packed transition and noble metal surfaces: trends from *ab initio* calculations, J. Phys. Condens. Matter. 16 (2004) 1141–1164. doi:10.1088/0953 8984/16/8/001.

[111] K.A. Layman, M.E. Bussell, Infrared spectroscopic investigation of thiophene adsorption on silica supported nickel phosphide catalysts, J. Phys. Chem. B. 108 (2004) 15791–15802. doi:10.1021/jp047882z.

[112] B.F. Machado, P. Serp, Graphene based materials for catalysis, Catal. Sci. Technol. 2 (2012) 54–75. doi:10.1039/C1CY00361E.

[113] S. Sarkar, S. Niyogi, E. Bekyarova, R.C. Haddon, Organometallic chemistry of extended periodic π electron systems: hexahapto chromium complexes of graphene and single walled carbon nanotubes, Chem. Sci. 2 (2011) 1326. doi:10.1039/c0sc00634c.

[114] E. Grånäs, J. Knudsen, U.A. Schröder, T. Gerber, C. Busse, M.A. Arman, K. Schulte, J.N. Andersen, T. Michely, Oxygen Intercalation under Graphene on Ir(111): Energetics, Kinetics, and the Role of Graphene Edges, ACS Nano. 6 (2012) 9951–9963. doi:10.1021/nn303548z.

[115] H. Liu, J.Y. Lee, Electric Field Effects on the Adsorption of CO on a Graphene Nanodot and the Healing Mechanism of a Vacancy in a Graphene Nanodot, J. Phys. Chem. C. 116 (2012) 3034–3041. doi:10.1021/jp210719r.

[116] L. Tapasztó, G. Dobrik, P. Nemes Incze, G. Vertesy, P. Lambin, L.P. Biró, Tuning the electronic structure of graphene by ion irradiation, Phys. Rev. B. 78 (2008) 233407. doi:10.1103/PhysRevB.78.233407.

[117] R. Martinazzo, S. Casolo, G.F. Tantardini, Symmetry induced band gap opening in graphene superlattices, Phys. Rev. B. 81 (2010) 245420. doi:10.1103/PhysRevB.81.245420.

[118] R.K. Joshi, H. Gomez, F. Alvi, A. Kumar, Graphene films and ribbons for sensing of O 2, and 100 ppm of CO and NO 2 in practical conditions, J. Phys. Chem. C. 114 (2010) 6610–6613. doi:10.1021/jp100343d.

[119] E. Kayhan, R.M. Prasad, A. Gurlo, O. Yilmazoglu, J. Engstler, E. Ionescu, S. Yoon, A. Weidenkaff, J.J. Schneider, Synthesis, Characterization, Electronic and Gas Sensing Properties towards H2 and CO of Transparent, Large Area, Low Layer Graphene, Chem. A Eur. J. 18 (2012) 14996–15003. doi:10.1002/chem.201201880.

[120] M.M. Ugeda, I. Brihuega, F. Hiebel, P. Mallet, J. Y. Veuillen, J.M. Gómez Rodríguez, F. Ynduráin, Electronic and structural characterization of divacancies in irradiated graphene, Phys. Rev. B. 85 (2012) 121402. doi:10.1103/PhysRevB.85.121402.

[121] M.M. Ugeda, D. Fernández Torre, I. Brihuega, P. Pou, A.J. Martínez Galera, R. Pérez, J.M. Gómez Rodríguez, Point defects on graphene on metals, Phys. Rev. Lett. 107 (2011) 116803. doi:10.1103/PhysRevLett.107.116803.

[122] O. Lehtinen, J. Kotakoski, A. V. Krasheninnikov, A. Tolvanen, K. Nordlund, J. Keinonen, Effects of ion bombardment on a two dimensional target: Atomistic simulations of graphene irradiation, Phys. Rev. B. 81 (2010) 153401. doi:10.1103/PhysRevB.81.153401.

[123] A.C. Ferrari, D.M. Basko, Raman spectroscopy as a versatile tool for studying the properties of graphene, Nat. Nanotechnol. 8 (2013) 235–246. doi:10.1038/nnano.2013.46.

[124] A. Politano, M. Cattelan, D.W. Boukhvalov, D. Campi, A. Cupolillo, S. Agnoli, N.G. Apostol, P. Lacovig, S. Lizzit, D. Farias, G. Chiarello, G. Granozzi, R. Larciprete, D. Farías, G. Chiarello, G. Granozzi, R. Larciprete, Unveiling the Mechanisms Leading to H2 Production Promoted by Water Decomposition on Epitaxial Graphene at Room Temperature, ACS Nano. 10 (2016) 4543–4549. doi:10.1021/acsnano.6b00554.

[125] A. Ambrosetti, P.L. Silvestrelli, Communication: Enhanced chemical reactivity of graphene on a Ni(111) substrate, J. Chem. Phys. 144 (2016) 111101. doi:10.1063/1.4944090.

[126] F. Banhart, J. Kotakoski, A. V. Krasheninnikov, Structural Defects in Graphene, ACS Nano. 5 (2011) 26–41. doi:10.1021/nn102598m.

[127] B. Borca, S. Barja, M. Garnica, M. Minniti, A. Politano, J.M. Rodriguez García, J.J. Hinarejos, D. Farías, A.L.V. de Parga, R. Miranda, Electronic and geometric corrugation of periodically rippled, self nanostructured graphene epitaxially grown on Ru(0001), New J. Phys. 12 (2010) 93018. doi:10.1088/1367 2630/12/9/093018.

[128] M. Rocca, S. Lehwald, H. Ibach, T.S. Rahman, Phonon dispersion of the (22) phase of carbon on the reconstructed Ni(100) surface, Phys. Rev. B. 35 (1987) 9510–9519. doi:10.1103/PhysRevB.35.9510.

[129] P. Jacobson, B. Stöger, A. Garhofer, G.S. Parkinson, M. Schmid, R. Caudillo, F. Mittendorfer, J. Redinger, U. Diebold, Disorder and Defect Healing in Graphene on Ni(111), J. Phys. Chem. Lett. 3 (2012) 136–139. doi:10.1021/jz2015007.

[130] L. Ferrighi, D. Perilli, D. Selli, C. Di Valentin, Water at the Interface Between Defective Graphene and Cu or Pt (111) Surfaces, ACS Appl. Mater. Interfaces. 9 (2017) 29932–29941. doi:10.1021/acsami.7b06633.

[131] T. Osaki, T. Mori, Role of Potassium in Carbon Free CO2 Reforming of Methane on K Promoted Ni/Al2O3 Catalysts, J. Catal. 204 (2001) 89–97. doi:10.1006/jcat.2001.3382.

[132] H. Nakano, J. Ogawa, J. Nakamura, Growth mode of carbide from C2H4 or CO on Ni(111), Surf. Sci. 514 (2002) 256–260. doi:10.1016/S0039 6028(02)01638 2.

[133] R.A. Bueno, J.I. Martínez, R.F. Luccas, N.R. del Árbol, C. Munuera, I. Palacio, F.J. Palomares, K. Lauwaet, S. Thakur, J.M. Baranowski, W. Strupinski, M.F. López, F. Mompean, M. García Hernández, J.A. Martín Gago, Highly selective covalent organic functionalization of epitaxial graphene, Nat. Commun. 8 (2017) 15306. doi:10.1038/ncomms15306.

[134] M.P. Levendorf, C.J. Kim, L. Brown, P.Y. Huang, R.W. Havener, D.A. Muller, J. Park, Graphene and boron nitride lateral heterostructures for atomically thin circuitry, Nature. 488 (2012) 627–632. doi:10.1038/nature11408.

[135] L. Niu, Z. Li, W. Hong, J. Sun, Z. Wang, L. Ma, J. Wang, S. Yang, Pyrolytic synthesis of boron doped graphene and its application aselectrode material for supercapacitors, Electrochim. Acta. 108 (2013) 666–673. doi:10.1016/j.electacta.2013.07.025.

[136] S. Wang, L. Zhang, Z. Xia, A. Roy, D.W. Chang, J.B. Baek, L. Dai, BCN graphene as efficient metal free electrocatalyst for the oxygen reduction reaction, Angew. Chemie Int. Ed. 51 (2012) 4209–4212. doi:10.1002/anie.201109257.

[137] H. Wang, Y. Zhou, D. Wu, L. Liao, S. Zhao, H. Peng, Z. Liu, Synthesis of boron doped graphene monolayers using the sole solid feedstock by chemical vapor deposition, Small. 9 (2013) 1316–1320. doi:10.1002/smll.201203021.

[138] D. Wei, Y. Liu, Y. Wang, H. Zhang, L. Huang, G. Yu, Synthesis of N Doped Graphene by Chemical Vapor Deposition and Its Electrical Properties, Nano Lett. 9 (2009) 1752–1758. doi:10.1021/nl803279t.

[139] J. Lu, K. Zhang, X.F. Liu, H. Zhang, T.C. Sum, A.H.C. Neto, K.P. Loh, Order disorder transition in a two dimensional boron carbon nitride alloy, Nat. Commun. 4 (2013). doi:10.1038/ncomms3681.

[140] Z. S. Wu, W. Ren, L. Xu, F. Li, H. M. Cheng, Doped Graphene Sheets As Anode Materials with Superhigh Rate and Large Capacity for Lithium Ion Batteries, ACS Nano. 5 (2011) 5463–5471. doi:10.1021/nn2006249.

[141] L. Lai, J.R. Potts, D. Zhan, L. Wang, C.K. Poh, C. Tang, H. Gong, Z. Shen, J. Lin, R.S. Ruoff, Exploration of the active center structure of nitrogen doped graphene based catalysts for oxygen reduction reaction, Energy Environ. Sci. 5 (2012) 7936. doi:10.1039/c2ee21802j.

[142] Z. H. Sheng, L. Shao, J. J. Chen, W. J. Bao, F. B. Wang, X. H. Xia, Catalyst free synthesis of nitrogen doped graphene via thermal annealing graphite oxide with melamine and its excellent electrocatalysis., ACS Nano. 5 (2011) 4350–8. doi:10.1021/nn103584t.

[143] N. Li, Z. Wang, K. Zhao, Z. Shi, Z. Gu, S. Xu, Large scale synthesis of N doped multi layered graphene sheets by simple arc discharge method, Carbon N. Y. 48 (2010) 255–259. doi:10.1016/j.carbon.2009.09.013.

[144] L.S. Panchakarla, K.S. Subrahmanyam, S.K. Saha, A. Govindaraj, H.R. Krishnamurthy, U. V. Waghmare, C.N.R.R. Rao, Synthesis, structure, and properties of boron and nitrogen doped graphene, Adv. Mater. 560012 (2009) NA NA. doi:10.1002/adma.200901285.

[145] I.Y. Jeon, H.J. Choi, M.J. Ju, I.T. Choi, K. Lim, J. Ko, H.K. Kim, J.C. Kim, J.J. Lee, D. Shin, S.M. Jung, J.M. Seo, M.J. Kim, N. Park, L. Dai, J.B. Baek, Direct nitrogen fixation at the edges of graphene nanoplatelets as efficient electrocatalysts for energy conversion, Sci. Rep. 3 (2013). doi:10.1038/srep02260.

[146] P. Wu, Z. Cai, Y. Gao, H. Zhang, C. Cai, Enhancing the electrochemical reduction of hydrogen peroxide based on nitrogen doped graphene for measurement of its releasing process from living cells, Chem. Commun. 47 (2011) 11327. doi:10.1039/c1cc14419g.

[147] L. Sun, L. Wang, C. Tian, T. Tan, Y. Xie, K. Shi, M. Li, H. Fu, Nitrogen doped graphene with high nitrogen level via a one step hydrothermal reaction of graphene oxide with urea for superior capacitive energy storage, RSC Adv. 2 (2012) 4498. doi:10.1039/c2ra01367c.

[148] Y. Zheng, Y. Jiao, L. Ge, M. Jaroniec, S.Z. Qiao, Two Step Boron and Nitrogen Doping in Graphene for Enhanced Synergistic Catalysis, Angew. Chemie. 125 (2013) 3192–3198. doi:10.1002/ange.201209548.

[149] L. Wang, P. Yu, L. Zhao, C. Tian, D. Zhao, W. Zhou, J. Yin, R. Wang, H. Fu, B and N isolate doped graphitic carbon nanosheets from nitrogen containing ion exchanged resins for enhanced oxygen reduction, Sci. Rep. 4 (2014). doi:10.1038/srep05184.

[150] Y. Gong, G. Shi, Z. Zhang, W. Zhou, J. Jung, W. Gao, L. Ma, Y. Yang, S. Yang, G. You, R. Vajtai, Q. Xu, A.H. Macdonald, B.I. Yakobson, J. Lou, Z. Liu, P.M. Ajayan, Direct chemical conversion of graphene to boron and nitrogen and carbon containing atomic layers, Nat. Commun. 5 (2014). doi:10.1038/ncomms4193.

[151] B. Muchharla, A. Pathak, Z. Liu, L. Song, T. Jayasekera, S. Kar, R. Vajtai, L. Balicas, P.M. Ajayan, S. Talapatra, N. Ali, Tunable electronics in large area atomic layers of boron nitrogen carbon, Nano Lett. 13 (2013) 3476–3481. doi:10.1021/nl400721y.

[152] G.H. Han, J.A. Rodríguez Manzo, C.W. Lee, N.J. Kybert, M.B. Lerner, Z.J. Qi, E.N. Dattoli, A.M. Rappe, M. Drndic, A.T.C. Johnson, Continuous growth of hexagonal graphene and boron nitride in plane heterostructures by atmospheric pressure chemical vapor deposition, ACS Nano. 7 (2013) 10129–10138. doi:10.1021/nn404331f.

[153] K. Shehzad, Y. Xu, C. Gao, X. Duan, Three dimensional macro structures of two dimensional nanomaterials, Chem. Soc. Rev. 45 (2016) 5541–5588. doi:10.1039/C6CS00218H.

[154] S. Nappini, I. Píš, T.O. Menteş, A. Sala, M. Cattelan, S. Agnoli, F. Bondino, E. Magnano, Formation of a Quasi Free Standing Single Layer of Graphene and Hexagonal Boron Nitride on Pt(111) by a Single Molecular Precursor, Adv. Funct. Mater. 26 (2016) 1120–1126. doi:10.1002/adfm.201503591.

[155] D.H. Kang, M. Trenary, Surface chemistry of dimethylamine on Pt(1 1 1): Formation of methylaminocarbyne and its decomposition products, Surf. Sci. 519 (2002) 40–56. doi:10.1016/S0039 6028(02)02145 3.

[156] D.H. Kang, B. Chatterjee, E. Herceg, M. Trenary, Adsorption and decomposition of trimethylamine on Pt( 1 1 1 ): Formation of dimethylaminocarbyne (CN(CH3)2), Surf. Sci. 540 (2003) 23–38. doi:10.1016/S0039 6028(03)00833 1.

[157] K. Mudiyanselage, M. Trenary, R.J.R.J. Meyer, Formation of methyl isocyanide from dimethylamine on Pt(111), J. Phys. Chem. C. 112 (2008) 3794–3799. doi:10.1021/jp709581j.

[158] R.J. Simonson, M.T. Paffett, M.E. Jones, B.E. Koel, A vibrational study of borazine adsorbed on Pt(111) and Au(111) surfaces, Surf. Sci. 254 (1991) 29–44. doi:10.1016/0039 6028(91)90635 6.

[159] A.B. Preobrajenski, M.L. Ng, A.S. Vinogradov, N. Mårtensson, Controlling graphene corrugation on lattice mismatched substrates, Phys. Rev. B Condens. Matter Mater. Phys. 78 (2008) 73401. doi:10.1103/PhysRevB.78.073401.

[160] A. Nagashima, N. Tejima, Y. Gamou, T. Kawai, C. Oshima, Electronic states of monolayer hexagonal boron nitride formed on the metal surfaces, Surf. Sci. 357–358 (1996) 307–311. doi:10.1016/0039 6028(96)00134 3.

[161] a. Preobrajenski, a. Vinogradov, M. Ng, E. Ćavar, R. Westerström, a. Mikkelsen, E. Lundgren, N. Mårtensson, Influence of chemical interaction at the lattice mismatched h BN/Rh(111) and h BN/Pt(111) interfaces on the overlayer morphology, Phys. Rev. B. 75 (2007) 1–8. doi:10.1103/PhysRevB.75.245412.

[162] R. Laskowski, P. Blaha, Ab initio study of h BN nanomeshes on Ru(001), Rh(111), and Pt(111), Phys. Rev. B Condens. Matter Mater. Phys. 81 (2010). doi:10.1103/PhysRevB.81.075418.

[163] K. Okazaki Maeda, Y. Morikawa, S. Tanaka, M. Kohyama, Atomic and Electronic Structures of Pt Supported on Graphene, MRS Proc. 900 (n.d.). doi:DOI: 10.1557/PROC 0900 O06 35.

[164] H. Werheit, H. Haupt, On the interpretation of the phonon spectra of boron carbide and β rhombohedral boron, AIP Conf. Proc. 231 (1991) 355–362. doi:10.1063/1.40851.

[165] U. Kuhlmann, H. Werheit, Raman effect of boron carbide (B4.3C to B10.37C), J. Alloys Compd. 205 (1994) 87–91. doi:https://doi.org/10.1016/0925 8388(94)90771 4.

[166] K. Shirai, S. Emura, Lattice Vibrations of Boron Carbide, J. Solid State Chem. 133 (1997) 93–96. doi:10.1006/jssc.1997.7321.

[167] M. Cattelan, G. Peng, E. Cavaliere, L. Artiglia, A. Barinov, L.T. Roling, M. Favaro, I. Píš, S. Nappini, E. Magnano, F. Bondino, L. Gavioli, S. Agnoli, M. Mavrikakis, G. Granozzi, The nature of the Fe graphene interface at the nanometer level, in: AIP Conf. Proc., 2016. doi:10.1063/1.4952924.

[168] M.L. Ng, R. Balog, L. Hornekær, A.B. Preobrajenski, N.A. Vinogradov, N. Mårtensson, K. Schulte, Controlling Hydrogenation of Graphene on Transition Metals.pdf, (2010) 18559–18565.

[169] J. Gebhardt, R.J. Koch, W. Zhao, O. Höfert, K. Gotterbarm, S. Mammadov, C. Papp, A. Görling, H. P. Steinrück, T. Seyller, Growth and electronic structure of boron doped graphene, Phys. Rev. B. 87 (2013) 155437. doi:10.1103/PhysRevB.87.155437.

[170] M. Cattelan, S. Agnoli, M. Favaro, D. Garoli, F. Romanato, M. Meneghetti, A. Barinov, P. Dudin, G. Granozzi, Microscopic view on a chemical vapor deposition route to boron doped graphene nanostructures, Chem. Mater. 25 (2013) 1490–1495. doi:10.1021/cm302819b.

[171] T.M. Chen, J. Xiao, G.W. Yang, Cubic boron nitride with an intrinsic peroxidase like activity, RSC Adv. 6 (2016) 70124–70132. doi:10.1039/C6RA14856E.

[172] M.N. Uddin, I. Shimoyama, Y. Baba, T. Sekiguchi, M. Nagano, X ray photoelectron spectroscopic observation on B–C–N hybrids synthesized by ion beam deposition of borazine, J. Vac. Sci. Technol. A Vacuum, Surfaces, Film. 23 (2005) 497. doi:10.1116/1.1894667.

[173] H. Sediri, D. Pierucci, M. Hajlaoui, H. Henck, G. Patriarche, Y.J. Dappe, S. Yuan, B. Toury, R. Belkhou, M.G. Silly, F. Sirotti, M. Boutchich, A. Ouerghi, Atomically Sharp

Interface in an h BN epitaxial graphene van der Waals Heterostructure, Sci. Rep. 5 (2015). doi:10.1038/srep16465.

[174] M.A. Mannan, H. Noguchi, T. Kida, M. Nagano, N. Hirao, Y. Baba, Chemical bonding states and local structures of the oriented hexagonal BCN films synthesized by microwave plasma CVD, Mater. Sci. Semicond. Process. 11 (2008) 100–105. doi:10.1016/j.mssp.2009.04.003.

[175] M. Abdul Mannan, M. Nagano, T. Kida, N. Hirao, Y. Baba, Characterization of BCN films synthesized by radiofrequency plasma enhanced chemical vapor deposition, J. Phys. Chem. Solids. 70 (2009) 20–25. doi:10.1016/j.jpcs.2008.08.013.

[176] S.Y. Kim, J. Park, H.C. Choi, J.P. Ahn, J.Q. Hou, H.S. Kang, X ray photoelectron spectroscopy and first principles calculation of BCN nanotubes., J. Am. Chem. Soc. 129 (2007) 1705–16. doi:10.1021/ja067592r.

[177] G. Rostamikia, M.J. Janik, First principles mechanistic study of borohydride oxidation over the Pt(1 1 1) surface, Electrochim. Acta. 55 (2010) 1175–1183. doi:10.1016/j.electacta.2009.10.002.

[178] A.M. Baró, H. Ibach, H.D. Bruchmann, Vibrational modes of hydrogen adsorbed on Pt(111): Adsorption site and excitation mechanism, Surf. Sci. 88 (1979) 384–398. doi:https://doi.org/10.1016/0039 6028(79)90082 7.

[179] M. Keppeler, E. Roduner, Platinum–hydrogen vibrations and low energy electronic excitations of 13 atom Pt nanoclusters, Phys. Chem. Chem. Phys. 16 (2014) 26613–26616. doi:10.1039/C4CP02052A.

[180] R. Deng, M. Trenary, Carbon nitrogen bond formation from the reaction of ammonia with dicarbon on the Pt(111) surface, J. Phys. Chem. C. 111 (2007) 17088–17093. doi:10.1021/jp075668f.

[181] A.F. Carley, P.R. Davies, D. Edwards, R. V. Jones, M. Parsons, Molecularly resolved studies of the reaction of pyridine and dimethylamine with oxygen at a Cu(110) surface, Top. Catal. 36 (2005) 21–32. doi:10.1007/s11244 005 7859 1.

[182] F. Bondino, G. Comelli, A. Baraldi, E. Vesselli, R. Rosei, A. Goldoni, S. Lizzit, NO adsorption on Rh(100). II. Stability of the adlayers, J. Chem. Phys. 119 (2003) 12534–12539. doi:10.1063/1.1627757.

[183] C.J. Weststrate, J.W. Bakker, E.D.L. Rienks, C.P. Vinod, A. V. Matveev, V. V. Gorodetskii, B.E. Nieuwenhuys, Ammonia oxidation on Pt(410), J. Catal. 242 (2006) 184–194. doi:10.1016/j.jcat.2006.06.011.

[184] A. Baraldi, S. Lizzit, M.G. Ramsey, F.P. Netzer, Direct observation of C N uptake and dissociation on Pd ( 110 ) by fast high resolution XPS, 416 (1998) 214–225.

[185] F. Bondino, A. Baraldi, G. Comelli, F.P. Netzer, Structure and stability of CN adlayers on Rh(110), Surf. Sci. 461 (2000) 31–44. doi:10.1016/s0039 6028(00)00520 3.

[186] J.C. Koepke, J.D. Wood, Y. Chen, S.W. Schmucker, X. Liu, N.N. Chang, L. Nienhaus, J.W. Do, E.A. Carrion, J. Hewaparakrama, A. Rangarajan, I. Datye, R. Mehta, R.T. Haasch, M.

Gruebele, G.S. Girolami, E. Pop, J.W. Lyding, Role of pressure in the growth of hexagonal boron nitride thin films from ammonia borane, Chem. Mater. 28 (2016) 4169–4179. doi:10.1021/acs.chemmater.6b00396.

[187] G. Rupprechter, T. Dellwig, H. Unterhalt, H.J. Freund, CO adsorption on Ni(100) and Pt(111) studied by infrared visible sum frequency generation spectroscopy: design and application of an SFG compatible UHV high pressure reaction cell, Top. Catal. 15 (2001) 19–26. doi:10.1023/A:1009063611629.

[188] A. Politano, A.R. Marino, G. Chiarello, Phonon dispersion of quasi freestanding graphene on Pt(111), J. Phys. Condens. Matter. 24 (2012) 104025. doi:10.1088/0953 8984/24/10/104025.

[189] E. Rokuta, Y. Hasegawa, K. Suzuki, Y. Gamou, C. Oshima, A. Nagashima, Phonon Dispersion of an Epitaxial Monolayer Film of Hexagonal Boron Nitride on Ni(111), Phys. Rev. Lett. 79 (1997) 4609–4612. doi:10.1103/PhysRevLett.79.4609.

[190] Y. Murata, T. Mashoff, M. Takamura, S. Tanabe, H. Hibino, F. Beltram, S. Heun, Correlation between morphology and transport properties of quasi free standing monolayer graphene, Appl. Phys. Lett. 105 (2014). doi:10.1063/1.4902988.

[191] V. Tozzini, V. Pellegrini, Prospects for hydrogen storage in graphene, Phys. Chem. Chem. Phys. 15 (2013) 80–89. doi:10.1039/C2CP42538F.

[192] S. Goler, C. Coletti, V. Tozzini, V. Piazza, T. Mashoff, F. Beltram, V. Pellegrini, S. Heun, Influence of Graphene Curvature on Hydrogen Adsorption: Toward Hydrogen Storage Devices, J. Phys. Chem. C. 117 (2013) 11506–11513. doi:10.1021/jp4017536.

[193] T. Balgar, H. Kim, E. Hasselbrink, Preparation of graphene with graphane areas of controlled hydrogen isotope composition on opposite sides, J. Phys. Chem. Lett. 4 (2013) 2094–2098. doi:10.1021/jz400690w.

[194] L. Kyhl, R. Balog, T. Angot, L. Hornekær, R. Bisson, Hydrogenated graphene on Ir(111): A high resolution electron energy loss spectroscopy study of the vibrational spectrum, Phys. Rev. B. 93 (2016) 115403. doi:10.1103/PhysRevB.93.115403.

[195] F. Speck, J. Jobst, F. Fromm, M. Ostler, D. Waldmann, M. Hundhausen, H.B. Weber, T. Seyller, The quasi free standing nature of graphene on H saturated SiC(0001), Appl. Phys. Lett. 99 (2011) 2014–2017. doi:10.1063/1.3643034.

[196] T. Seyller, Passivation of hexagonal SiC surfaces by hydrogen termination, J. Phys. Condens. Matter. 16 (2004) S1755–S1782. doi:10.1088/0953 8984/16/17/016.

[197] J.D. Emery, V.H. Wheeler, J.E. Johns, M.E. McBriarty, B. Detlefs, M.C. Hersam, D. Kurt Gaskill, M.J. Bedzyk, Structural consequences of hydrogen intercalation of epitaxial graphene on SiC(0001), Appl. Phys. Lett. 105 (2014). doi:10.1063/1.4899142.

[198] F.C. Bocquet, R. Bisson, J.M. Themlin, J.M. Layet, T. Angot, Reversible hydrogenation of deuterium intercalated quasi free standing graphene on SiC(0001), Phys. Rev. B Condens. Matter Mater. Phys. 85 (2012) 1–4. doi:10.1103/PhysRevB.85.201401.

[199] F.C. Bocquet, R. Bisson, J. M. Themlin, J. M. Layet, T. Angot, Deuterium adsorption on (and desorption from) SiC(0001) (33), (√3√3)R30, (6√36√3)R30 and quasi free standing graphene obtained by hydrogen intercalation, J. Phys. D. Appl. Phys. 47 (2014) 94014. doi:10.1088/0022 3727/47/9/094014.

[200] N.P. Guisinger, G.M. Rutter, J.N. Crain, P.N. First, J. a Stroscio, Exposure of Epitaxial Graphene on SiC ( 0001 ) to Atomic Hydrogen, Nano Lett. 9 (2009) 1462–1466. doi:10.1021/nl803331q.

[201] R.J. Koch, T. Haensel, S.I. U.U. Ahmed, T. Seyller, J.A. Schaefer, HREELS study of graphene formed on hexagonal silicon carbide, Phys. Status Solidi. 7 (2010) 394–397. doi:10.1002/pssc.200982481.

[202] S. Watcharinyanon, C. Virojanadara, J.R. Osiecki, A.A. Zakharov, R. Yakimova, R.I.G. Uhrberg, L.I. Johansson, Hydrogen intercalation of graphene grown on 6H SiC(0001), Surf. Sci. 605 (2011) 1662–1668. doi:10.1016/j.susc.2010.12.018.

[203] J.S. Bunch, S.S. Verbridge, J.S. Alden, A.M. Van Der Zande, J.M. Parpia, H.G. Craighead, P.L. McEuen, Impermeable atomic membranes from graphene sheets, Nano Lett. 8 (2008) 2458–2462. doi:10.1021/nl801457b.

[204] L.S. Ramsdell, Studies on Silicon Carbide, Am. Mineral. 32 (1947) 64–82.

[205] S. Fiori, Y. Murata, S. Veronesi, A. Rossi, C. Coletti, S. Heun, Li intercalated graphene on SiC(0001): An STM study, Phys. Rev. B. 96 (2017) 1–8. doi:10.1103/PhysRevB.96.125429.

[206] Y. Li, G. Zhou, J. Li, J. Wu, B.L. Gu, W. Duan, Lithium intercalation induced decoupling of epitaxial graphene on SiC(0001): Electronic property and dynamic process, J. Phys. Chem. C. 115 (2011) 23992–23997. doi:10.1021/jp208747q.

[207] R.J. Koch, T. Seyller, J.A. Schaefer, Strong phonon plasmon coupled modes in the graphene/silicon carbide heterosystem, Phys. Rev. B Condens. Matter Mater. Phys. 82 (2010) 2–5. doi:10.1103/PhysRevB.82.201413.

[208] R.J. Koch, S. Fryska, M. Ostler, M. Endlich, F. Speck, T. Hänsel, J.A. Schaefer, T. Seyller, Robust Phonon Plasmon Coupling in Quasifreestanding Graphene on Silicon Carbide, Phys. Rev. Lett. 116 (2016) 106802. doi:10.1103/PhysRevLett.116.106802.

[209] H. Kim, T. Balgar, E. Hasselbrink, Is there sp 3 bound H on epitaxial graphene? Evidence for adsorption on both sides of the sheet, Chem. Phys. Lett. 546 (2012) 12–17. doi:10.1016/j.cplett.2012.07.049.

[210] E. Aréou, G. Cartry, J. M.M. Layet, T. Angot, Hydrogen graphite interaction: Experimental evidences of an adsorption barrier, J. Chem. Phys. 134 (2011) 8–13. doi:10.1063/1.3518981.

[211] H. Kim, T. Balgar, E. Hasselbrink, The stretching vibration of hydrogen adsorbed on epitaxial graphene studied by sum frequency generation spectroscopy, Chem. Phys. Lett. 508 (2011) 1–5. doi:10.1016/j.cplett.2011.04.025.

[212] R.P. Chin, J.Y. Huang, Y.R. Shen, T.J. Chuang, H. Seki, Interaction of atomic hydrogen with the diamond C(111) surface studied by infrared visible sum frequency generation spectroscopy, Phys. Rev. B. 52 (1995) 5985–5995. doi:10.1103/PhysRevB.52.5985.

[213] T. Ohta, J.T. Robinson, P.J. Feibelman, A. Bostwick, E. Rotenberg, T.E. Beechem, Evidence for Interlayer Coupling and Moiré Periodic Potentials in Twisted Bilayer Graphene, Phys. Rev. Lett. 109 (2012) 186807. doi:10.1103/PhysRevLett.109.186807.

[214] C. Riedl, A.A. Zakharov, U. Starke, Precise in situ thickness analysis of epitaxial graphene layers on SiC(0001) using low energy electron diffraction and angle resolved ultraviolet photoelectron spectroscopy, Appl. Phys. Lett. 93 (2008) 10–13. doi:10.1063/1.2960341.

[215] R. Balog, B. Jørgensen, J. Wells, E. Lægsgaard, P. Hofmann, F. Besenbacher, L. Hornekær, Atomic Hydrogen Adsorbate Structures on Graphene, J. Am. Chem. Soc. 131 (2009) 8744–8745. doi:10.1021/ja902714h.

[216] M. Park, Y.J. Yun, M. Lee, D.H. Jeong, Y. Jun, Y.W. Park, B.H. Kim, Local doping of graphene devices by selective hydrogen adsorption, AIP Adv. 5 (2015) 17120. doi:10.1063/1.4906254.

[217] S.Y. Shin, N.D. Kim, J.G. Kim, K.S. Kim, D.Y. Noh, K.S. Kim, J.W. Chung, Control of the π plasmon in a single layer graphene by charge doping, Appl. Phys. Lett. 99 (2011) 82110. doi:10.1063/1.3630230.

[218] G. Sclauzero, A. Pasquarello, First principles study of H adsorption on graphene/SiC(0001), Phys. Status Solidi Basic Res. 250 (2013) 2523–2528. doi:10.1002/pssb.201300084.

[219] L. Hornekær, Ž. Šljivančanin, W. Xu, R. Otero, E. Rauls, I. Stensgaard, E. Lægsgaard, B. Hammer, F. Besenbacher, Metastable structures and recombination pathways for atomic hydrogen on the graphite (0001) surface, Phys. Rev. Lett. 96 (2006) 1–4. doi:10.1103/PhysRevLett.96.156104.

[220] L. Nilsson, M. Andersen, R. Balog, E. Lægsgaard, P. Hofmann, F. Besenbacher, B. Hammer, I. Stensgaard, L. Hornekær, Graphene Coatings: Probing the Limits of the One Atom Thick Protection Layer, ACS Nano. 6 (2012) 10258–10266. doi:10.1021/nn3040588.

[221] C. Virojanadara, A.A. Zakharov, R. Yakimova, L.I. Johansson, Buffer layer free large area bi layer graphene on SiC(0 0 0 1), Surf. Sci. 604 (2010) L4–L7. doi:10.1016/j.susc.2009.11.011.

[222] A. Paris, N. Verbitskiy, A. Nefedov, Y. Wang, A. Fedorov, D. Haberer, M. Oehzelt, L. Petaccia, D. Usachov, D. Vyalikh, H. Sachdev, C. Wöll, M. Knupfer, B. Büchner, L. Calliari, L. Yashina, S. Irle, A. Grüneis, Kinetic Isotope Effect in the Hydrogenation and Deuteration of Graphene, Adv. Funct. Mater. 23 (2013) 1628–1635. doi:10.1002/adfm.201202355.

[223] T.P.M. Goumans, J. Kästner, Hydrogen Atom Tunneling Could Contribute to H2 Formation in Space, Angew. Chemie Int. Ed. 49 (2010) 7350–7352. doi:10.1002/anie.201001311.

[224] Y. Xia, Z. Li, H.J. Kreuzer, Adsorption, diffusion and desorption of hydrogen on graphene, Surf. Sci. 605 (2011) L70–L73. doi:10.1016/j.susc.2011.07.009.

[225] A. Markevich, R. Jones, S. Öberg, M.J. Rayson, J.P. Goss, P.R. Briddon, First principles study of hydrogen and fluorine intercalation into graphene SiC(0001) interface, Phys. Rev. B Condens. Matter Mater. Phys. 86 (2012) 1–9. doi:10.1103/PhysRevB.86.045453.